A Synvolcanic Origin for Magnetite-rich Orebodies Hosted by BIF in the Weld Range District, Western Australia

PAUL DUURING[1,2*], STEFFEN G. HAGEMANN[2], DAVID A. BANKS[3], CHRISTIAN SCHINDLER[2]

[1]Geological Survey of Western Australia, Department of Mines and Petroleum, 100 Plain Street, East Perth, Western Australia 6004, Australia

[2]Centre for Exploration Targeting, The University of Western Australia, Crawley, Western Australia 6009, Australia

[3]School of Earth and Environment, University of Leeds, Leeds, United Kingdom

[*]Corresponding author: email, pduuring@hotmail.com

Abstract

Iron ore deposits hosted by Archean banded iron-formation (BIF) in the Weld Range greenstone belt are representative of most of the documented iron ore deposits in the Yilgarn Craton. They include near-surface, supergene goethite-hematite orebodies that overlie and partly modify deeper occurrences of hypogene magnetite and specular hematite ores. The Cenozoic goethite-hematite-rich orebodies in these deposits are unequivocally the product of meteoric fluid alteration affecting BIF in the near-surface supergene environment; however, the deeper and likely older magnetite- and specular hematite-rich orebodies have a more contentious origin. This study is the first to present a fluid-alteration model for hypogene iron mineralization in the Yilgarn Craton that uses fluid inclusion and mineral chemistry data to constrain the physical-chemical characteristics and source of hypogene fluids responsible for mineralization. High-grade (>57 wt% Fe), magnetite-rich iron ore at the Beebyn deposit defines a discontinuous series of <80 m-thick by <1 km-long lenses that extend 3 km along strike in the BIF. These magnetite-rich lenses are surrounded by a broad carbonate alteration halo in the BIF and intense ferroan chlorite and talc alteration in nearby basalt, dolerite, and gabbro country rocks. Magnetite-rich lenses at Beebyn are the product of the replacement of primary quartz bands in the BIF by Stages 1 and 2 hypogene carbonate minerals, followed by their replacement by magnetite and minor ferroan dolomite. Fluid inclusion studies demonstrate that Stage 1 fluids were high-temperature (>440 °C) and CO_2-rich. Paired O and C stable isotope data for Stage 1 ferroan dolomite suggest that these fluids had a magmatic source, while Stage 1 magnetite chemistry (e.g. enrichments in Mg, Mn, Ca, and Na) indicates chemical exchange took place between the fluids and mafic igneous rocks prior to crystallization of magnetite. The presence of monophase carbonic fluid inclusions in Stage 1 ferroan dolomite suggest that phase separation of a bicarbonate-rich aqueous fluid took place in deeper parts of the hydrothermal system, which led to the separation of the resultant volatile-rich and brine phases during transport of the Stage 1 fluid to shallower crustal levels. Cooling of the hydrothermal system during the Stage 2 fluid event involved (i) an early brine (>275 to 327 ºC; 36 to 40 equiv. wt% NaCl) with Cl/Br and C and O isotopes values that overlap the ranges

for magmatic fluids, with minor involvement of Archean seawater, and extensive chemical exchange with country rocks; followed by (ii) pulses of moderate- and lower-temperature Stage 2 brines (>125 to 260 ºC; 2 to 24 equiv. wt% $CaCl_2$) with Cl/Br, O and C isotope, Na/Br, and Ca/Ca+Na signatures that suggest cooling of magmatic-derived fluids that mixed with Archean seawater and reacted with mafic igneous country rocks in areas more distal to fluid pathways. The last stage of formation of magnetite-rich ore at the Beebyn deposit involved the flow of Stage 3 fluids through the existing fault network that controlled earlier fluids. Stage 3 fluids are lower-temperature (>98 to 175 °C), low to high-salinity brines with Cl/Br values that overlap reported ranges for 3.2 Ga vent fluids and seawater. Thus, they are likely the product of heated Archean seawater that was chemically-modified through interaction with mafic country rocks. Magnetite-talc veins at the Madoonga deposit have fluid halogen ratios for fluid inclusions hosted by magnetite that are compatible with a range of possible sources, including low-grade metamorphic fluids, geothermal brines, or oil field formation waters. Although, their common spatial association with semi-massive sulfides suggests their likely precipitation from brines derived from heated Archean seawater. More locally developed specular hematite-quartz veins that cut folded magnetite-rich ores at the Beebyn and Madoonga deposits are the product of iron redistribution in BIF by heated meteoric fluids or seawater, with precipitation of specular hematite as a consequence of oxidation and cooling of the fluid.

Keywords: *Weld Range, banded iron-formation, magnetite, hematite, iron ore*

Introduction

All major iron ore districts in the Hamersley Province, Pilbara Craton and Yilgarn Craton of Western Australia contain high-grade (>57 wt% Fe) iron orebodies hosted by Archean to Paleoproterozoic banded iron-formation (BIF). In all cases, these high-grade orebodies are the product of secondary enrichment of iron in BIF through interaction with hydrothermal fluids (Hagemann et al., 2016 and references therein). The Cenozoic goethite-hematite-rich orebodies in these deposits are unequivocally the product of meteoric fluid alteration affecting BIF in the near-surface supergene environment (e.g. Morris, 1980). However, the deeper and likely older magnetite-, specular hematite-, and microplaty hematite-rich orebodies have a more contentious origin, and several rival genetic models have been proposed, including (i) early diagenetic de-silicification of BIF with corresponding iron enrichment (Lascelles, 2006), (ii) a supergene-metamorphic origin where very low-grade metamorphic dehydration at 80 to 100 °C led to the conversion of Paleoproterozoic supergene goethite to microplaty hematite ore (Morris, 1985; Morris and Kneeshaw, 2011), and (iii) a supergene-modified hypogene fluid model that invokes the involvement of hot externally-derived fluids for the upgrading of iron in BIF; principally via the replacement of primary quartz bands in BIF by hypogene carbonate minerals, followed by carbonate dissolution and concentration of residual iron oxide minerals to produce large volumes of high-grade iron ore (Barley et al., 1999; Powell et al., 1999; Taylor et al., 2001; Angerer et al., 2015; Hagemann et al., 2016; this study).

The BIF-hosted iron ore deposits of the Yilgarn Craton include near-surface, supergene goethite-hematite orebodies that overlie and partly modify deeper occurrences of hypogene magnetite and specular

hematite ores (e.g. Koolyanobbing and Windarling deposits, Angerer and Hagemann, 2010; Angerer et al., 2013; Weld Range, Duuring and Hagemann, 2013b; Jack Hills, Maskell et al., 2014). Although structural and hydrothermal models exist for many of these deposits, there are no existing studies that use fluid inclusion evidence to directly constrain the physical and chemical characteristics of hypogene fluids responsible for BIF-hosted iron mineralization in the Yilgarn Craton. This study is the first to address this knowledge gap by examining fluid inclusions from the Beebyn and Madoonga deposits, located in the Weld Range greenstone belt in the Murchison Domain of the Yilgarn Craton (Fig. 1).

This study applies a multidisciplinary approach to characterizing hypogene fluids at both deposits. Fluid inclusion studies that include microthermometry, laser Raman analyses, laser Ablation Inductive Coupled Mass Spectrometry (LA-ICP-MS), and crush leachate analysis are employed to constrain hypogene fluid compositions and trapping conditions. Stable oxygen and carbon isotope values for hypogene alteration minerals are used to estimate crystallization temperatures and likely fluid sources. LA-ICP-MS analysis of iron oxide minerals is used to constrain mineral chemistry and interpret changes in fluid compositions and sources for the fluid alteration events (details about all methods are reported in Online Appendix 1). These data are then integrated in the construction of a fluid-alteration model for hypogene iron mineralization at Weld Range. An improved understanding of genetic processes for BIF-hosted iron ore in the Yilgarn Craton has direct relevance for refining the Mineral Systems model for BIF-hosted iron deposits and consequently for exploring for these types of deposits world-wide (Hagemann et al., 2016).

Geology of the Weld Range Greenstone Belt and BIF-hosted Iron Deposits

Weld Range greenstone belt

Archean supracrustal rocks exposed in the Weld Range greenstone belt include, from north to south, 2977 ± 3 Ma felsic crystal tuff (Wingate et al., 2013), several BIF horizons, tuffaceous siltstones, and felsic volcanic and volcaniclastic rocks (Fig. 1). The ENE-trending, subvertical, stratigraphic sequence is intruded by c. 2805 Ma mafic-ultramafic rocks of the Gnanagooragoo igneous complex (Wingate et al., 2012). Farther south, the Gnanagooragoo igneous complex is overlain by c. 2710 to 2705 Ma, undifferentiated felsic volcanic and volcaniclastic rocks, and by schistose pelite and psammite units of the Ryansville Formation. Gabbronorite, gabbro, and dolerite of the Yalgowra Suite locally intrude the schistose pelite and psammite units (Ivanic, 2009). Post-tectonic monzogranite of the Bald Rock Supersuite (c. 2637 to 2592 Ma) truncate the northern margins of the Wilgie Mia Formation and Gnanagooragoo igneous complex (Van Kranendonk and Ivanic, 2009). Supracrustal rocks in the Weld Range greenstone belt are metamorphosed to lower-greenschist facies (300 ± 50° C) at pressures of <2-3 kbar (Gole, 1980). District-scale structures in the belt include ENE-trending, isoclinal F_1 folds that have an axial planar foliation oriented subparallel to bedding in supracrustal rocks (Spaggiari, 2006; Duuring and Hagemann, 2013b). The folding of bedding contacts and a bedding-parallel foliation (axial planar to F_1 folds) in rocks of the Ryansville Formation

(Ivanic, 2009) define a moderately SW-plunging F_2 syncline located to the south of the main series of ENE-trending ridges (Fig. 1).

Outcrop in the Weld Range district mostly corresponds with a series of ENE-trending ridges, 3 to 5 km-wide, 70 km-long, and <150 m-high. Individual ridges are 10 to 500 m wide, and mostly correspond with exposures of BIF that are more resistant to erosion compared to surrounding mafic igneous, or rhyolitic volcanic and volcaniclastic rocks. All rocks exposed at surface are at least moderately weathered, whereas rocks that are more fractured are usually intensively weathered. The base of weathering varies across the Weld Range district and is commonly 150 to 200 m below surface, but is as deep as 300 m in faulted parts of the Madoonga BIF deposit.

Beebyn deposit geology

Key relationships between rock types, structures, and hydrothermal alteration mineral assemblages in BIF and surrounding mafic igneous rocks at the Beebyn deposit are described in detail by Duuring et al. (2012; 2013b) and Duuring and Laukamp (2016); thus, only a summary of these features is included here. Three main BIF units (informally named the Beebyn North, Central, and South BIF) crop out in the main ENE-trending ridge at the Beebyn deposit (Fig. 2A). The exposed BIF units are up to 80 m thick, trend ENE, and dip steeply (>80º) to the SSE (Fig. 2C). Basalt, dolerite, and gabbro country rocks envelop the Beebyn North, Central, and South BIF. All primary lithological contacts between BIF and mafic igneous rocks are deformed, with only thin (<3 m-thick) dolerite sills within the three main BIF units recording primary intrusive contacts. Rare, <1 m-thick, intervals of shale or siltstone are present within the North and Central BIF. The BIFs represent a lithotectonic unit (terminology after Neuendorf et al., 2005) in that their alternating silica- and iron oxide-rich bands are a composite of primary compositional layers and several superimposed, F_1 and F_2 fold-related, axial planar fabrics that are now oriented subparallel to compositional bands in the BIF (Duuring and Hagemann, 2013b). Facing indicators are not observed. The BIFs and intervening mafic igneous rocks are locally offset up to 200 m by NNW- to NNE-trending, subvertical faults (Fig. 2A). High-grade magnetite±martite ("martite" terminology after Clark, 1993) and goethite±hematite ore zones are thickest in the North BIF, coincident with the W11 and W10 prospects (Fig. 2A). The adjacent prospects located to the west (i.e. W9, W8, W7) and east (W12) host narrower lenses of high-grade Fe ore. Surrounding mafic igneous rocks do not host high-grade Fe ore. The North BIF hosts high-grade Fe ore from the present surface to vertical depths of at least 250 m (Fig. 2C). Goethite-hematite ore zones in BIF extend from surface to about 60 m depth, magnetite-martite-rich zones occur from 60 to 150 m, whereas magnetite-rich zones dominate in unweathered rocks below 150 m.

Below the weathering front, BIF and nearby mafic igneous country rocks record multiple stages of structurally-controlled, hypogene alteration prior to the onset of near-surface weathering (Fig. 3). These sequential hypogene alteration stages affect the mineralogy, texture, and chemistry (including Fe content) of the least-altered BIF (Fig. 4A) and mafic rocks. The result is a <80 m-thick, Fe ore body that displays zoned hypogene alteration mineral and geochemical patterns in BIF and mafic country rocks. The earliest hypogene alteration event (Stage 1) affecting BIF involved the direct replacement of quartz in silica-rich bands by fine-grained, anhedral Stage 1 hypogene siderite and ferroan dolomite, with hypogene magnetite

nucleating on existing magnetite-rich primary bands and also forming disseminated, euhedral crystals surrounded by Stage 1 carbonates (Fig. 4B). The Stage 2 event entailed the local development of Stage 2 ferroan dolomite veins that cut primary iron oxide-rich bands and earlier Stage 1 altered BIF (Fig. 4C and D) and the replacement of quartz-rich bands by ferroan dolomite (Fig. 4E and F). Proximal areas to magnetite-rich ore zones (e.g. the W10 prospect) display a higher proportion of ferroan dolomite veins and hydrothermal breccias. Stage 2 accessory minerals identified with a Scanning Electron Microscope (SEM) include apatite, monazite, xenotime, pyrite, chalcopyrite, galena, and sphalerite, as well as several undefined sulfide minerals (i.e. Cu-S, As-Ni-Co-Fe-Sb-S, Pb-Cu-Ag-Sb-Zn-S) and a W-Sr-Fe-bearing oxide mineral. Carbonate mineral replacement of quartz-rich bands preserve the original texture of BIF, but drastically change the bulk chemistry of the BIF through a major depletion (98 %) in the abundance of SiO_2, with increases in CaO, MgO, Loss on Ignition (LOI) values, C, P_2O_5, and $Fe_2O_{3(total)}$ (Duuring and Hagemann, 2013b). Stages 1 and 2 carbonate-alteration of BIF is most intensely developed along the deformed northern margin of the Beebyn North BIF and extends about 4 km along strike between the W11 and W7 prospects (Fig. 2A).

The Stage 3 hypogene alteration event involved reactivation of existing structures and replacement of Stage 1 and 2 carbonate minerals by finer-grained Stage 3 magnetite-ferroan dolomite±apatite±monazite (Fig. 4D, E, F), primarily in the W11 and W10 prospects, and more sporadically distributed in the W9, W8, and W7 prospects. In some areas replacement of the Stages 1 and 2 carbonate gangue minerals was associated with a volume decrease in the rock and resulted in the residual concentration of primary magnetite-rich bands (Fig. 4E). The resultant high-grade, magnetite-rich ore zones in BIF are thinly banded and are locally crenulated, cavity-rich, and brecciated. The ore zones are depleted in SiO_2 (by up to 99 %) and enriched in $Fe_2O_{3(total)}$, K_2O, CaO, MgO and P_2O_5 compared with least-altered BIF (Duuring and Hagemann, 2013b). The folding of carbonate-altered BIF and the residual magnetite-rich ore zones by F_2 folds indicate that the timing of Stages 1, 2, and 3 alteration predates district-wide upright folding and tilting of the greenstone sequence in the Weld Range district.

Stage 4 chlorite-hematite±talc±apatite±monazite hypogene alteration zones (Fig. 5A) are present in all prospects in the Beebyn deposit, where they are associated with 2 m-wide, bedding-parallel shear zones that locally replace least-altered and Stages 1, 2, and 3 altered BIF (Fig. 5B). Specular hematite lenses are located along the deformed limbs or are present in the hinge areas of parasitic F_2 folds that deform the residual magnetite-rich ore zones. Three more subsequent stages of hypogene alteration (i.e. Stages 5, 6 and 7; Duuring and Hagemann, 2013b) have a restricted expression at the scale of the Beebyn deposit and are unlikely to have a major influence on the bulk chemistry of the ore body. Stage 5 quartz-magnetite±chalcopyrite locally replaces Stage 2 ferroan dolomite and Stage 3 dolomite (Fig. 5C) in the W10 prospect. Stage 6 ferroan dolomite- and calcite-rich veins (Fig. 5D) are common throughout the Beebyn deposit. The veins are 1-30 mm thick and cut Stages 2, 3, and 4 hydrothermal alteration mineral assemblages. Stage 7 siderite-chlorite-magnetite veins cut Stage 6 veins (Fig. 5E) in the W10 prospect (additional photographs of altered BIF and matching thin sections are included in the Online Appendix 2).

Fresh mafic igneous rocks also show a distinct hypogene alteration zonation pattern. Proximal and intermediate alteration zones located up to 20 m from the contact with BIF-hosted, magnetite-rich ore zones display the replacement of primary and metamorphic Ca- and Na-rich minerals, such as amphibole,

plagioclase, and epidote, by hypogene ferroan chlorite, ferroan dolomite, and siderite. Geochemical anomalies in proximal alteration zones include enrichments in LOI, MgO, and $Fe_2O_{3(total)}$ values, and depletions in SiO_2, CaO, K_2O, and Na_2O (Duuring and Hagemann, 2013b).

Within 60 m of the present surface, weathered examples of hypogene-altered BIF display a massive to mottled secondary texture, resulting from the destruction of mesobands and the replacement of primary, metamorphic, and hypogene minerals by fine-grained goethite (Fig. 5F). Supergene-altered mafic igneous rocks show the replacement of primary, metamorphic, and hydrothermal minerals by goethite, hematite, and kaolinite.

Madoonga deposit geology

A detailed description of the Madoonga deposit geology, including relationships between rock types, structure, and hydrothermal alteration mineral assemblages, is provided by Duuring et al. (2013a). The Madoonga deposit is hosted by the northern-most BIF in the Weld Range district and is principally centred on the W14 prospect, with smaller pods of high-grade iron ore located along strike in the W15 and W25 prospects (Fig. 2B). From north to south, the lithotectonic unit at the Madoonga deposit includes a quartz-feldspar-phyric volcanic and volcaniclastic rock intruded by dolerite and gabbro, a <60 m-thick northern BIF (hereafter referred to as the “Madoonga North BIF”), a <40 m-thick volcaniclastic or (volcanogenic)-sedimentary rock, a southern <150 m-thick BIF (i.e. Madoonga South BIF), a 100 m-thick pyritic mudstone containing metre-thick intervals of semi-massive pyrite intergrown with cryptocrystalline quartz, and dolerite and gabbro. The lithotectonic unit is unconformably overlain by a flat-lying, <80 m-thick, poorly-sorted detrital unit comprising angular fragments of BIF clasts cemented by supergene goethite (Fig. 2D).

The deposit includes four genetically distinct styles of iron ore: hypogene magnetite-talc veins, hypogene specular hematite-quartz veins, supergene goethite-hematite enriched BIF, and supergene goethite-hematite-altered detrital sediments (Fig. 2D). The residual magnetite-rich ore type documented at the Beebyn deposit is notably absent at Madoonga. Ore formation involved superimposed multiple hypogene and supergene alteration stages (Fig. 6Fig.). Semi-massive pyrite intervals (Fig. 7A and B), pyrite veins, and spherical pyrite nodules in mudstone along the southern margin of the Madoonga South BIF are most likely syn-sedimentary in origin, representing exhalative or subseafloor replacement style alteration in mudstone. Guilliamse (2014) reports the additional presence of Cu-Zn-Pb-bearing massive sulfides and stringer veins along the northern margin of the North BIF in the W27 and W15 prospects (Fig. 2B). These sulfides are associated with intense chlorite and more distal sericite alteration zones in nearby felsic volcanic rocks. The local presence of sulfide lenses and veins at both margins of BIF at the Madoonga deposit suggests multiple hydrothermal fluid events that predate regional folding of BIF, or alternatively a single fluid event with replacement-style sulfidation localized at several positions in the sequence.

Stage 1 jaspilite (terminology after Hagemann et al., 2008) containing alternating jasper and hematite ± magnetite bands is preserved in the Madoonga North and South BIF units below the weathering front in the W14, W15, and W25 prospects. Stage 2 magnetite-talc±apatite±monazite±xenotime veins (Fig. 7C) hosted by faults or shear zones cut Stage 1 jaspilite at shallow angles to bands in the BIF. The ore zones are <3 m thick, <50 m long, and are located along major lithological contacts. Ore zones are thickest

in areas of structural complexity, such as dilational jogs, fault splays, and bends in the W14 and W15 prospects. Magnetite-rich shear zones are folded by tight, upright, moderately WSW-plunging regional F_2 folds. Magnetite-talc veins and proximal alteration zones in BIF are enriched in $Fe_2O_{3(total)}$, P_2O_5, MgO, Sc, Ga, Al_2O_3, Cl, and Zr; and depleted in SiO_2 and MnO_2, relative to least-altered BIF (Duuring and Hagemann, 2013a).

Stage 3 specular hematite-quartz±apatite±monazite veins (Fig. 7D) are <2 m thick and hosted by en echelon, ENE-trending faults that locally cut F_2 folds in BIF in the W15 and W19 prospects (Fig. 1 and Fig. 2B). These Stage 3 veins have a similar relative timing relationship to the Stage 4 chlorite-hematite±talc hypogene alteration zones documented in the Beebyn deposit. At the Madoonga deposit, the veins are surrounded by <40 m-thick, hypogene alteration zones that comprise an inner halo of microplaty hematite and an outer halo of hematite alteration. The alteration zones are best developed in areas surrounding fault jogs, splays, or bends. Specular hematite-quartz-rich ore zones are enriched in $Fe_2O_{3(total)}$, but are contaminated by SiO_2 (Duuring and Hagemann, 2013a).

Stage 4 siderite-quartz veins, Stage 5 ferroan chlorite-pyrite veins, and Stage 6 quartz-ferroan dolomite veins locally cut the North and South BIF at Madoonga (representative photographs of rocks and matching thin sections are included in the Online Appendix 3). The veins are up to 2 m-thick and are oriented subparallel to bands in BIF, with alteration halos that replace earlier hypogene alteration mineral assemblages. These veins are distributed throughout the Madoonga deposit but have a minor influence on the chemistry and physical properties of the main ore body.

Mafic igneous country rocks located within 10 m of the northern contact to the Madoonga North BIF display the replacement of primary igneous amphibole and plagioclase, and metamorphic chlorite, by ferroan chlorite, talc, and minor magnetite. Altered mafic igneous country rocks are enriched in $Fe_2O_{3(total)}$, P_2O_5, Al_2O_3, and TiO_2; and depleted in K_2O, Na_2O, CaO, and SiO_2, relative to least-altered mafic country rocks (Duuring and Hagemann, 2013a).

Supergene goethite-hematite ore is <150 m wide, <400 m long, and extends to vertical depths of about 300 m below the present surface. The ore zones are controlled by the intersection between late NNW- to NNE-trending, subvertical brittle faults and the ENE-trending BIF. Within these highly deformed areas, least-altered BIF and existing hypogene Fe ores are replaced by intense supergene goethite-hematite alteration, which destroys existing bands in the BIF and results in a cavity-rich Fe ore that is enriched in $Fe_2O_{3(total)}$ and depleted in SiO_2.

Supergene goethite-hematite-cemented detrital sediments are thickest along the southern margin of the ENE-trending ridge at Madoonga (Fig. 2D). The detrital deposits extend for about 3 km in strike, are <200 m wide, and <100 m deep. The detrital unit is mostly low-grade (<55 wt% Fe), but varies widely in Fe grade along strike and with depth due to its heterogeneous content. The unit formed as a result of the erosion and transport of least-altered BIF, mafic igneous rocks, and high-grade Fe ore zones exposed along the ridge. These fragments were transported short distances due to gravity and fluvial processes, and were deposited in paleo-topographic depressions located adjacent to the ridge. Once accumulated, the poorly-sorted fragments were partly cemented by goethite during the circulation of supergene fluids through the unconsolidated sediment.

Fluid Inclusion Data for Multi-stage Hypogene Alteration of BIF

Sample selection for fluid inclusion studies

Representative hand-specimens of fresh, hypogene-altered BIF from the Beebyn and Madoonga deposits were selected for microthermometry, crush-leach, and in situ LA-ICP-MS analysis. The aim of these analyses was to characterize the physical and chemical properties of the hypogene fluids responsible for high-grade magnetite- and specular hematite-rich ore zones in each deposit, as well as characterize the major post-ore fluid alteration events affecting BIF.

From the Beebyn deposit, hand specimens of hypogene alteration Stages 1 to 3 are crucial for understanding the genesis of high-grade magnetite-rich ore at this deposit. They record the step-wise replacement of primary quartz bands by hypogene carbonate minerals (Stages 1 and 2), followed by their partial replacement by hypogene magnetite (Stage 3). Beebyn Stage 4 alteration resulted in specular hematite-rich ore zones; however, fluid inclusions were not observed in Stage 4 chlorite, hematite, or talc using conventional or infrared transmitted-light microscopy. Beebyn Stages 5 to 7 are post-ore stages identified by quartz replacement domains, or carbonate-rich veins that cut existing magnetite- and specular hematite-rich ore zones in BIF. Twenty-two 100 µm-thick, doubly-polished thin sections were prepared from hand specimens of Beebyn alteration Stages 1, 2, 3, 5, 6, and 7, and were used for microthermometry.

From the Madoonga deposit, only Madoonga Stage 3 specular hematite-quartz veins associated with high-grade specular hematite ore zones were suitable for microthermometry. Fluid inclusions were not observed in Madoonga Stage 2 magnetite-talc veins, whereas Madoonga post-ore Stages 4 to 6 samples contain submicron-sized fluid inclusions in their quartz and carbonate mineral hosts. Nine 100 µm-thick, doubly-polished thin sections were prepared from Madoonga Stage 3 specular hematite-quartz veins and used for microthermometry.

Fluid inclusion assemblages

Primary, pseudosecondary, and secondary fluid inclusion assemblages (terminology after Roedder, 1984; Goldstein and Reynolds, 1994) exist in all quartz and carbonate mineral hosts obtained from the Beebyn and Madoonga deposits. Primary fluid inclusion assemblages are mostly located in the centre of crystalline quartz and carbonate minerals, or near the nucleation surfaces of these crystals (e.g. Fig. 8E). The morphology of these fluid inclusion-rich domains commonly mirrors the crystal form of the host mineral (Fig. 8E and Fig. 9C). In some areas, the fluid inclusion-rich domains are surrounded by fluid inclusion-poor rims that locally include narrower bands of fluid inclusions, thus indicating incremental growth zones in these crystals. Pseudosecondary fluid inclusion assemblages that define three-dimensional trails within crystals that terminate before crystal boundaries (e.g. Fig. 8B) most likely represent healed fractures. In contrast, trails of secondary fluid inclusion assemblages cut crystal boundaries and their timing post-dates crystallization of the host mineral. Temperature ranges for each hydrothermal alteration stage are provided below; Table A1 shows summary microthermometry data for fluid inclusion assemblages, whereas Table

A2 provides data for all measured fluid inclusions. It should be noted that due to the lack of evidence for fluid boiling, the temperatures of total homogenization reported for each alteration stage represent minimum trapping temperatures since a pressure correction (cf. Potter, 1977) is not possible without the availability of independent geobarometric constraints. In this case, pressure corrections to minimum trapping temperature estimates are not possible due to large uncertainties associated with interpreting depths of fluid trapping during crystallization during the various stages of vein formation in the Weld Range greenstone belt. The common presence of unconformities at major unit boundaries, plus the effects of multiple folding events, prevents an accurate determination of crustal thickness during the stages of hydrothermal alteration in BIF.

Microthermometry results

Beebyn Stage 1 (pre-ore fluid alteration event) Beebyn Stage 1 magnetite-siderite±ferroan dolomite replaces primary quartz-rich bands in BIF. Stage 1 siderite and ferroan dolomite crystals are <300 µm-wide, irregularly-shaped, and intergrown with disseminated, <1 mm-wide, subhedral to euhedral magnetite (Fig. 4B). Stage 1 ferroan dolomite crystals host abundant carbonic fluid inclusions that range in size from submicron to 12 µm. At room temperature (25 ºC), both monophase vapor and two-phase, liquid-rich CO_2 inclusions were observed (Fig. 8A and B). From four doubly-polished thin sections of Stage 1 magnetite-siderite±ferroan dolomite altered BIF, only sample BN-W9-104 contained fluid inclusions that were sufficiently large for microthermometry. Within this sample, five ferroan dolomite crystals, each surrounded by Stage 1 magnetite, host primary or pseudosecondary trails of carbonic fluid inclusion assemblages (Fig. 8B). The measured fluid inclusions range in size from 3 to 12 µm in length and 2 to 6 µm in width. Freezing experiments demonstrate that the five fluid inclusion assemblages have internally consistent final melt temperatures (T_{mCO2}) indicated by the melting of solid CO_2 that range from -56.7 to -57.5 ºC (Table A1). These fluid inclusion assemblages display final homogenization temperatures ($T_{h(CO2l)}$) to the liquid phase (L) that range from 18.6 to 28.3 ºC. The measured T_{mCO2} indicate that Stage 1 fluid inclusions are dominantly CO_2-rich, with possible minor presence of other gases. However, laser Raman spectroscopy performed on 12 representative fluid inclusions from the five siderite crystals in sample BN-W9-104 demonstrates strong diagnostic peaks for the presence of CO_2 with no other peaks detected apart from those for the ferroan dolomite host (Fig. 10). Calculated densities range from 0.65 to 0.79 g/cm^3.

Beebyn Stage 2 (pre-ore fluid alteration event) Beebyn Stage 2 ferroan dolomite veins cut Stage 1 magnetite-siderite±ferroan dolomite-altered bands (Fig. 8C and D), or replaces primary quartz-rich bands (Fig. 8E and F). Stage 2 ferroan dolomite locally forms <5 mm-wide, subhedral to euhedral crystals that grow inwards from the margins of vein walls or iron oxide-rich bands. Ferroan dolomite crystals display undulose to uniform extinction in cross-polarized transmitted light. Euhedral crystals of Stage 2 ferroan dolomite commonly host dense clusters of 1 to 25 µm-long, primary fluid inclusions surrounded by fluid inclusion-poor rims, indicating primary mineral growth zones in these crystals (Fig. 8E). Eight doubly-polished thin sections were prepared from Stage 2 ferroan dolomite±magnetite-altered BIF from the W10 and W8 prospects, which are located about 4 km apart and represent proximal and distal zones to

magnetite-rich ore, respectively (Fig. 2A). From these thin sections, 33 primary fluid inclusion assemblages were measured for microthermometry (Table A1). Most fluid inclusion assemblages comprise two-phase (liquid-vapor) aqueous-rich fluid inclusions (Fig. 8F), with only one documented sample (BN-W10-013) hosting eight fluid inclusion assemblages that contain three-phase (liquid-vapor-solid) aqueous-rich fluid inclusions (Fig. 8C and D). All documented fluid inclusions are equant to irregularly-shaped and range in size from 2 to 25 µm in length and 1 to 15 µm in width. No relative timing relationships were observed between ferroan dolomite crystals that host two-phase or three-phase fluid inclusion assemblages; they are interpreted to represent discrete crystallization stages within a long-lived, widespread, Stage 2 hypogene fluid alteration event.

The two-phase aqueous-rich fluid inclusions hosted by Beebyn Stage 2 ferroan dolomite crystals contain 80 to 90 vol% liquid and 10 to 20 vol% vapor (Fig. 8F). Rare accidentally trapped translucent solids are present in some fluid inclusions and were unchanged during heating to about 500 ºC. Two-phase aqueous-rich fluid inclusion assemblages have initial melting temperatures (T_i) that define a maximum range from -45.0 to -62.0 ºC, with individual fluid inclusion assemblages displaying more restricted T_i that vary by <5 ºC (Fig. 11A). The T_i ranges for individual fluid inclusion assemblages are comparable between (i) different ferroan dolomite crystals from the same sample, (ii) hand-specimens collected from the same prospect, and (iii) samples from the W8 and W10 prospects (Fig. 11A). The observed T_i for the fluid inclusion assemblages are below the eutectic temperature for the H_2O-NaCl system (i.e. -21.2 ºC) and therefore suggest the presence of additional cations such as Ca, Mg, and Fe (the presence of these cations were independently confirmed by LA-ICP-MS analysis of these inclusions, described below). Melting temperatures of ice ($T_{m\,(ice)}$) are more variable than the T_i ranges, defining a maximum $T_{m\,(ice)}$ range from -1.1 to -28.4 ºC, although individual fluid inclusion assemblages have $T_{m\,(ice)}$ determinations that vary by <5 ºC. Ferroan dolomite crystals within the same hand-specimen have very similar $T_{m\,(ice)}$ ranges, with the greatest variations in $T_{m\,(ice)}$ ranges occurring between different hand-specimens. The W8 and W10 prospects display similar maximum ranges in $T_{m\,(ice)}$. Two-phase aqueous-rich fluid inclusion assemblages homogenize by the disappearance of vapor bubbles over a wide range of temperatures, from 125 to 257 ºC, although $T_{h(total)}$ values for individual fluid inclusion assemblages vary by <11 ºC) (Table A1) (Fig. 11B). The Oakes et al. (1990) equation of state for the H_2O-NaCl-$CaCl_2$ system was used to calculate salinities for the two-phase fluid inclusions due to observed T_i values being lower than the T_e for a H_2O-NaCl fluid (-21.2 ºC). Calculated salinities for the Beebyn Stage 2 two-phase fluid inclusions range from 2.7 to 23.4 equiv. wt% $CaCl_2$ (Fig. 11C), with densities ranging from 0.83 to 1.08 g/cm^3 (Fig. 11D).

Less common three-phase aqueous-rich fluid inclusions, hosted by Beebyn Stage 2 ferroan dolomite contain 75 to 90 vol% liquid, 5 to 15 vol% vapor, and 5 to 10 vol% solid (Fig. 8D). The solids are cubic and dissolve during heating, suggesting that they are halite daughter crystals. The T_i range of -50.0 to -59.7 ºC for three-phase aqueous-rich fluid inclusions is similar to the range for two-phase aqueous-rich fluid inclusions (Fig. 11A). Heating shows that three-phase aqueous-rich fluid inclusion assemblages display the disappearance of the vapor bubble at temperatures from 100 to 173 ºC and are completely homogenized by the dissolution of halite within the range of 275 to 327 ºC (Table A1) (Fig. 11B). Thus, $T_{h(total)}$ values are consistently higher for three-phase aqueous-rich fluid inclusions compared with two-phase fluid inclusions. The Lecumberri-Sanchez et al. (2012) equation of state for the H_2O-NaCl-(KCl)

system was used to calculate salinities for the Beebyn Stage 2 three-phase fluid inclusions, based on the dissolution temperatures of halite daughter crystals. Calculated salinities range from 36.5 to 39.5 equiv. wt% NaCl (Fig. 11C), with densities ranging from 1.07 to 1.27 g/cm^3 (Fig. 11D).

Beebyn Stage 3 (syn-ore fluid alteration event) Beebyn Stage 3 magnetite (60 vol%) and ferroan dolomite (40 vol%) replace Stages 1 and 2 carbonate minerals in BIF (Fig. 4F and Fig. 8G) to produce high-grade magnetite-rich ore. Stage 3 magnetite and ferroan dolomite are fine-grained (<350 μm), subhedral to euhedral, and display an interlocking texture. Stage 3 ferroan dolomite crystals display uniform extinction in cross-polarized transmitted light and host <40 μm-wide, mineral inclusions of Stage 3 magnetite. The contained fluid inclusions are 2 to 20 μm long, 1 to 10 μm wide, and irregularly shaped (Fig. 8H). These fluid inclusions and magnetite mineral inclusions are interpreted to be primary on the basis that they are mostly concentrated in the centre of Stage 3 ferroan dolomite and are surrounded by narrower, inclusion-poor rims. Seven doubly-polished thin sections were prepared of Stage 3 magnetite-dolomite-altered BIF from the W8 and W10 prospects. From these thin sections, two samples from the W10 prospect contain 10 primary fluid inclusion assemblages that were used for microthermometry (Table A1). Most fluid inclusion assemblages comprise two-phase (liquid-vapor) aqueous-rich fluid inclusions, with opaque accidentally-trapped solids (magnetite) present in about 10 % of measured inclusions. Primary fluid inclusions contain 80 to 90 vol% liquid and 10 to 20 vol% vapor. Two-phase aqueous-rich fluid inclusion assemblages have T_i that define a range from -53.1 to -62.7 ºC, with individual fluid inclusion assemblages displaying more precise T_i that vary by <4 ºC (Fig. 11A). Melting temperatures of ice define a large $T_{m\ (ice)}$ range from -2.6 to -14.0 ºC, with individual fluid inclusion assemblages displaying $T_{m\ (ice)}$ that vary by <2 ºC. Two-phase aqueous-rich fluid inclusion assemblages display total homogenization by the disappearance of their vapor bubbles at temperatures from 98 to 174 ºC ($T_{h(total)}$ values for individual fluid inclusion assemblages vary by <25 ºC) (Table A1) (Fig. 11B). Using the Oakes et al. (1990) equation of state for the H_2O-NaCl-$CaCl_2$ system, calculated salinities for the Beebyn Stage 3 two-phase fluid inclusions range from 4.4 to 17.3 equiv. wt% $CaCl_2$ (Fig. 11C), with densities ranging from 1.05 to 1.10 g/cm^3 (Fig. 11D).

Beebyn Stage 5 (post-ore fluid alteration event) Beebyn Stage 5 quartz-magnetite±chalcopyrite replaces Stages 2 and 3 carbonate minerals in BIF. Stage 5 quartz crystals are coarse-grained (<2 mm-wide), anhedral to euhedral (Fig. 5C and Fig. 9A), and display uniform extinction in transmitted cross-polarized light. Primary fluid inclusions are concentrated in the center of quartz crystals (Fig. 9A and B), whereas pseudosecondary fluid inclusions define trails that terminate before quartz crystal boundaries. Primary and pseudosecondary fluid inclusions are 3 to 30 μm long, 3 to 25 μm wide, and are equant to irregularly shaped. Irregular-shaped magnetite mineral inclusions are spatially associated with primary and pseudosecondary fluid inclusions (Fig. 9B). Two doubly-polished thin sections were prepared of Stage 5 quartz-magnetite±chalcopyrite-altered BIF from the W10 prospect. From these thin sections, eight primary or pseudosecondary fluid inclusion assemblages were used for microthermometry (Table A1). All observed fluid inclusion assemblages contain three-phase (liquid-vapor-solid) aqueous-rich fluid inclusions (Fig. 9B). The fluid inclusions contain 80 to 90 vol% liquid, 5 to 10 vol% vapor, and 5 to 10 vol% solid. The solids are

cubic and dissolve during heating, suggesting that they are halite daughter crystals. Initial melting temperatures define a range of -52.0 to -65.0 ºC, with individual fluid inclusion assemblages varying by <2 ºC (Fig. 11A). Three-phase aqueous-rich fluid inclusion assemblages have a homogenization temperature ($T_{h\ (l)}$) range from 117 to 159 ºC (to the liquid phase) and total homogenization temperatures ($T_{h(total)}$) by halite dissolution that have a range from 133 to 196 ºC (Table A1) (Fig. 11B). Individual fluid inclusion assemblages show more precise homogenization ranges of <17 ºC. Using the Lecumberri-Sanchez et al. (2012) equation of state for the H_2O-NaCl-(KCl) system, calculated salinities for the Beebyn Stage 5 halite-bearing, three-phase aqueous-rich fluid inclusions range from 28.5 to 31.7 equiv. wt% NaCl (Fig. 11C). Densities range from 1.13 to 1.23 g/cm^3 (Fig. 11D).

Beebyn Stage 6 (post-ore fluid alteration event) Beebyn Stage 6 ferroan dolomite- and calcite-rich veins cut Beebyn Stages 2, 4, and 5 hydrothermal alteration mineral assemblages. Stage 6 ferroan dolomite-rich veins comprise varying proportions of calcite, magnetite, pyrite, and chalcopyrite. Ferroan dolomite crystals are coarse, euhedral, and intergrown with anhedral magnetite (Fig. 5D). Stage 6 ferroan dolomite crystals display uniform extinction in transmitted cross-polarized light. The center of ferroan dolomite crystals host abundant primary fluid inclusions (5 to 30 µm-long, 3 to 15 µm-wide) and cogenetic, <30 µm-wide, mineral inclusions of magnetite; the distribution of fluid inclusions commonly mirror the crystal form of the host ferroan dolomite crystal (Fig. 9C and D). Four doubly-polished thin sections from the W10 prospect were examined and one thin section was selected for microthermometry. From this one sample, four primary fluid inclusion assemblages were measured. The primary fluid inclusion assemblages include two-phase (liquid-vapor) aqueous-rich fluid inclusions, with accidentally-trapped translucent (undetermined) solids present in about 20 % of measured inclusions (Fig. 9D). Primary fluid inclusions contain 80 to 90 vol% liquid and 10 to 20 vol% vapor. The T_i for fluid inclusion assemblages range from -50.8 to -63.2 ºC, with individual ranges that vary by <4 ºC (Fig. 11A). The $T_{m\ (ice)}$ define a range from -7.0 to -16.3 ºC, with individual fluid inclusion assemblages displaying $T_{m\ (ice)}$ that vary by <2 ºC. Two-phase aqueous-rich fluid inclusion assemblages homogenize by the disappearance of the vapor bubble from 115 to 152 ºC; $T_{h(total)}$ values for individual fluid inclusion assemblages vary by <9 ºC (Table A1) (Fig. 11B). Using the Oakes et al. (1990) equation of state for the H_2O-NaCl-$CaCl_2$ system, calculated salinities for the Beebyn Stage 6 two-phase fluid inclusions range from 10.5 to 19.4 equiv. wt% $CaCl_2$ (Fig. 11C), with densities ranging from 1.02 to 1.10 g/cm^3 (Fig. 11D).

Beebyn Stage 7 (post-ore fluid alteration event) Beebyn Stage 7 siderite-chlorite-magnetite veins cut Stage 6 veins in the W10 prospect. Stage 7 siderite-chlorite-magnetite veins comprise coarse-grained (<1 mm-wide) euhedral siderite intergrown with fibrous ferroan chlorite and bladed magnetite (Fig. 5E). Stage 7 siderite crystals display uniform extinction in transmitted cross-polarized light and host clusters of primary two-phase aqueous fluid inclusions and <30 µm-wide, magnetite mineral inclusions in the center of the crystals (Fig. 9E). Two doubly-polished thin sections from the W10 prospect were prepared and one thin section used for microthermometry. From this sample, three measured primary fluid inclusion assemblages include two-phase (90 vol% liquid and 10 vol% vapor) aqueous-rich fluid inclusions that are 5 to 30 µm long and 3 to 20 µm wide. The T_i for the fluid inclusion assemblages range from -57.0 to -68.0 ºC, with

individual ranges that vary by <4 ºC (Fig. 11A). The $T_{m\ (ice)}$ define a range from -8.0 to -13.3 ºC, with individual fluid inclusion assemblages displaying $T_{m\ (ice)}$ that vary by <2 ºC. Two-phase aqueous-rich fluid inclusion assemblages homogenize by the disappearance of vapor bubbles from 125 to 180 ºC; $T_{h(total)}$ values for individual fluid inclusion assemblages vary by <16 ºC (Table A1) (Fig. 11B). Using the Oakes et al. (1990) equation of state for the H_2O-NaCl-$CaCl_2$ system, calculated salinities for the Beebyn Stage 7 two-phase fluid inclusions range from 11.7 to 17.0 equiv. wt% $CaCl_2$ (Fig. 11C), with densities ranging from 1.00 to 1.08 g/cm^3 (Fig. 11D).

Madoonga Stage 3 (syn-ore fluid alteration event) Specular hematite±quartz veins (Fig. 7D) are present in the Madoonga and Beebyn deposits. The veins are hosted by ENE-trending fault zones that cut magnetite-talc orebodies and upright F_2 folds in BIF. Based on these timing relationships for both deposits, Madoonga Stage 3 specular hematite-quartz veins most likely share a comparable relative timing to Beebyn Stage 4 chlorite-hematite±talc alteration mineral assemblages.

Four doubly-polished thin sections of representative specular hematite-quartz veins were prepared from the Madoonga W19 and W15 prospects. One sample from each prospect was used for microthermometry. Specular hematite was examined using near-infrared transmitted-light microscopy (and later by LA-ICP-MS analysis of specular hematite); however, no fluid inclusions were detected in specular hematite. Instead, cogenetic quartz crystals were examined, with four fluid inclusion assemblages measured from the W19 prospect sample, and nine fluid inclusion assemblages analyzed from the W15 prospect sample.

The sample from the W19 prospect contains euhedral quartz crystals that hosts clusters of primary fluid inclusion assemblages and trails of pseudosecondary fluid inclusion assemblages (Fig. 9G and H). All observed fluid inclusion assemblages comprise 3 to 20 µm-long, 2 to 15 µm-wide, three-phase aqueous-rich fluid inclusions (80 to 90 vol% liquid, 5 to 15 vol% vapor, 5 to 10 vol% solid). The solids are translucent, cubic, and homogenize during heating, suggesting they are halite daughter crystals. Initial melting temperatures define a wide range of -35.0 to -60.0 ºC, although individual fluid inclusion assemblages vary by <12 ºC (Fig. 11A). Three-phase aqueous-rich fluid inclusion assemblages have a homogenization temperature ($T_{h\ (L)}$) range from 87 to 127 ºC (to the liquid phase) and total homogenization temperatures ($T_{h(total)}$) by halite dissolution that have a range from 132 to 146 ºC (Table A1) (Fig. 11B). Individual fluid inclusion assemblages show more precise homogenization ranges of <10 ºC. Using the Lecumberri-Sanchez et al. (2012) equation of state for the H_2O-NaCl-(KCl) system, calculated salinities for the Madoonga Stage 3 halite-bearing, three-phase aqueous-rich fluid inclusions range from 29.3 to 30.1 equiv. wt% NaCl (Fig. 11C). Densities range from 1.16 to 1.19 g/cm^3 (Fig. 11D). Representative fluid inclusions from this sample were analyzed by laser Raman spectroscopy, with no gases detected other than water vapor.

The specular hematite-quartz vein sample from the W15 prospect contains euhedral quartz crystals that are intergrown with, or are completely enclosed by, cogenetic specular hematite. Two-phase (liquid-vapor) aqueous-rich fluid inclusions define pseudosecondary fluid inclusion assemblage trails within quartz crystals. The fluid inclusions are 3 to 20 µm-long, 1 to 10 µm-wide, and are irregular- to negative crystal-shaped. Two distinct populations of fluid inclusion assemblages are identified from their T_i and $T_{m\ (ice)}$. A

lower-salinity population of pseudosecondary fluid inclusion assemblages includes two-phase (85 to 95 vol% liquid and 5 to 15 vol% vapor) aqueous-rich fluid inclusions with T_i that range from -15.1 to -23.6 ºC and $T_{m\ (ice)}$ that range from 0.0 to -9.0 ºC (Table A1) (Fig. 11A). Total homogenization temperatures have a range from 110 to 190 ºC (to L), with individual fluid inclusion assemblages displaying more precise ranges that vary by <10 ºC (Fig. 11B). Using the Bodnar and Vityk (1994) equation of state for the H_2O-NaCl-(KCl) system, calculated salinities for the lower-salinity population of fluid inclusion assemblages range from 0.0 to 12.8 equiv. wt% NaCl (Fig. 11C), whereas densities range from 0.89 to 1.01 g/cm^3 (Fig. 11D). In contrast, a higher-salinity population of pseudosecondary fluid inclusion assemblages is defined by two-phase (90 to 95 vol% liquid and 5 to 10 vol% vapor) aqueous-rich fluid inclusions with T_i that range from -22.9 to -40.0 ºC (Fig. 11A) and $T_{m\ (ice)}$ that range from -10.0 to -21.2 ºC (Table A1). Total homogenization temperatures have a range from 108 to 222 ºC (to L), with individual fluid inclusion assemblages displaying more precise ranges that vary by <26 ºC (Fig. 11B). Using the Oakes et al. (1990) equation of state for the H_2O-NaCl-$CaCl_2$ system, calculated salinities for the higher-salinity two-phase fluid inclusions range from 13.9 to 22.4 equiv. wt% $CaCl_2$ (Fig. 11C), with densities ranging from 0.99 to 1.12 g/cm^3 (Fig. 11D).

Ion chromatography data from crush-leach analyses

Halogen contents and ratios of fluid inclusions are used to differentiate hydrothermal fluids and constrain fluid source areas (Kesler et al., 1995). Twenty-eight mineral separates, derived from selected hypogene alteration stages from the Beebyn and Madoonga deposits, were prepared for ion chromatography (Na, K, Cl, Br, SO_4). Samples included altered BIF from the Beebyn deposit (Stage 2 ferroan dolomite, Stage 3 ferroan dolomite-magnetite, and post-ore Stage 5 quartz), as well as two generations of high-grade hypogene iron ore from the Madoonga deposit (Stage 2 magnetite and Stage 3 specular hematite-quartz veins). Ion chromatography data are reported in Table A3 and graphically in Fig. 12.

The results of the crush-leach analysis show that Cl is the dominant anion relative to Br and SO_4, although values for SO_4 can be higher and more variable for analyzed fluids from Madoonga Stage 3 specular hematite-quartz veins (Table A3). Fluoride was not detected in any sample (<10 ppb in the leached solutions). All fluids contain Na and K, with Na being the more dominant cation (Table A3). Calculated molar Cl/Br ratios for Beebyn Stages 2 and 3 fluids are comparable, but are higher for Beebyn Stage 5 fluids, and highest for Madoonga Stages 2 and 3 fluids (Fig. 12A). Molar Na/Br ratios are lowest for Beebyn Stage 2 fluids and highest for Madoonga Stages 2 and 3 fluids (Fig. 12B). Molar Na/Cl and Na/K ratios are similar in all analyzed hydrothermal fluids, with Beebyn Stage 3 fluids showing the greatest variability (Fig. 12C and D). Molar Na/SO_4 ratios are notably higher for Beebyn samples compared with Madoonga samples (Fig. 12E).

In situ LA-ICP-MS data for fluid inclusions

Primary and pseudosecondary fluid inclusions examined in the microthermometry study were analyzed by in situ LA-ICP-MS to determine their cation abundances (Na, Mg, Si, K, Ca, Mn, Fe, Co, Cu, Zn, Sr, Sn, Ba, W, Pb, and Bi). Samples from the Beebyn deposit include Stage 2 ferroan dolomite and Stage 3 ferroan

dolomite-magnetite, as well as post-ore Stage 5 quartz and Stage 6 ferroan dolomite±magnetite. Madoonga Stage 3 specular hematite-quartz veins were analyzed from the W15 and W19 prospects. Summary LA-ICP-MS data for 26 fluid inclusion assemblages are presented in Table A4, whereas data for all 127 individual fluid inclusion analyses are reported in Table A5.

LA-ICP-MS data are presented as cation ratios normalized against Na for the reason that Na is a constituent of all measured fluid inclusions and is absent in the ferroan dolomite and quartz hosts (Fig. 13). A matrix correction was applied to data obtained from ferroan dolomite to compensate for the joint presence of Mg, Ca, Mn, Fe, Sr, and minor Co and Zn, in fluid inclusions and carbonate mineral hosts (carbonate mineral chemistry was confirmed by LA-ICP-MS spot analyses of fluid inclusion-free ferroan dolomite). Matrix-corrected values for Mg, Ca, Mn, Fe, Sr, Co, and Zn were only included in the final data compilation and derivative plots if laser ablation data peaks measured for these elements correspond precisely with those for Na (Fig. 13A).

All analyzed fluids are rich in Fe, Ca, Mg, Mn, Na, and K (Fig. 14), with lower abundances of Cu, Sr, Ba, Zn, Pb, and Co (i.e. ratios of 0.1 to 0.001 normalized against Na=1), and very minor W, Bi, and Sn (i.e. 0.001 to 0.0001 the concentration of Na). Beebyn Stages 2 and 3 ferroan dolomite-hosted fluid inclusions display indistinguishable cation/Na ratios (Fig. 14 and Fig. 15), whereas Beebyn Stage 5 quartz-hosted fluid inclusions have lower concentrations of Fe, Mn, and Sn. Beebyn Stage 6 ferroan dolomite-hosted fluid inclusions are most similar in cation composition to Stages 2 and 3 fluids, but display the highest Fe, Ca, and Cu concentrations of all measured fluid inclusions. Compared with the Beebyn fluids, Madoonga Stage 3 specular hematite-quartz vein-hosted fluid inclusions display overlapping, but mainly lower values for Ca, Mn, and Sr. Lower-salinity, NaCl-dominant fluid inclusions from the W15 prospect have lower Ca, Mn, Pb, Zn, and Cu concentrations than higher-salinity, multi-cation-dominant fluid inclusions analyzed from the W19 prospect (Fig. 15).

Stable Isotope Data for Quartz, Carbonate Minerals and Magnetite

In situ oxygen isotope data for diagenetic/metamorphic and hypogene quartz

In situ oxygen isotope data were obtained using a CAMECA IMS 1280 multi-collector ion probe for medium-grained quartz in least-altered BIF from the Beebyn and Madoonga deposits. These quartz grains are interpreted to have recrystallized during diagenesis and possibly by later lower-greenschist facies (<300 ºC) regional metamorphism. In addition, oxygen isotope data were collected for quartz from a Beebyn Stage 5 quartz alteration zone in BIF, a Madoonga Stage 3 specular hematite-quartz vein from the W19 prospect, and from a pyrite-quartz vein within semi-massive pyrite intervals located in mudstone near the southern margin of the Madoonga South BIF.

Mineral $\delta^{18}O_{V\text{-}SMOW}$ values for diagenetic/metamorphic quartz grains located across several centimetre-wide bands in the least-altered Beebyn BIF range from 9.22 to 14.38 ‰ (n=14), whereas values

for diagenetic/metamorphic quartz from the Madoonga BIF ranges from 7.26 to 9.06 ‰ (n=14). In comparison, $\delta^{18}O_{V\text{-}SMOW}$ values for Beebyn Stage 5 quartz range from 14.69 to 18.67 ‰ (n=14), Madoonga Stage 3 quartz values range from 11.77 to 12.16 ‰ (n=20), whereas values from semi-massive pyrite-quartz intervals range from 11.80 to 13.26 ‰ (n=10) (Table A6).

Fluid $\delta^{18}O_{H2O}$ values for quartz are calculated using the quartz-H_2O fractionation equations of Sharp and Kirschner (1994) and their respective minimum trapping temperatures derived from microthermometry. In the case of the diagenetic/metamorphic quartz from the least-altered BIF from the Beebyn and Madoonga deposits, it is assumed that the quartz originally precipitated as syn-depositional, silica-rich bands in BIF, but their present mineral and calculated fluid isotopic signatures mostly reflect their re-equilibration with ~300 ºC metamorphic fluids. No microthermometry data exist for quartz analyzed from semi-massive pyrite-quartz veins; however, a temperature estimate of 330 ºC is used based on maximum fluid temperatures reported for vent fluids from major exhalative sulfide deposits (compiled by James et al., 2014). Metamorphic fluids recorded by least-altered BIF define a calculated $\delta^{18}O_{H2O}$ value range of 1.02 to 6.18 ‰ at the Beebyn deposit and -0.94 to 0.86 ‰ at the Madoonga deposit. Hydrothermal, exhalative-style, fluids that precipitated semi-massive pyrite-quartz intervals in mudstone at the Madoonga deposit have calculated $\delta^{18}O_{H2O}$ values from 4.70 to 6.15 ‰. The Beebyn Stage 5 fluid has calculated $\delta^{18}O_{H2O}$ values from -2.51 to 1.47 ‰, whereas Madoonga Stage 3 fluid has calculated $\delta^{18}O_{H2O}$ values from -6.73 to -6.34 ‰ (Table A6).

Carbon and oxygen isotope data for hypogene carbonate mineral separates

Carbon and oxygen isotope data for hypogene carbonate alteration mineral separates are shown in Table A7. The $\delta^{13}C_{V\text{-}PDB}$ values for carbonate minerals from Beebyn Stages 1, 2, and 6 range from -8.87 to -5.72 ‰; whereas their corresponding $\delta^{18}O_{V\text{-}SMOW}$ values range from 8.99 to 14.55 ‰. In comparison, $\delta^{13}C_{V\text{-}PDB}$ values for carbonate minerals from Madoonga Stages 4 and 6 range from -9.63 to -3.52 ‰; corresponding $\delta^{18}O_{V\text{-}SMOW}$ values are from 5.64 to 13.77 ‰ (Table A7).

Methane was not observed in trapped primary fluid inclusions in any of the samples and its presence is assumed to be negligible, with CO_2 being the dominant carbon species in the hydrothermal fluids. $\delta^{13}C_{CO2}$ values for the carbonate minerals are calculated using minimum trapping temperatures determined from microthermometry, although in the case of Beebyn Stage 1 monophase CO_2-rich fluids, a trapping temperature is used from isotopic equilibrium fractionation values determined for cogenetic magnetite and dolomite (i.e. 450 °C; see below). For samples that do not have available microthermometry data, an average temperature estimate was used based on data from nearby samples of the same alteration stage. The $\delta^{13}C_{CO2}$ values for carbonate minerals are calculated using the dolomite-CO_2 and calcite-CO_2 fractionation equations of Ohmoto and Rye (1979), and the siderite-CO_2 equation of Golyshev et al. (1981). $\delta^{18}O_{H2O}$ values for hypogene carbonate minerals are calculated using the dolomite-H_2O and calcite-H_2O fractionation equations of Horita (2014) and Zheng (1999), and the siderite-H_2O equation of Zheng (1999) (Table A7) (Fig. 16). Fluid $\delta^{13}C_{CO2}$ values for carbonate minerals from Beebyn Stages 1, 2, and 6 range from -10.97 to -4.29 ‰; whereas $\delta^{18}O_{H2O}$ values for the same minerals range from -2.84 to 9.57 ‰. In comparison, $\delta^{13}C_{CO2}$ values for carbonate minerals from Madoonga Stages 4 and 6 range from -12.33 to -

6.22 ‰; whereas corresponding $\delta^{18}O_{H2O}$ values range from -8.76 to -0.63 ‰ (Table A7).

Oxygen isotope data for hypogene magnetite separates

In the general case of monophase fluid inclusions observed at room temperature conditions, it is not possible to accurately estimate final trapping temperatures from heating experiments (Yardley and Bodnar, 2014). Instead, additional independent temperature or pressure constraints are required. For this reason, stable oxygen isotope values were determined for Beebyn Stage 1 magnetite (Table A8) and paired oxygen isotope values for cogenetic dolomite separates are used to calculate crystallization temperatures for Stage 1 hydrothermal fluids at the Beebyn deposit. Magnetite $\delta^{18}O_{V\text{-}SMOW}$ values range from 0.72 to 2.01 ‰. Isotope fractionation factors for magnetite (Cole et al., 2004) and dolomite (Zheng, 1999) are used to calculate fluid crystallization temperatures for the Beebyn Stage 1 fluids ranging from 444 to 664 ºC (Table A8). Three of the four sample pairs used for the temperature calculations give estimates of 444 to 465 ºC, whereas the fourth pair provides a substantially higher value of 664 ºC. In this latter case, it is likely that the $\delta^{18}O_{V\text{-}SMOW}$ value for dolomite was shifted to a lower value due to the interaction with later fluids, thereby resulting in an anomalously high temperature estimate. Accordingly, a temperature estimate of 444 to 465 ºC is considered reasonable for the Beebyn Stage 1 fluid.

In situ LA-ICP-MS Trace Element Data for Magnetite and Hematite

Sample selection for LA-ICP-MS analysis of iron oxide minerals

Thirteen polished mounts and thin sections containing iron oxides were selected from the Beebyn and Madoonga deposits with the aim of determining their trace element abundances and interpreting changes in the composition of their formational fluids. Least-altered BIF containing diagenetic/metamorphic magnetite from the Beebyn deposit (Fig. 17A) is compared with hypogene magnetite from Beebyn ore-formation Stages 1 (Fig. 17B) and 3 (Fig. 17C), Stage 4 martite and specular hematite-chlorite veins (Fig. 17D and E, respectively), and post-ore Stages 6 (Fig. 17F) and 7 (Fig. 17G). From the Madoonga deposit, diagenetic/metamorphic magnetite (Fig. 17H) is compared with Stage 2 magnetite representing the main stage of hypogene mineralization (Fig. 17I) at Madoonga and specular hematite from Stage 3 specular hematite-quartz veins (Fig. 17J). Summary data for LA-ICP-MS analysis of iron oxides are reported in Table A9, whereas individual analyses are reported in Table A10. Compositional data are presented as a series of box-and-whisker plots for elements considered to be most compatible in magnetite and hematite (Fig. 18).

Compositional ranges for magnetite and hematite from the Beebyn deposit

Least-altered BIF from the Beebyn deposit contains primary iron oxide-rich bands comprised of interlocked

diagenetic/metamorphic magnetite grains with <20 µm-diameter mineral inclusions of quartz, apatite, and ferroan dolomite (Fig. 17A). In situ LA-ICP-MS spot analyses were positioned away from obvious mineral inclusions in diagenetic/metamorphic magnetite. Accidental ablation of mineral inclusions in magnetite were identified by their prominent Si, P, Ca, Sr, or Mg spectral peaks in the collected data and were thereafter excluded from the finalized compositional data set. Diagenetic/metamorphic magnetite (n=23) mainly contains Si (upper threshold concentrations of 1943 to 72245 ppm), Ca (285 to 421 ppm), Al (77 to 198 ppm), Mg (24 to 198 ppm), Zn (23 to 35 ppm), Ni (22 to 32 ppm), Ti (11 to 29 ppm), K (11 to 26 ppm), Mn (6 to 17 ppm), and Sb (2 to 13 ppm) (Fig. 18). All other element concentrations are below 10 ppm, with individual REE values below 6 ppm.

Beebyn Stage 1 magnetite forms isolated grains or clusters of coarse-grained (<400 µm-diameter), hexagonal crystals surrounded by finer grained (<50 µm), crystalline ferroan dolomite (Fig. 17B). The cores of Stage 1 magnetite grains host abundant mineral inclusions of <40 µm ferroan dolomite. Laser ablation spot locations were positioned along the mineral inclusion-poor, edges of disseminated magnetite grains. Beebyn Stage 1 magnetite analyzed from the W8 and W9 prospects (n=27) comprise mainly Mg (1351 to 19523 ppm), Ca (190 to 9816 ppm), Si (430 to 4719 ppm), P (80 to 808 ppm), Mn (50 to 742 ppm), Al (18 to 335 ppm), Ni (18 to 225 ppm), K (14 to 119 ppm), Ti (31 to 63 ppm), V (5 to 56 ppm), Zn (18 to 41 ppm), Na (13 to 25 ppm), and Sb (3 to 14 ppm). All individual REE concentrations are below 2 ppm. Compared with diagenetic/metamorphic magnetite from the least-altered Beebyn BIF, Stage 1 magnetite is enriched in Mg (by up to two orders of magnitude), Mn (by one order of magnitude), with common enrichments in Ba, Mo, Na, P, Rb, Ti, and V, and more localized enrichments in As, Ca, K, Na, Pb, Sc, Sr, and W (Fig. 18). Stage 1 magnetite is commonly depleted in Si relative to diagenetic/metamorphic magnetite.

Beebyn Stage 3 magnetite is typified by <200 µm-long by <100 µm-wide, hemi-pyramidal crystals intergrown with Stage 3 ferroan dolomite (Fig. 17C). Stage 3 magnetite grains rarely contain mineral inclusions; however, their small grain size relative to the 75 µm-diameter laser beam resulted in few representative analyses for this alteration stage (n=8). Stage 3 magnetite contains Si (1554 to 5814 ppm), Ca (1666 to 3342 ppm), Mg (36 to 2806 ppm), W (0.2 to 1486 ppm), Al (95 to 768 ppm), Na (<153 ppm), Mn (2 to 126 ppm), K (<121 ppm), As (2 to 48 ppm), Ti (25 to 42 ppm), and V (6 to 22 ppm). Apart from Ce (0.1 to 0.5 ppm), REE concentrations are below detection limits. Relative to diagenetic/metamorphic magnetite, Stage 3 magnetite displays similar, but generally more pronounced, enrichment trends compared with Stage 1 magnetite (i.e. greater enrichments in As, Ba, Ca, K, Mo, Na, Pb, Sr, and W). Magnesium, Mn, Ti, and V are enriched in Stage 3 magnetite relative to diagenetic/metamorphic magnetite, but to a lesser extent than Stage 1 magnetite. Bismuth, Cr, Cu, Ge, and Nb are enriched solely in Stage 3 magnetite. Stage 3 magnetite is commonly depleted in Si relative to diagenetic/metamorphic magnetite. Diagenetic/metamorphic, Stage 1, and Stage 3 magnetite display comparable absolute abundances of Al, Ga, Sb, and Zr (Fig. 18).

Beebyn Stage 4 martite is the result of the in situ oxidation of Stage 1 magnetite to hematite (Fig. 17D). Stage 4 martite (n=18) contains mainly Si (4349 to 26144 ppm), Mg (106 to 559 ppm), Ca (<181 ppm), P (<132 ppm), Al (22 to 81 ppm), Ti (40 to 45 ppm), Na (17 to 26 ppm), K (13 to 24 ppm), and Mn (14 to 17 ppm), with all individual REE concentrations below 0.4 ppm. Compared with Stage 1 magnetite precursor grains, Stage 4 martite is enriched in Si, while depleted in Ca, Co, Cu, Mg, Mn, Ni, V, and Zn.

Stage 4 martite and Stage 1 magnetite display comparable abundances of As, Cr, Ga, Ge, Na, Pb, Ti, and W (Fig. 18). Beebyn Stage 4 specular hematite blades that are 1 cm-long by 0.5 cm-wide (Fig. 17E) (n=7) contains mainly Ca (188 to 7290 ppm), P (69 to 2304 ppm), Si (461 to 1267 ppm), Al (305 to 829 ppm), Ti (21 to 742 ppm), W (31 to 312 ppm), V (11 to 88 ppm), Na (13 to 63 ppm), Sb (9 to 51 ppm), Mg (1 to 50 ppm), Mn (1 to 50 ppm), As (3 to 44 ppm), K (9 to 36 ppm), and Cr (3 to 29 ppm). Stage 4 specular hematite is enriched in Light REE compared with Heavy REE, with individual Ce contents up to 4 ppm. REE normalized with respect to the Post-Archean Australian Shale (PAAS, McLennan, 1989) demonstrate a positive slope and a prominent positive Eu anomaly. Relative to Stage 4 martite, Stage 4 specular hematite is enriched in Al, As, Ba, Bi, Ca, Cu, Mo, Nb, P, Sb, Sc, Sr, Ta, Ti, U, V, and W, while depleted in Ge, Ni, and Si (Fig. 18).

Beebyn Stage 6 veins contain disseminated, irregular-shaped, <300 µm-diameter magnetite grains surrounded by ferroan dolomite (Fig. 17F). Inclusions of ferroan dolomite are locally present in the centre of magnetite grains. Stage 6 magnetite (n=11) comprises Ca (229 to 744 ppm), Mg (22 to 429 ppm), Si (187 to 1185 ppm), Al (59 to 159 ppm), Mn (4 to 43 ppm), K (20 to 38 ppm), Zn (15 to 29 ppm), Ni (11 to 18 ppm), and V (9 to 17 ppm). Apart from Er (0.05 ppm), all REE concentrations are below their respective detection limits. Relative to diagenetic/metamorphic magnetite, Stage 6 magnetite is enriched in Ba, Ge, Sr, and V, locally enriched in Mg and Mn, but depleted in Si, Sb, Ni, W, and Ti (Fig. 18). Stage 6 magnetite displays similar compositional ranges with Stages 1 and 3 magnetite, although their enrichments relative to diagenetic/metamorphic magnetite are more subdued. Stage 6 magnetite contains the lowest abundance of Si compared with all other analyzed magnetite.

Beebyn Stage 7 magnetite in siderite-chlorite-magnetite veins form <500 µm-diameter, hexagonal grains that are surrounded by finer-grained chlorite or siderite (Fig. 17G). Magnetite grains host minor <5 µm-diameter inclusions of siderite. Stage 7 magnetite (n=6) contains Ca (1328 to 9369 ppm), Mg (135 to 2630 ppm), P (182 to 1685 ppm), Si (546 to 1090 ppm), Mn (9 to 169 ppm), Al (55 to 147 ppm), and Ti (133 to 145 ppm), with lower abundances of K (20 to 27 ppm), Na (21 ppm), Zn (10 to 20 ppm), Ni (14 to 17 ppm), and Ge (9 to 14 ppm). Rare earth elements are minor constituents (e.g. La <1.3 ppm, Ce <2.9 ppm, Pr <0.4 ppm, and Nd <1.6 ppm). Compared with diagenetic/metamorphic magnetite, Stage 7 magnetite is enriched in As, Ba, Ca, Ge, Mg, Mn, Mo, Na, P, Pb, Rb, Sr, Ti, and V (Fig. 18). Stage 7 magnetite is depleted in Si and Zn relative to diagenetic/metamorphic magnetite.

Compositional ranges for magnetite and hematite from the Madoonga deposit

Least-altered BIF from the Madoonga deposit contains bands of diagenetic/metamorphic magnetite with abundant <5 µm inclusions of recrystallized quartz (Fig. 17H). Compared with the Beebyn samples, relatively few mineral inclusion-free magnetite grains were large enough for ablation. Madoonga diagenetic/metamorphic magnetite (n=3) contains mostly Si (4046 to 21553 ppm), Mn (530 to 797 ppm), Mg (208 to 210 ppm), Al (19 to 25 ppm), Na (21 to 22 ppm), and Ni (9 to 10 ppm). Apart from Ce (0.16 ppm) and La (0.01 ppm), all REE are below their respective detection limits. Compared with diagenetic/metamorphic magnetite from the Beebyn deposit, Madoonga examples are enriched in Mn, Ti,

and Pb, and depleted in Al, Zn, V, Ni, and Co (Fig. 18).

Madoonga Stage 2 magnetite-talc±apatite±monazite±xenotime veins locally contain amalgamated grains of hypogene magnetite separated by talc (Fig. 17I). Stage 2 magnetite from the latter occurrences (n=35) mainly contains Si (577 to 4839 ppm), Ca (284 to 1707 ppm), P (190 to 1261 ppm), Mg (30 to 543 ppm), Al (18 to 408 ppm), Na (14 to 131 ppm), Mn (37 to 109 ppm), Ti (10 to 23 ppm), Ni (5 to 14 ppm) and Zn (2 to 35 ppm). Individual REE concentrations are <5 ppm, with Light REE more abundant than Heavy REE. Relative to diagenetic/metamorphic magnetite in the least-altered Madoonga BIF, Stage 2 magnetite is enriched in Ca, Cr, K, Mo, P, Sc, Ti, U, and V, while depleted in Mn and Si (Fig. 18).

Madoonga Stage 3 specular hematite blades (Fig. 17J) (n=22) contain mostly Si (299 to 1764 ppm), Al (7 to 419 ppm), P (<75 ppm), Na (14 to 112 ppm), Mg (1 to 37 ppm), and Mn (3 to 30 ppm). REE are very minor constituents, with individual abundances <1.6 ppm. Relative to Madoonga diagenetic/metamorphic magnetite and Stage 2 magnetite, Madoonga Stage 3 specular hematite displays comparable trace element abundances, but is depleted in Cr, K, Mg, Mn, Ni, P, Si, Ti, and V. Compared with Beebyn Stage 4 specular hematite, Madoonga Stage 3 specular hematite is enriched in Zn, but depleted in Bi, Ca, Co, Cr, K, Mg, Mo, P, Sb, Sn, Ta, Th, Ti, V, and W (Fig. 18).

Interpretation of Fluid and Mineral Chemistry Data

Microthermometry data: fluid composition and trapping conditions

Microthermometry data for the Beebyn deposit demonstrate a transition in fluid homogenization temperatures and salinities with time (Fig. 11 and Fig. 19); from early higher-temperature carbonic (Beebyn Stage 1) fluids to lower-temperature aqueous (Stage 2) fluids responsible for the replacement of primary quartz bands by hypogene carbonate minerals in BIF, to aqueous-rich fluids that removed hypogene carbonate minerals to form high-grade magnetite-rich ore (Beebyn Stage 3). The presence of vapor-rich Stage 1 carbonic fluid inclusions suggests phase separation and related fluid immiscibility may have operated during the early replacement of primary quartz bands by hydrothermal fluids at the Beebyn deposit. However, all subsequent aqueous fluid inclusion assemblages show similar phase ratios at room temperature (Fig. 8 and Fig. 9), suggesting that phase separation was not a trigger for crystallization of iron oxide minerals in these deposits (cf. Shepherd et al., 1985).

At the Beebyn deposit, large variations exist in Stage 2 fluid total homogenization temperatures and calculated salinities for fluid inclusion assemblages measured from samples spanning the 4 km strike-length of the ferroan dolomite alteration halo (Fig. 11B and C). The Stage 2 fluid event is characterized by the localized trapping of (i) higher-temperature/ higher-salinity fluids in the W10 prospect (>275 to 327 ºC; 36 to 40 equiv. wt% NaCl), (ii) moderate-temperature/ low- to moderate-salinity fluids in the W8 and W10 prospects (>225 to 260 ºC; 3 to 24 equiv. wt% $CaCl_2$), as well as (iii) lower-temperature/ low- to moderate-salinity fluids in the W10 prospect (>125 to 180 ºC; 2 to 24 equiv. wt% $CaCl_2$) (Fig. 19A). These temperature and salinity observations for the Stage 2 fluid inclusion assemblages are best explained by the progressive trapping of multiple pulses of hydrothermal fluid with similar major cation components, but varying in temperature and salinity through time and with proximity to central fluid pathways.

The Beebyn Stage 3 fluid, responsible for the replacement of Stage 2 ferroan dolomite by Stage 3 magnetite and minor reprecipitation of ferroan dolomite, has a total homogenization temperature and salinity (>98 to 175 ºC; 4 to 18 equiv. wt% $CaCl_2$) that overlaps the lower-temperature range of Stage 2 fluids (Fig. 19A). The lower temperature of Stage 3 fluids, whose timing coincides with the net removal of hypogene carbonate from BIF, suggests that the retrograde solubility of carbonate minerals may have been important in forming high-grade magnetite ore at the Beebyn deposit.

Post-ore Beebyn Stage 5 fluids hosted by hydrothermal quartz replacement zones have comparable final homogenization temperatures and cations to the preceding hydrothermal fluids (Fig. 11), but Stage 5 fluids are more saline and likely Si-rich. More localized occurrences of Beebyn Stages 6 and 7 magnetite-carbonate veins formed from hydrothermal fluids that have final homogenization temperatures and calculated salinities that are most similar to Stage 3 hydrothermal fluids (Fig. 11 and Fig. 19).

At the Madoonga deposit, Stage 3 fluids responsible for specular hematite-quartz veins display total homogenization temperature and salinity ranges that overlap data for Beebyn Stage 2, 3, 6, and 7 fluids (Fig. 19). Vein occurrences at the Madoonga W19 prospect host fluids that are more saline and $CaCl_2$-dominant, compared with the lower-salinity and NaCl-dominant fluids recorded from the W15 prospect. The trapping of two compositionally distinct fluids at similar temperature ranges in these prospects, which are spaced 10 km apart, suggests that their source fluids were potentially controlled by their local environment but they share a global control such as changes in temperature or oxidation state that triggers precipitation of specular hematite in their respective areas.

Ion chromatography data: fluid compositions and sources

Molar Cl/Br ratios are useful indicators for the source of salinity in hydrothermal fluids because, in the absence of halite, Cl and Br are not significantly involved in fluid-rock interactions (Banks et al., 1991; Bohlke and Irwin, 1992; Kesler et al., 1995; Banks et al., 2002; Lüders et al., 2005). Seawater has a molar Cl/Br ratio of 655 (Fig. 20A) and evaporation of seawater to the point of halite saturation does not change this ratio, but once halite precipitation occurs the molar Cl/Br ratio decreases to 240 at the end of halite precipitation (Banks et al., 2002). Further evaporation produces fluids that are even more Br rich (Lüders et al., 2005). In contrast, the dissolution of halite, such as from sedimentary evaporite deposits, results in Br-poor fluids with a large range in molar Cl/Br ratios from about 1000 to 20000 (Fontes and Matray, 1993). Unlike molar Cl/Br ratios, molar ratios for Na/Cl, Na/Br, Na/K, and Na/SO_4 can be influenced by fluid-rock interactions. They are particularly affected by interaction between the fluids and Na-K-bearing minerals, such as feldspar minerals.

Molar Cl/Br ratios for the analyzed fluids from the Beebyn and Madoonga deposits are mostly higher than the ratio for Archean and modern seawater values, indicating that these fluids dissolved halite through wallrock fluid-rock interactions prior to trapping by their mineral hosts (Fig. 20A). Beebyn Stage 2 fluids, with molar Cl/Br ratios of 1000 to 2000, most closely overlap the compositional range for magmatic-derived fluids as reported by existing studies (Bohlke and Irwin, 1992; Johnson et al., 2000; Banks et al., 2000b; Kendrick et al., 2001; Banks et al., 2002; Baker et al., 2006), with very good correspondence with magmatic fluid compositions compiled by Yardley (2013) and Yardley and Bodnar (2014) (Fig. 20C),

although the Cl/Br values do overlap the broader fields for low-grade metamorphic fluids and oil field formation waters (Fig. 20A to F). Beebyn Stage 3 fluids display a broad range of molar Cl/Br values from 380 to 2350. The highest of the two molar Cl/Br values is similar to the signature for Beebyn Stage 2 values, but might be influenced by accidental incorporation of fine-grained Stage 2 magnetite and carbonate minerals with the Stage 3 mineral separates during sample preparation. The lower Cl/Br ratio (~400) for the Stage 3 fluid is similar to Cl/Br ratios for Archean seawater buffered by vent fluids (data reported by De Ronde et al., 1997) (Fig. 20B). However, the Stage 3 Cl/Br values must be treated with caution considering that the measured Br contents for these fluids are close to the analytical detection limits. Beebyn Stage 5 fluids define a molar Cl/Br trend that overlaps the range of Stage 2 fluids and magmatic-derived fluid fields, but also extends towards higher Cl/Br values, thus sharing compositional affinities with low-grade metamorphic fluids, geothermal brines, and oil field formation waters (Fig. 20A). The single Cl/Br value for the Madoonga Stage 2 fluid is higher than any value determined for the Beebyn deposit, but overlaps the range of Cl/Br values for Madoonga Stage 3 fluids; these Madoonga Stages 2 and 3 fluids are compatible with low-grade metamorphic fluids, geothermal brines, or oil field formation waters (Fig. 20A).

A measure of fluid-rock interaction is indicated by molar Na/Cl, Na/Br, Na/K, Na/SO_4, and Cl/SO_4 ratios in Fig. 20 and by the molar Cl/Br versus molar Ca/Ca+Na ratios in Fig. 21A. The analyzed fluids have molar Na/Cl ratios of 0.1 to 0.8, which indicates that other cations are required to be present to balance the anions and cations. Beebyn Stage 2 fluids, with the lowest molar Na/Cl and Na/Br ratios, and the highest range of Ca/Ca+Na ratios (Fig. 20A, Fig. 20B and Fig. 21A), are likely to contain the greatest abundance of cations substituting for Na. Corresponding LA-ICP-MS data from fluid inclusions confirm that these fluids contain Fe, Ca, Mg, and Mn in decreasing order of abundance (Fig. 14). Molar NaCl and Na/Br ratios vary considerably for most of the analyzed fluids, depending on the extent of interaction between the fluids and surrounding mafic igneous rocks that are rich in Fe, Ca, Mg, and Mn-bearing minerals. Intense chloritization of igneous amphibole and plagioclase in neighboring mafic igneous rocks, combined with depletions in whole rock geochemical values for CaO, K_2O, and Na_2O in these altered mafic rocks (Duuring and Hagemann, 2013b), independently corroborates the inferred chemical exchange between these cations in the hydrothermal fluids and country rocks. The presence of sulfide minerals associated with Beebyn Stages 3 and 5 alteration mineral assemblages (Fig. 3) explains the lower Cl/SO_4 ratios for these trapped fluids (Fig. 20E). The very low Cl/SO_4 ratios for Madoonga fluids suggests the fluids interacted with semi-massive sulfides that are locally present in shale along the southern margin of the South BIF at the Madoonga deposit.

Variations in the molar Na/K ratios for the fluids record a combined signature of the fluid source and a measure of the interaction with feldspars in country rocks (Fig. 20C). Fig. 21B shows a comparison of K/Na ratios determined for fluids from crush-leach and LA-ICP-MS fluid data sets versus their corresponding minimum trapping temperatures estimated from microthermometry studies. Two main fluid compositional-temperature groups are shown. A higher-temperature group defined by Stage 2 Beebyn and Stage 2 Madoonga fluids overlaps the fields for black smoker fluids and geothermal brines. In contrast, the lower-temperature data defined by Beebyn Stages 3 and 5 fluids, and Madoonga Stage 3 fluids, show a wider spread in K/Na ratios, trending away from the microcline-albite equilibrium curve (dashed line),

indicating their likely interaction with feldspars in country rocks. These fluids are most compatible with bittern brines formed from the dissolution of halite, and oil field formation waters (Fig. 21B).

In situ LA-ICP-MS data for fluid inclusions: fluid compositions and sources

All analyzed fluid inclusions from the Beebyn deposit contain Fe, Ca, Mg, Mn, Na, and K (Fig. 14), compatible with observed initial melting temperatures of -40 to -68 ºC for these fluid inclusions (Fig. 11). Madoonga Stage 3 fluid inclusions from the W19 prospect have similar cation ratios to the Beebyn fluids, although a subset of lower-salinity fluids analyzed from the W15 prospect are richer in NaCl (Fig. 11).

Manganese content is the best discriminator for fluids analyzed from the Beebyn and Madoonga deposits (Fig. 22A). Beebyn Stages 2, 3, and 6 fluids display higher Mn/Na ratios relative to other measured fluids and are most compatible with reported data for magmatic fluids, black smoker fluids, and geothermal brines (Fig. 22A). Beebyn Stage 5 and Madoonga Stage 3 fluids overlap the data ranges for geothermal brines, low-grade metamorphic fluids, and basinal brines from basement rocks (Yardley and Bodnar, 2014; James et al., 2014). Based on a comparison of Fe, Zn, and Pb contents of fluid inclusions, most analyzed fluids from Beebyn and Madoonga are compatible with a modified brine that has reacted with an evaporite, with some Beebyn Stage 5 fluids demonstrating possible variation between end-member compositions of modified and unmodified brines (Fig. 22B). Fluids from the Beebyn and Madoonga deposits are preferentially enriched in Cu and Zn compared with Pb, showing an affinity with Cu-Zn ratios in volcanogenic massive sulfide (VMS) deposits rather than more Pb-rich SEDEX deposits.

Carbon and oxygen isotope data: fluid sources

Hydrothermal quartz from semi-massive pyrite-quartz veins hosted by mudstone along the Madoonga South BIF has calculated $\delta^{18}O_{H2O}$ values (4.70 to 6.15 ‰) that overlap the reported values for mantle and metamorphic fluids, but are slightly more negative than the reported range for magmatic fluids (Sharp, 2006) (Fig. 16). The isotope values for the semi-massive pyrite-quartz veins most likely record isotopic exchange between a blend of magmatic and Archean seawater signatures through fluid mixing. Later metamorphic fluids may also have affected $\delta^{18}O_{H2O}$ values.

Beebyn Stage 1 CO_2-rich fluids have the most positive $\delta^{18}O_{H2O}$ values measured from either deposit; their paired $\delta^{18}O_{H2O}$ and $\delta^{13}C_{CO2}$ values overlap reported ranges for magmatic, carbonatite, and metamorphic fluids (Fig. 16). The higher-temperature/ higher-salinity subset of Beebyn Stage 2 fluids define a narrow $\delta^{13}C_{CO2}$ range (i.e. from -7.03 to -6.54 ‰), but a wide range of corresponding $\delta^{18}O_{H2O}$ values (0.99 to 7.42 ‰). The calculated $\delta^{13}C_{CO2}$ values overlap the ranges for mantle, magmatic, and metamorphic fluids, whereas the more negative $\delta^{18}O_{H2O}$ values suggest that Beebyn Stage 2 fluids interacted with Archean seawater or meteoric waters, resulting in a negative shift in $\delta^{18}O_{H2O}$ values while preserving the initial $\delta^{13}C_{CO2}$ values of the hydrothermal fluids. In comparison, the lower-temperature/ low- to moderate-salinity Beebyn Stage 2 fluids have more negative $\delta^{13}C_{CO2}$ values (i.e. from -10.36 to -10.11 ‰) (Fig. 16). In the likely absence of methane in the fluid inclusions, the more negative $\delta^{13}C_{CO2}$ values for lower-temperature Beebyn Stage 2 fluids suggest interaction with rocks that contain organic carbon, which

can have $\delta^{13}C$ values as low as -41.4 ‰ (Bekker et al., 2014). Corresponding low $\delta^{18}O_{H2O}$ values (-0.45 to 1.01 ‰) for these fluids suggest interaction with Archean seawater or meteoric waters.

Post-ore Beebyn Stages 5 and 6 fluids have $\delta^{18}O_{H2O}$ values (-2.84 to 2.05 ‰) that overlap values for lower-temperature Beebyn Stage 2 fluids, but their isotopic range extends to more negative $\delta^{18}O_{H2O}$ values, compatible with greater interaction with Archean seawater or meteoric waters. Corresponding $\delta^{13}C_{CO2}$ values for Beebyn Stage 6 fluids (-5.47 to -10.97 ‰) display a similar range to Beebyn Stage 2 fluids, suggesting interaction with organic carbon.

Madoonga Stage 3 high-salinity fluids in the specular hematite-quartz veins from the W19 prospect have calculated $\delta^{18}O_{H2O}$ values (-6.73 to -6.34 ‰) that are significantly more negative than any fluid analyzed from the Beebyn deposit, or reported values for mantle, magmatic, and metamorphic fluids (Fig. 16). Instead, Madoonga Stage 3 $\delta^{18}O_{H2O}$ fluid values overlap the isotopic ranges for Archean seawater as defined by Prokoph et al. (2008) and meteoric waters, suggesting that the Stage 3 fluids may be derived from combinations of both sources.

Post-ore Madoonga Stages 4 and 6 fluids display a large range in $\delta^{13}C_{CO2}$ and $\delta^{18}O_{H2O}$ values, including some of the most negative values determined from either deposit. The large range in values suggests the influence of several possible isotope sources, such as organic carbon in the pyritic mudstone (producing negative $\delta^{13}C_{CO2}$ values) and meteoric fluids or Archean seawater (resulting in negative $\delta^{18}O_{H2O}$ values).

Iron oxide mineral chemistry data: fluid compositions and sources

Magnetite and hematite are recognized petrogenetic indicators; their trace element abundances and element ratios have been used to constrain fluid sources and discriminate ore deposit types, including Ni-Cu-PGE and Cr (Dupuis and Beaudoin, 2011; Boutroy et al., 2014), Iron Oxide Copper-Gold and Iron Oxide-Apatite (Dupuis and Beaudoin, 2011), VMS deposits (Singoyi et al., 2006; Makvandi et al., 2016), carbonatite in Phalaborwa (Milani et al., 2016), as well as porphyry Cu-Mo, skarn, Ag-Pb-Zn veins, and BIF (Dupuis and Beaudoin, 2011; Nadoll, 2011; Nadoll et al., 2014). Recently, magnetite and hematite compositions have been used to identify the involvement of metamorphic and hydrothermal fluids in the genesis of high-grade iron orebodies hosted by BIF in the Quadrilátero Ferrífero, Brazil (Cabral and Rosière, 2013; Hensler et al., 2015), and the Koolyanobbing and Marda greenstone belts, Western Australia (Angerer et al., 2012; Angerer et al., 2013). Divalent cations such as Mg, Ni, Mn, Co, and Zn may substitute for Fe^{2+} sites in magnetite; trivalent cations such as Al, Cr, V, Mn, and Ga replace Fe^{3+} sites in magnetite or hematite (Lindsley, 1976; Wechsler et al., 1984), whereas cations with higher valencies (e.g. Ti^{4+}, $V^{4,5+}$, $Cr^{4,5,6+}$) can occupy Fe^{3+} sites when substitution is coupled with a divalent cation (Wechsler et al., 1984). Consequently, Mg, Al, Ti, V, Cr, Mn, Co, Ni, Zn, and Ga are the main discriminator elements for magnetite (Nadoll et al., 2014), whereas Al, Cr, V, Mn, Ga, and Ti are useful for hematite (Lindsley, 1976; Hensler et al., 2015). In the case of magnetite, numerous case studies and reviews demonstrate that its chemistry is influenced by the composition of the magma (relevant for magmatic magnetite), the composition of the host rocks and fluid phases (in metamorphic and hydrothermal magnetite), as well as a range of physical-chemical fluid properties, including temperature, pressure, rate of cooling, oxygen

fugacity, silica activity, the ionic radius and overall charge balance of substituting elements, and the composition of coeval minerals and partition coefficients of various substituting elements between competing mineral phases (Goldschmidt, 1954; Buddington and Lindsley, 1964; Fleet, 1981; Wechsler et al., 1984; Whalen and Chappell, 1988; Frost and Lindsley, 1991; Ghiorso and Sack, 1991; Haggerty, 1991; Cornell and Schwertmann, 2003; Carew et al., 2006; Nadoll, 2011; Dare et al., 2012; Mollo et al., 2012; Biagioni and Pasero, 2014; Dare et al., 2014; Nadoll et al., 2014). Recent case studies on hydrothermal hematite have demonstrated similar controls on hematite chemistry (cf. Figueiredo e Silva et al., 2009; Cabral and Rosière, 2013; Hensler et al., 2015).

Diagenetic/metamorphic magnetite in BIF units Iron oxide-rich bands in least-altered BIF from the Beebyn and Madoonga deposits comprise magnetite with accessory mineral inclusions of quartz, apatite, and stilpnomelane (Fig. 17). These magnetite-rich bands are overgrown by diagenetic/metamorphic magnetite that is devoid of mineral inclusions. Diagenetic/metamorphic magnetites from both deposits contain high Si contents compared with their respective later generations of hypogene magnetite (Fig. 18). The high abundance of Si in diagenetic/metamorphic magnetite is likely due to the presence of sub-micrometre mineral inclusions of quartz in the magnetite, or the incorporation of Si into the magnetite crystal lattice, or both. For comparison, magnetite mesobands from the Dales Gorge Member of the Brockman Iron Formation, Hamersley Group, Western Australia reportedly contains 1 to 3 wt% SiO_2 (equivalent to 4674 to 14032 ppm Si) (Huberty et al., 2012). This study demonstrated by applying in situ micro-X-ray diffraction and high-resolution transmission electron microscopy techniques that Si solid solution is present in the magnetite crystal lattice. Furthermore, a compilation by these authors of 32 prior studies on magnetite chemistry from multiple rock types and ore deposits, shows a range in SiO_2 of up to 8 wt% (i.e. 37392 ppm Si) (references included in Huberty et al., 2012). In the iron oxide-rich bands of the Dales Gorge Member, the low-Si magnetite domains that host abundant mineral inclusions are interpreted to have formed during soft-sediment deformation. Whereas, the Si-rich magnetite overgrowths, which are likely to be comparable with the diagenetic/metamorphic magnetite observed at the Beebyn and Madoonga deposits, are either diagenetic or low-temperature (sub-greenschist facies) burial metamorphic in origin (Huberty et al., 2012).

Least-mobile, compatible element abundances (e.g. Ga and Al) in diagenetic/metamorphic magnetite from the Beebyn deposit define one main cluster, with minor compositional variation (Fig. 23A). In comparison, it is not possible to accurately determine Ga/Al ratios for diagenetic/metamorphic magnetite analyzed from the Madoonga deposit due to the low absolute abundance of Ga in the diagenetic/metamorphic magnetite. However, by assuming Ga concentrations at half their detection limits, the resultant Ga and Al-paired data for Madoonga diagenetic/metamorphic magnetite are likely to plot closer to the axis of the plot, away from data for Beebyn, but potentially along a linear trend that passes through the clustered data for Beebyn diagenetic/metamorphic magnetite (Fig. 23A). From this evidence, both groups of diagenetic/metamorphic magnetite are likely to display similar Ga/Al ratios, with minor variations caused by local differences in depositional conditions, or the minor mobility of these elements during later hydrothermal alteration events, or combinations of both influences. Madoonga diagenetic/metamorphic magnetite contains higher abundances of Mn, Ti, and Pb, but most other trace elements are comparable (Fig. 18).

The comparable magnetite-quartz±apatite±stilpnomelane mineral associations between the Beebyn and Madoonga deposits, their shared textural relationships (with early mineral inclusion-rich magnetite and overgrowths of diagenetic/metamorphic magnetite), their high abundance of Si and mutually similar concentrations of other trace element constituents (and potentially comparable Ga/Al ratios) in diagenetic/metamorphic magnetite, all support the interpretation that the diagenetic/metamorphic magnetite and least-altered BIF from the Beebyn and Madoonga deposits share a similar depositional history with a metamorphic fluid overprint. The absence of compositional heterogeneity within analyzed iron oxide bands from the Beebyn deposit suggests that peak metamorphism involved localized dissolution of existing diagenetic or early-stage diagenetic/metamorphic magnetite, and re-precipitation of peak-metamorphic magnetite, without significant differences in their composition.

Hypogene magnetite in BIF The Beebyn Stage 1 alteration event is characterized by widespread replacement of primary and diagenetic/metamorphic quartz by Stage 1 ferroan dolomite, precipitation of Stage 1 magnetite as overgrowths on existing magnetite and crystallization of new crystals, and the local formation of apatite as an accessory mineral. The clear depletion of Si in Stage 1 magnetite and replacement of existing quartz indicates that the Stage 1 hydrothermal fluid was Si-poor. Whereas, major enrichments in Mg, Mn, Ca, Sr, Ba, Mo, As, Pb, and W in Stage 1 magnetite (Fig. 23B and C), through their incorporation into the crystal lattice of Stage 1 magnetite and/or crystallization as sub-micrometre- to micrometre-sized mineral inclusions of ferroan dolomite or apatite, suggest that these elements were added to BIF from the Stage 1 hydrothermal fluid. These enrichment patterns can be clearly demonstrated in a number of discrimination diagrams whose principle constituents include Mg, Mn, and Ti (Fig. 23). The Al+Mn versus Ti+V plot, with deposit fields from Dupuis and Beaudoin (2011), Nadoll (2011), and Nadoll et al. (2014), clearly differentiates Beebyn Stage 1 magnetite from diagenetic/metamorphic magnetite, likely owing to a higher abundance of Mn and Ti in Stage 1 magnetite (Fig. 23D). On this discrimination plot, Beebyn Stage 1 magnetite bears closest compositional affinity with examples of hydrothermal magnetite sampled from Ag-Pb-Zn veins (Fig. 23D). A comparison of Ga and Al abundance and Ga/Al ratios between Stage 1 magnetite and diagenetic/metamorphic magnetite (Fig. 23A and E) demonstrates that Stage 1 magnetite likely inherited its Ga/Al signature from existing diagenetic/metamorphic iron oxides during Stage 1 hydrothermal fluid interaction with the BIF, suggesting the local dissolution and re-crystallization of diagenetic/metamorphic magnetite as Stage 1 magnetite.

Beebyn Stage 3 magnetite displays comparable enrichment and depletion patterns to Stage 1 magnetite (Fig. 18), indicating that both generations of hypogene magnetite precipitated from compositionally similar hydrothermal fluids. The more pronounced enrichments in Cu, As, W, Sr, Mo, Pb, and Ca in Stage 3 magnetite suggest that Stage 3 hydrothermal fluids contained higher abundances of these elements, or that these element concentrations were upgraded via the local dissolution of existing, trace metal-rich, Stage 1 magnetite. These enrichment trends in the Stage 3 magnetite are supported by the confirmed presence of accessory sulfide minerals containing Fe, Cu, Pb, Zn, As, Ni, Co, Sb, and Ag, and a W-bearing mineral.

Post-ore Beebyn Stages 6 and 7 magnetite-rich veins have a more restricted spatial distribution in the Beebyn deposit compared with diagenetic/metamorphic minerals and Stages 1 and 3 alteration mineral

assemblages. Stage 6 magnetite is compositionally most similar to diagenetic/metamorphic magnetite (displaying comparable Ga/Al, Al+Mn/Ti+V, Mg/W versus Mn/Al ratios; Fig. 23), although it bears many of the geochemical hallmarks that characterize earlier stages of hypogene alteration at Beebyn (i.e. local enrichments in Ba, Mg, Mn, Sr, and V, and depletions in Si; Fig. 23). Stage 7 magnetite also displays trace element abundances, Ga/Al, and Al+Mn/Ti+V ratios that suggest that they represent intermediate compositional states between metamorphic magnetite and Stages 1 and 3 magnetite end-member compositions. The restricted spatial occurrences of Stages 6 and 7 veins at Beebyn and their likely compositional dependence on existing magnetite suggests that they formed from relatively low volumes of hydrothermal fluids (compared with Stages 1 and 3 fluids). The compositions of these post-ore fluids were buffered by the greater volume of BIF wallrock that they passed through prior to precipitating magnetite in Stages 6 and 7 veins.

An accurate comparison between diagenetic/metamorphic magnetite and Stage 2 magnetite from the Madoonga deposit is hindered by the small number of analytical data available for Madoonga diagenetic/metamorphic magnetite (n=3). Both generations of magnetite display overlapping element abundances for least-mobile compatible elements (Fig. 18), and in some cases, comparable Ga/Al ratios (Fig. 23A), indicating the likely inheritance of these elements from Madoonga diagenetic/metamorphic magnetite. Madoonga Stage 2 magnetite displays the same depletion in Si relative to diagenetic/metamorphic magnetite that is shown by Stages 1 and 3 magnetites at the Beebyn deposit. Furthermore, these stages of hypogene magnetite from both deposits show mutual enrichments in Ca, Mo, Ti, V, and K. Madoonga Stage 2 magnetite is uniquely enriched in U, whereas Beebyn Stages 1 and 3 are enriched in Mg, Mn, Sr, Ba, Na, As, Pb, and W. Beebyn Stage 1 magnetite and Madoonga Stage 2 magnetite are clearly distinguished from each other in the Mg/W versus Mn/Al (Fig. 23B) and the Al+Mn versus Ti+V (Fig. 23D) discrimination plots.

Hypogene specular hematite veins and martitization of BIF wallrock Beebyn Stage 4 martite is derived from the oxidation of disseminated euhedral Stage 1 magnetite (e.g. Eq. 1 and Eq. 2).

Eq. 1 $2Fe_3O_4 + 0.5O_{2aq} \rightarrow 3Fe_2O_3$

Eq. 2 $2Fe_3O_4 + H_2O_L \rightarrow 3Fe_2O_3 + H_2$

Stage 4 martite grains have a similar Ga/Al ratio (albeit with minor Al-depletion) to diagenetic/metamorphic magnetite and Stage 1 magnetite from the Beebyn deposit (Fig. 23A). Other trace element enrichment and depletion patterns in Stage 4 martite compared to its precursor Stage 1 magnetite are best explained by documented differences in cation substitution tendencies between magnetite and hematite (Nadoll et al., 2014). That is, Beebyn Stage 4 martite has most likely inherited compatible trivalent cations (e.g. Cr, Ga, Al, As, Ti, and W) from Stage 1 magnetite. Whereas, Stage 4 martite is depleted in divalent cations, such as Cu, Mg, and Zn, which are less compatible in hematite. Divalent elements that are redox sensitive and possess higher valency states in oxidized conditions (e.g. Co, Mn, Ni, and V) are mostly depleted in Stage 4 martite. This strongly suggests that the Stage 4 hydrothermal fluids that oxidized magnetite were not enriched in these metals, but rather scavenged them through fluid interaction with existing magnetite. The strong enrichment of Si in Stage 4 martite relative to Stage 1 magnetite is compatible with the Beebyn Stage 4 specular hematite-chlorite alteration mineral assemblage in BIF.

Beebyn Stage 4 specular hematite-chlorite-altered shear zones and veins, which are surrounded by meter-wide zones of martite-altered BIF, cut high-grade Stages 1 and 3 magnetite-rich ore zones in BIF. These Stage 4 specular hematite-rich shear zones and veins represent areas of greater hydrothermal fluid flow through BIF where new specular hematite grains crystallize; in contrast to the more distal BIF wallrock zones where hydrothermal fluids are more likely to be buffered by rock chemistry and where earlier stages of magnetite are replaced by Stage 4 martite. Consequently, the composition of Beebyn Stage 4 specular hematite is directly influenced by the chemistry of the Stage 4 hydrothermal fluid (i.e. specular hematite demonstrates unique enrichments in Nb, Sb, Sc, Sn, Ta, and U), as well as by compositional inheritance from Stages 1 and 3 magnetite (i.e. demonstrating similar abundances in Al, As, Ba, Bi, Ca, Cu, Mo, P, Sn, Sr, Ti, V, and W).

Madoonga Stage 3 specular hematite demonstrates similar element abundances and depletion patterns compared to Beebyn Stage 4 specular hematite (Fig. 18 and Fig. 23B), indicating shared compositional dependencies based on known element compatibility differences between magnetite and hematite. Madoonga specular hematite preserves many of the element enrichment patterns recorded by earlier diagenetic/metamorphic magnetite and Stage 2 magnetite, indicating some inheritance of elements from earlier magnetite generations.

Fluid-alteration Model for Hypogene Iron Mineralization at Weld Range

Magnetite replacement-style orebodies

Magnetite-rich orebodies at the Beebyn deposit are the product of a multistage fluid event (Beebyn Stages 1 to 3) affecting BIF over an aerial extent of at least of 8 km. The timing of this event post-dates the diagenesis of the BIF and emplacement of the c. 2805 Ma (Wingate et al., 2012) mafic-ultramafic rocks of the Gnanagooragoo igneous complex because both rock types are locally altered by these ore fluids. The fluid event pre-dates the regional upright folding and steep tilting of the Weld Range lithotectonic unit. Early macro-scale faults that controlled fluid movement are not easily recognized at the Beebyn deposit because of their likely transposition during folding to orientations that are now subparallel to lithological contacts; however, the lens geometries and irregular distribution of several discrete alteration zones spaced across the 8 km lateral extent of the deposit (Fig. 2) suggests that such structures were important for repeatedly focussing fluids in the BIF, resulting in superimposed alteration zones and the magnetite replacement-style orebodies (Fig. 24). A synthesis of hypogene fluid data and interpretations for the Beebyn deposit is presented in Table 1, whereas an extended comparison is available in Table A11.

Stage 1: high-temperature, magmatic-derived fluids The Stage 1 fluid alteration event is the first of three successive fluid events affecting BIF. The Stage 1 event is responsible for the replacement of primary quartz bands by fine-grained siderite, ferroan dolomite, and magnetite, while preserving the original band thickness of BIF. Textural relationships demonstrate that the primary quartz bands were more reactive than

iron oxide-rich bands, with the latter bands experiencing limited growth of hypogene magnetite along the surfaces of existing magnetite grains. Stage 1 fluids were likely focussed along first-order faults that transect the BIF and mafic igneous country rocks (Fig. 24A). Mineral replacement progressed away from these large structures, laterally across reactive quartz bands. However, the additional local presence of carbonate mineral-filled veinlets cutting primary iron oxide-rich bands suggests that this process was enhanced by the creation of secondary, fracture-controlled permeability in BIF, allowing fluid migration across iron oxide-rich bands via linking fractures. The sealing of fluid pathways by precipitated carbonate minerals and the associated decrease in rock permeability led to cyclic increases in fluid pressures and subsequent hydraulic fracturing of BIF, thereby sustaining the widespread migration of the Stage 1 fluid at the Beebyn deposit.

Stage 1 fluids were high-temperature (>444 °C), silica-poor, reduced, alkaline, and CO_2-rich at the site of their trapping by carbonate minerals (interpreted from Stage 1 alteration mineral assemblages, stable isotopes, and fluid inclusion composition). Paired O and C stable isotope data for Stage 1 ferroan dolomite suggest that these fluids had a magmatic source, while Stage 1 magnetite chemistry indicates significant chemical exchange took place between these fluids and mafic igneous rocks prior to crystallization of the magnetite in BIF (i.e. enrichments in Mg, Mn, Ca, and Na). The monophase carbonic Stage 1 fluids trapped by ferroan dolomite are likely sourced from bicarbonate-rich aqueous fluids that separated into volatile-rich and brine phases in deeper parts of the hydrothermal system, most likely as a result of phase separation triggered by a rapid drop in confining and hydrostatic fluid pressures due to rock fracturing (Ramboz et al., 1982; cf. Yardley and Bodnar, 2014).

The Beebyn Stage 1 desilicification-carbonate replacement process involved the alteration of quartz bands to ferroan dolomite or siderite by abundant hot, reduced, silica-poor, bicarbonate-rich aqueous fluids. Quartz replacement was assisted by the high temperature and reduced conditions of the fluid since quartz solubility (Eq. 3) is promoted by increasing fluid temperature, pressure, salt concentration, and pH, with quartz solubility in Si undersaturated seawater increasing drastically at fluid pH conditions above 9 (Steele-MacInnis et al., 2012; Seward et al., 2014). The removed silica was transported away from these alteration sites via the active structural network, where it potentially precipitated as silica-rich minerals in distal (unobserved) areas of the lithotectonic unit, or was released into, and diluted by, the ancient ocean. The replacement of quartz bands by carbonate minerals was aided by the retrograde solubility of carbonate minerals over the temperature range documented at the Beebyn deposit (cf. Seward et al., 2014). Episodic intensification of the fluid flux rate most likely led to an increase in hydraulic fluid pressures, rock fracturing, and a rapid drop in hydrostatic pressures. Subsequent phase separation of the bicarbonate-rich aqueous fluid resulted in the loss of gaseous CO_2 (Eq. 4). Removal of CO_2 drove the reactions shown in Equations 4, 5 and 6 to the right, thus lowering the concentration of free hydrogen ions in the fluid. The resultant increase in the fluid pH led to the precipitation of magnetite and ferroan dolomite (Eq. 7) and promoted the further dissolution of quartz bands.

Eq. 3 $SiO_{2s} \rightarrow SiO_{2aq}$ (dissolution of quartz bands)

Eq. 4 $H_2CO_{3aq} \rightarrow CO_{2g} + H_2O_L$ (phase separation, CO_2 loss, and decrease in carbonic acid)

Eq. 5 $H^+_{aq} + HCO_3^-{}_{aq} \rightarrow H_2CO_{3aq}$ (decrease in free H ions)

Eq. 6 $H^+_{aq} + CO_3^{2-}{}_{aq} \rightarrow HCO_3^-{}_{aq}$ (decrease in free H ions)

Eq. 7 $Fe_2O_{3S} + 1.2Fe^{2+}_{aq} + 0.8Mg^{2+}_{aq} + Ca^{2+}_{aq} + 2CO_3^{2-}_{aq} + 2OH^-_{aq} \rightarrow Fe_3O_{4S} +$ $(0.2Fe,0.8Mg)Ca(CO_3)_{2S} + H_2O_L$ (precipitation of magnetite and ferroan dolomite)

Stage 2: moderate-temperature, magmatic- and seawater-derived fluids The Stage 2 fluid event is represented by ferroan dolomite veins and replacement zones in BIF. Stage 2 alteration zones broadly overlap the spatial distribution of Stage 1 alteration throughout the Beebyn deposit, suggesting that Stage 2 fluids exploited the existing fault network. Stage 2 fluids vary in their homogenization temperatures and salinities, probably as a consequence of the trapping of multiple pulses of Stage 2 fluids through time and varying distances from the main fluid pathways. They include (i) higher-temperature/ higher-salinity fluids (>275 to 327 ºC; 36 to 40 equiv. wt% NaCl), (ii) moderate-temperature/ low- to moderate-salinity fluids (>225 to 260 ºC; 3 to 24 equiv. wt% $CaCl_2$), and (iii) lower-temperature/ low- to moderate-salinity fluids (>125 to 180 ºC; 2 to 24 equiv. wt% $CaCl_2$). All Stage 2 fluids are water-rich, silica-poor, reduced, and alkaline. Chloride is the dominant anion, while the cations include Fe, Ca, Mg, Mn, Na, K, Rb, P, Sr, Cu, Ba, Zn, Pb, W, S, and Co.

The hottest and most saline Stage 2 fluids have Cl/Br and C and O isotopes values that overlap the ranges for magmatic fluids, but with the likely minor involvement of Archean seawater. These fluids record chemical exchange with country rocks, evidenced by (i) the dissolution of halite through interaction with evaporites, (ii) addition of cations from mafic igneous country rocks (Ca, K, Na, Mg, Mn, Sr, Rb, and Ba), and (iii) the presence of accessory sulfide minerals containing Fe, Cu, Pb, Zn, As, Ni, Co, Sb, and Ag. The trapping of these higher-temperature Stage 2 fluids at least 3 km apart in the W8 and W10 prospects suggests that there were multiple pathways for fluid movement through BIF.

The moderate- and lower-temperature Stage 2 brines are the likely products of a cooling hydrothermal system. Their Cl/Br, O and C isotope, Na/Br, and Ca/Ca+Na values suggest that cooling occurred when magmatic-derived fluids were increasingly mixed with Archean seawater and reacted with mafic igneous country rocks in areas distal to central fluid pathways. A coincident decrease in Na/Br and increase in Ca/Ca+Na values in Stage 2 fluids likely resulted from albitization of plagioclase in mafic igneous country rocks. The variable salinities recorded for Stage 2 fluids suggest the existence of a chemical gradient along fluid pathways; from a higher-salinity, magmatic-derived brine that experienced extensive chemical exchange with mafic igneous country rocks, to a lower-salinity fluid compatible with unmodified Archean seawater. These observations are analogous to those described by Gutzmer et al. (2003) for fluid gradients in a passive seafloor alteration regime, where low salinity ancient seawater evolved to more saline fluids through water loss via the hydration of minerals within mafic volcanic host rocks.

Replacement of quartz continued during the Stage 2 fluid event, with primary quartz bands that survived the Stage 1 event replaced by Stage 2 ferroan dolomite (Eq. 3 and Eq. 8).

(Eq. 8) $Ca^{2+}_{aq} + Mg^{2+}_{aq} + 2CO_3^{2-}_{aq} \rightarrow CaMg(CO_3)_{2S}$ (precipitation of dolomite)

Structurally-controlled fluid pathways that transported the hottest Stage 2 fluid had the greatest potential to replace quartz with ferroan dolomite due to the prograde solubility of quartz and retrograde solubility of carbonate minerals in H_2O (Rimstidt, 1997). As the Stage 2 fluid cooled with time and distance from central fluid pathways quartz replacement by ferroan dolomite became less prevalent, marking the transference

to the Stage 3 fluid alteration event.

Stage 3: lower-temperature, seawater-derived (vent) fluids The Stage 3 fluid event resulted in the replacement of Stages 1 and 2 carbonate minerals by magnetite and minor ferroan dolomite, primarily in the W11 and W10 prospects. Faults that channelled earlier fluids continued to be the main control on the distribution of Stage 3 fluids. These fluids were focussed along both margins of the Beebyn North BIF, although the northern margin experienced more extensive fluid flow and consequently shows the thickest alteration zones. Stage 3 alteration terminates short distances away from the central fault network, resulting in a series of 50 m to 1 km-long, magnetite-rich lenses.

Stage 3 aqueous fluids are lower-temperature (>98 to 175 °C), reduced, and alkaline. These low to high-salinity brines fluids are silica-undersaturated and Cl-rich, with cations including Fe, Ca, Mg, Mn, Na, K, Rb, P, Sr, Sc, Cu, Ba, Zn, Pb, W, S, As, Mo, Bi, Cr, and Co. Compared with Stage 1 magnetite, the Stage 3 magnetite contains more W, Cu, Pb, As, and Sr, but less Mg and Mn (Fig. 18). Stage 3 fluids have Cl/Br values that overlap reported ranges for 3.2 Ga vent fluids and seawater (cf. Gutzmer et al., 2003). Based on these evidences, the Stage 3 fluids are compatible with heated Archean seawater that was chemically-modified through interaction with mafic country rocks.

The lower-temperature of Stage 3 aqueous fluids, compared with earlier hypogene fluid alteration events promoted the dissolution of Stage 2 ferroan dolomite owing to the retrograde solubility of carbonate minerals in brines. Ferrous iron was probably more concentrated in Stage 2 fluids due to its hotter temperature and the higher solubility of ferrous iron. Cooling of the fluid during the Stage 3 event most likely led to a decrease in solubility and precipitation of magnetite (Eq. 9). Eventually, as the influx of Stage 3 fluids waned, the dissolution of carbonate minerals raised fluid pH above those levels required for dissolution (Rosenqvist et al., 2012), leading to the minor co-precipitation of Stage 3 ferroan dolomite with magnetite.

Eq. 9 $Fe^{2+}_{aq} \rightarrow Fe_3O_{4S}$ (precipitation of magnetite)

Magnetite-rich veins

Magnetite-rich veins, such as those documented at the Madoonga deposit, have a similar relative timing to the magnetite replacement-style orebodies in that they pre-date regional upright folding in the Weld Range greenstone belt (Table 2). However, both styles of magnetite ore are not present in the same deposit, suggesting different processes operated during their genesis. The Madoonga Stage 2 fluids are likely to have been reduced brines containing Fe, Na, K, Ca, Mg, Si, Cr, K, Mo, P, Sc, Ba, Sr, Ga, Zn, Pb, S, Ti, W, U, and V. Their fluid Cl/Br values overlap reported compositional fields for low-grade metamorphic fluids, geothermal brines, or oil field formation waters. Additionally, their halogen and cation ratios suggest that these fluids dissolved halite through interaction with evaporites and experienced significant addition of Na, K, Ca, and Mg through alteration of feldspars in mafic igneous country rocks. The absence of key fluid data (microthermometry and stable isotope data) for magnetite-rich veins hinders interpretations of their fluid source and a detailed comparison with fluids associated with magnetite replacement-style orebodies. However, an important distinction between both fluid events is the absence of carbonate

minerals associated with the magnetite-rich veins. Consequently, the Madoonga Stage 2 fluids are unlikely to have contained significant amounts of bicarbonate ions or CO_2.

The broad spatial association (but mutual exclusion) between metre-thick magnetite-rich veins and semi-massive pyrite intervals in diamond drillholes intersecting the Madoonga lithotectonic unit (Fig. 2D) suggest that (i) they formed from different pulses of fluids that pre-date regional folding, or (ii) they are products of an evolving iron-rich fluid that transected multiple levels of the stratigraphic sequence and they varied in terms of their local differences in the activity of S in the fluid. These fluids deposited talc as a principle alteration product in BIF, but chlorite in nearby Al-rich, felsic volcanic and mafic country rocks. Narrow fault zones that transect the stratigraphic sequence and are now transposed subparallel to bands are likely the main conduits for the fluids. Whereas, the main controls on iron mobility in the fluid is likely temperature and the redox state, with cooling and oxidation of the reduced fluid responsible for magnetite precipitation. The Madoonga Stage 2 fluids are most compatible with brines that are derived from heated Archean seawater that interacted with mafic and felsic country rocks; these fluids mobilized iron in BIF, leading to its transport by shear zones and concentration as narrow orebodies in BIF at shallower crustal levels.

Specular hematite-rich veins

Specular hematite-quartz veins hosted by shear zones at the Beebyn and Madoonga deposits are folded by the regional upright folding event. Coarse-grained hematite intergrown with euhedral undeformed quartz indicates that the veins crystallized after shearing, most likely during a discrete fluid crystallization episode rather than from multiple mineral replacement events. Representative Madoonga Stage 3 fluids measured from the W15 and W19 prospects are oxidized brines that crystallized specular hematite and quartz over a range of temperatures from 108 to 222 °C. The fluids contained Fe, Ca, Mg, K, Mn, Cu, Sr, Ba, Zn, Pb, S, Ga, Sn, Co, W, and Bi. Cation exchange likely took place with mafic country rocks, with Na depleted in the fluids as a consequence of albitization of country rocks. Fluid Cl/Br values indicate that these fluids dissolved halite through interaction with evaporites and these fluid values overlap the reported ranges for geothermal brines, oil field formation waters, and low-grade metamorphic fluids. However, negative oxygen isotope fluid values (-6.73 to -6.34 ‰) from Stage 3 quartz indicate the likely involvement of meteoric fluids and possibly seawater (Fig. 16), thus discounting a low-grade metamorphic fluid origin.

The differences in the salinity and major cation components of Madoonga Stage 3 fluids recorded between the W15 and W19 prospects are probably the result of different degrees of fluid interaction with mafic country rocks. The lower salinity, NaCl-dominant fluids recorded at the W15 prospect likely better reflect the initial fluid chemistry of ancient meteoric fluids and seawater, whereas the higher salinity, mixed cation content of fluids from the W19 prospect demonstrate more extensive chemical exchange with country rocks. Iron was most likely mobilized within BIF in its reduced state by heated meteoric fluids or seawater and precipitated as a consequence of oxidation and cooling of the fluid (e.g. Eq. 10).

(Eq. 10) $2Fe^{2+}_{aq} + 0.5O^{2-}_{aq} + 2H_2O_L \rightarrow Fe_2O_{3S} + 4H^{+}_{aq}$

Post-ore alteration by seawater and meteoric waters

The post-ore veins cut folded magnetite- and specular hematite-rich orebodies at the Beebyn and Madoonga deposits. Constrained fluid events include the Beebyn Stages 5, 6, and 7 fluids and the Madoonga Stages 4 and 6 events. Beebyn Stage 5 fluids that replaced Stage 2 ferroan carbonate bands with crystalline quartz ± magnetite ± chalcopyrite are lower-temperature (>133 to 196 °C), high-salinity, reduced brines. The fluids are Cl-dominant and contain Si, Ca, Na, Fe, Mg, K, Mn, Cu, Sr, Ba, Zn, Pb, Bi, Sn, S, Co, and W. Their Cl/Br values indicate halite dissolution of evaporites with Na depletion caused by albitization of mafic country rocks. Halogen ratios overlap reported fields for geothermal brines, oil field formation waters, or low-grade metamorphic fluids; whereas O isotopes fluid values are comparable with Archean seawater or meteoric waters.

Beebyn Stage 6 fluids responsible for minor calcite-ferroan dolomite ± magnetite ± pyrite ± chalcopyrite veins are lower-temperature (>115 to 152 °C), moderate-salinity, reduced brines. The fluids contain Fe, Ca, Mg, Mn, Na, K, Sr, Ba, Ge, V, Pb, Zn, S, W, and Co, but are depleted in Si. Carbon and O isotopes for the fluids are comparable to values for Archean seawater or meteoric waters, with local interaction with organic carbon from shales. The Beebyn Stage 7 fluids that formed minor siderite-magnetite veins are similarly lower-temperature (>125 to 180 °C), moderate-salinity, reduced, brines that contain Fe, As, Ba, Ca, Ge, Mg, Mn, Mo, Na, P, Pb, Rb, Sr, Ti, and V. Their fluid source areas are poorly constrained. Madoonga Stage 4 and 6 fluids responsible for minor siderite-quartz and quartz-ferroan dolomite ± pyrite veins, respectively, have C and O isotopes that are compatible with Archean seawater or meteoric waters, with local interaction with organic carbon from shales. In summary, the post-ore fluid events recorded in BIF at the Beebyn and Madoonga deposits display overlapping temperature ranges, with greater differences in their fluid compositions and salinities. They record involvement of Archean seawater or meteoric waters, most likely circulating at shallow crustal levels in a basinal system and interacting with BIF, mafic country rocks, and organic carbon in siliclastic rocks such as shales.

Comparison with other BIF-hosted hypogene iron and base metal VMS systems

Evidence that is considered to be definitive for a hypogene fluid origin for magnetite- and some crystalline hematite-rich orebodies throughout the world includes (i) the spatial and co-temporal association between high-grade iron orebodies and hypogene alteration zones in BIF and neighboring country rocks below the limits of near-surface Cenozoic weathering, and (ii) fluid inclusion and stable isotope data that demonstrate the role of warm to hot, externally-derived basinal or magmatic brines that altered BIF during Proterozoic times (Hagemann et al., 2016).

For example, the Mount Tom Price (Hagemann et al., 1999; Thorne et al., 2004) and Paraburdoo (Thorne et al., 2014) hypogene orebodies in the Hamersley Province demonstrate the involvement of hot (<400 °C) basinal brines with high salinity, Ca, and base metal contents, and low Cl/Br and Na/Br ratios that were focused along normal faults. These fluids interacted with dolomite from the Wittenoom Formation, resulting in a positive shift in $\delta^{13}C$ fluid values towards those for the dolomite, before altering nearby BIF

and forming high-grade magnetite- and hematite-rich ores. Thermodynamic modelling of the proposed desilicification-carbonate replacement process at Mount Tom Price interprets the likely central role of gravity-driven, high-pH (>9), hypersaline brines derived from an evaporitic source that reacted with BIF along an up-temperature fluid-wallrock alteration pathway (Evans et al., 2013). The Thabazimbi iron deposit in South Africa contains near-surface supergene goethite-rich ores that formed during Late Mesozoic-Cenozoic lateritic weathering. Deeper high-grade hematite (martite and microplaty) ores and genetically associated carbonate alteration zones resulted from ancient Ca-Na- and Mg-K-bearing brines interacting with BIF at temperatures of 120 to 160 °C (Gutzmer et al., 2005). Similarly at the Serra Norte deposit in the Carajás mineral province of Brazil, Paleoproterozoic hematite-rich massive and brecciated ores hosted by Archean BIF resulted from reactions with ascending hot (220 to 320 °C) magmatic-derived brines. Later alteration of BIF involved the mixing of brines with meteoric water, followed by interaction with low-salinity meteoric water (Figueiredo e Silva et al., 2013).

The Weld Range hypogene iron deposits show similar hypogene fluid evolution histories described for the major deposit examples summarized above, including the early dominance of hot brines, followed by mixing between brines and seawater or meteoric fluids, and lastly by low-salinity meteoric waters. The fluid transitions generally correspond to hypogene fluids becoming cooler and more oxidized with time, initially producing magnetite-rich orebodies followed by specular hematite or microplaty hematite-rich ore. A key distinction between the Weld Range deposits and documented hypogene deposits in the Hamersley Province is that the latter deposits are a product of basinal brines without contributions from magmatic-derived fluids. In these cases, the source of bicarbonate ions in the hypogene brines was probably dolomite from the Wittenoom Formation.

The Serra Norte deposit in the Carajás mineral province is a closer analogy to the Weld Range deposits in that both areas record the early involvement of hot magmatic-derived fluids. In the case of the Serra Norte deposit, the source of magmatic-hydrothermal fluids was deeply buried granites, with fluids ascending along fault zone and fracture networks that were active during the Paleoproterozoic (Figueiredo e Silva et al., 2013). Rather than the Weld Range magnetite-rich orebodies being the product of deep circulation of magmatic-hydrothermal brines during an orogenic cycle as first proposed by Duuring and Hagemann (2013b), it is likely that they formed in shallow crustal levels with ready access to a combination of magmatic- and seawater-derived fluids. Possible tectonic environments include ancient mid-ocean ridge and back-arc basin settings where subvolcanic felsic intrusions drive hydrothermal convection cells in shallow crustal rocks, contributing energy, fluids, and metals. Replacement of quartz bands by hypogene carbonate in BIF took place below the seafloor, with the removed silica dispersed via vents into seawater.

These geological processes are similar to those responsible for volcanogenic massive sulfide Cu-Zn-Pb deposits. These VMS systems record a range of fluid temperatures (e.g. <100 to 400 °C) and salinities (0 to 30 equiv. wt% NaCl), with the common presence of Na and divalent cations such as Ca^{2+} in the fluid (Bodnar et al., 2014). Oxygen isotope fluid values indicate mixing of seawater with country rocks and more locally with magmatic fluids (e.g. Zengqian et al., 2008; Shanks III, 2014). The overall range in salinities and compositions of the fluids suggest seawater modification through water-rock interaction (e.g. hydrolysis reactions with minerals or interaction with evaporites), phase separation, addition of magmatic fluid, or a combination of these processes (Ridley, 2012; Bodnar et al., 2014). Fluid compositions reflect

the chemistry of the country rocks and the degree of their interaction. Iron is transported in its reduced form and precipitates as sulfide minerals, mostly through a decrease in temperature from about 350 to 200 °C and an increase in the oxidation state of the fluid (e.g. Hannington, 2014). Evidence from Weld Range suggest similar processes for iron transport and precipitation, with the exception that the low concentration of S in the mineralizing fluid resulted in the precipitation of magnetite rather than iron sulfide minerals.

A genetic association between Cu-Zn-Pb VMS and sulfur-poor magnetite end-member systems has been proposed for stratiform magnetite lenses and VMS deposits in the Cambrian to Ordovician Mount Windsor volcanic belt in north Queensland, Australia (Duhig et al., 1992). The magnetite lenses are located along strike and immediately stratigraphically above known VMS deposits. Both ore types are considered to be the result of mixing between a hydrothermal fluid and seawater, and cooling of the product, formed at different stages during the hydrothermal system. Iron-formations of the upper Soldiers Cap Group in the Mt Isa Inlier, Queensland, are considered to be products of mixing between hydrothermal fluids and seawater, with emplacement of voluminous Fe-tholeiite magma into the base of the sedimentary sequence a likely source of hot Fe-rich fluids (Hatton and Davidson, 2004). Co-spatial occurrences of massive sulfide and magnetite-rich orebodies exist at the Madoonga deposit in the Weld Range district, the Koolyanobbing BIF-hosted iron district in the Southern Cross Domain of the Yilgarn Craton (Angerer and Hagemann, 2010; Angerer et al., 2012), and at the Golden Groves VMS deposit in the Eastern Goldfields Superterrane (Sharpe and Gemmell, 2001; Sharpe and Gemmell, 2002). Other documented examples of VMS deposits containing significant magnetite-rich zones include the Corbet, Orchan, Anderson Lake, Balcooma, and Boksputs deposits in eastern Australia (Large, 1977; Knuckey and Watkins, 1982; Walford and Franklin, 1982; Geringer et al., 1987; Huston, 1989). The demonstrated spatial and genetic coincidence between VMS and magnetite-rich mineral systems has implications for predicting their mutual occurrence within a district and interpreting syn-volcanic alteration patterns as vectors for their detection.

Conclusions

The BIF-hosted iron ore deposits of the Yilgarn Craton contain near-surface, supergene goethite-hematite orebodies that overlie and partly modify deeper occurrences of hypogene magnetite and specular hematite ores. The chemical-physical properties and source of the mineralizing fluids responsible for these magnetite- and specular hematite-rich orebodies are poorly constrained due to the lack of fluid inclusion studies for these deposits. This study is the first to address this problem by undertaking a combined fluid inclusion and stable isotope study of the Beebyn and Madoonga deposits, located in the Weld Range greenstone belt in the Murchison Domain of the Yilgarn Craton.

Magnetite-rich orebodies at the Beebyn deposit are the product of secondary enrichment of iron in the BIF through the replacement of primary quartz bands by hypogene carbonate minerals, followed by carbonate replacement by hypogene magnetite. In contrast, magnetite-talc veins are the dominant style of magnetite-rich ore body present at the Madoonga deposit. At both deposits, specular hematite-quartz veins hosted by fault zones cut the primary quartz-magnetite BIF units and both types of magnetite-rich orebodies.

Magnetite replacement-style orebodies at the Beebyn deposit are the product of a multistage fluid event (Beebyn Stages 1 to 3) affecting BIF over an aerial extent of at least of 8 km. The timing of this event post-dates the diagenesis of the BIF and emplacement of c. 2752 to 2740 Ma mafic-ultramafic country rocks, but pre-dates the regional upright folding and steep tilting of the Weld Range lithotectonic unit. Beebyn fluid Stages 1, 2 and 3 alteration took place as a result of a multi-kilometer scale, (magmatic-) hydrothermal fluid system centred beneath BIF and underlying mafic igneous rocks in shallow areas of the crust that were intermittently accessible to ancient modified seawater. The Stage 1 event began with a hot, dominantly magmatic-derived fluid with only minor contributions from ancient seawater. The fluids travelled along steeply dipping faults to shallower areas where they experienced chemical exchange with underlying mafic country rocks and BIF, and eventually underwent phase separation due to fracturing and a rapid lowering of confining pressures. The exsolution and removal of CO_2 from the aqueous fluids most likely triggered an increase in the alkalinity of the fluid. Under these alkaline and hot conditions, quartz bands in BIF were readily replaced by carbonate minerals. During the Stage 2 event, a decrease in the supply of hot magmatic-derived fluids led to a higher proportion of circulating heated and modified ancient seawater transported through BIF along the same fault pathways through mafic country rocks. These reduced and alkaline Stage 2 brines further promoted the replacement of primary quartz bands by hypogene carbonate minerals. As the hydrothermal system waned during the Stage 3 event, the Beebyn BIF experienced alteration of carbonates along and proximal to the central fluid pathways, resulting in magnetite replacement-style lenses that are surrounded by broader zones of relict carbonate alteration minerals.

Magnetite-talc veins at the Madoonga deposit are likely the product of a genetically distinct mineralization event. Fluid halogen ratios are compatible with a source including low-grade metamorphic fluids, geothermal brines, or oil field formation waters. However, their common close spatial association with semi-massive sulfides suggest that they are more likely brines that were derived from heated Archean seawater. These fluids interacted with mafic and felsic country rocks, mobilizing iron from BIF and concentrating it in narrow fault zones at shallow crustal levels.

Specular hematite-quartz veins hosted by shear zones at the Beebyn and Madoonga deposits are folded by the regional upright folding event. Iron was most likely mobilized within BIF in its reduced state by heated meteoric fluids or seawater and precipitated as a consequence of oxidation and cooling of the fluid. Whereas, post-ore fluid events recorded in BIF at the Beebyn and Madoonga deposits record the involvement of Archean seawater or meteoric waters, most likely circulating at shallow crustal levels in a basinal system and interacting with BIF, mafic country rocks, and organic carbon in siliclastic rocks such as shales.

The hypogene iron deposits in the Weld Range district display similar hypogene fluid evolution histories compared with the major iron deposits of the Hamersley Province and Carajás mineral province. The Weld Range deposits show greatest similarity to the Serra Norte deposit in the Carajás mineral province in that they both record the early involvement of hot magmatic-derived fluids that evolve with time to mixing between brines or meteoric fluids, and lastly by meteoric waters. However, the magnetite replacement-style and magnetite-rich veins in the Weld Range district differ in that the magmatic fluids were most likely derived from a shallower crustal level compared with the fluids responsible for iron deposits in the Carajás mineral province. Instead, the Weld Range magnetite orebodies display similar

structural controls, ore body geometries, and fluid chemical and physical properties to replacement-style, volcanic-hosted massive sulfide orebodies; suggesting at least a spatial, and possibly a genetic, association between these mineral systems. The identification of one style of mineralization may therefore be an indicator for the presence of the other within a district.

Acknowledgements

This study was funded by the Geological Survey of Western Australia's Exploration Incentive Scheme (a Royalties for Regions initiative). Sinosteel Midwest Corporation funded initial field work in the Weld Range district and provided access to drill core (2009 to 2010). Stephane Roudaut assisted with the collection of microthermometry data while Orestes Santos provided advice during SEM examination of samples for accessory mineral identification. The authors acknowledge the facilities, and the scientific and technical assistance of the Australian Microscopy and Microanalysis Research Facility at the Centre for Microscopy, Characterisation and Analysis, The University of Western Australia, a facility funded by the University, State and Commonwealth Governments. Malcolm Roberts provided assistance with the collection of the quantitative element maps using the JEOL 8530F. Thomas Becker is thanked for his advice with the laser Raman analyses at the CMCA. John Cliff and Sten Littmann are thanked for help with acquiring the O isotope data using the CAMECA 1280 at the CMCA. Noreen Evans and Brad McDonald provided advice with the set up and analysis of iron oxide minerals at the AGOS-GeoHistory LA-ICP-MS Facility, Curtin University. John Valley and Michael Spicuzza (Department of Geoscience at the University of Wisconsin-Madison) are thanked for their advice and provision of O isotope data for magnetite separates by laser fluorination. Tim Ivanic, Josh Guilliamse, and Lee Hassan are thanked for discussions concerning the interpretation of published geochronological data for the Weld Range greenstone belt. Figures were improved by Adam Symonds. Paul Duuring publishes with permission from the Director of the Geological Survey of Western Australia. Matthew Steele-MacInnis, David Burrows, Elizabeth Turner, and Larry Meinert are thanked for their reviews and handling of the manuscript.

References

Angerer, T., Duuring, P., Hagemann, S.G., Thorne, W., and McCuaig, T.C., 2015, A mineral system approach to iron ore in Archaean and Palaeoproterozoic BIF of Western Australia, in GRT Jenkin, PAJ Lusty, I McDonald, MP Smith, AJ Boyce and JJ Wilkinson ed., Ore Deposits in an Evolving Earth, Geological Society of London, p. 81–115.

Angerer, T. and Hagemann, S.G., 2010, The BIF-hosted high-grade iron ore deposits in the Archean Koolyanobbing greenstone belt, Western Australia: structural control on synorogenic- and weathering-related magnetite-, hematite-, and goethite-rich iron ore: Economic Geology, v. 105, p. 917–945.

Angerer, T., Hagemann, S.G., and Danyushevsky, L., 2013, High-grade iron ore at Windarling, Yilgarn craton: a product of syn-orogenic deformation, hydrothermal alteration, and supergene modification in an Archean BIF–basalt lithostratigraphy: Mineralium Deposita, v. 48, p. 697–728.

Angerer, T., Hagemann, S.G., and Danyushevsky, L.V., 2012, Geochemical evolution of the banded iron formation-hosted high-grade iron ore system in the Koolyanobbing Greenstone Belt, Western Australia: Economic Geology, v. 107, p. 599–644.

Audetat, A., Gunther, D., and Heinrich, C.A., 2000a, Magmatic-hydrothermal evolution in a fractionating granite: a microchemical study of the sn-w-f-mineralized mole granite (Australia): Geochimica et Cosmochimica Acta, v. 64, p. 3373–3393.

Audetat, A., Gunther, D., and Heinrich, C.A., 2000b, Causes for large-scale metal zonation around mineralized plutons: fluid inclusion LA-ICP-MS evidence from the Mole Granite, Australia: Economic Geology, v. 95, p. 1563–1581.

Baker, T., Ebert, S., Rombach, C., and Ryan, C.G., 2006, Chemical compositions of fluid inclusions in intrusion-related gold systems, Alaska and Yukon, using PIXE microanalysis: Economic Geology, v. 101, p. 311–327.

Banks, D.A., Boyce, A.J., and Samson, I.M., 2002, Constraints on the origins of fluids forming Irish Zn-Pb-Ba deposits: evidence from the composition of fluid inclusions: Economic Geology, v. 97, p. 471–480.

Banks, D.A., Da Vies, G.R., Yardley, B.W.D., Mccaig, A.M., and Grant, N.T., 1991, The chemistry of brines from an Alpine thrust system in the Central Pyrenees: An application of fluid inclusion analysis to the study of fluid behaviour in orogenesis: Geochimica et Cosmochimica Acta, v. 55, p. 1021–1030.

Banks, D.A., Giuliani, G., Yardley, B.W.D., and Cheilletz, A., 2000a, Emerald mineralisation in Colombia: fluid chemistry and the role of brine mixing: Mineralium Deposita, v. 35, p. 699–713.

Banks, D.A., Green, R., Cliff, R.A., and Yardley, B.W.D., 2000b, Chlorine isotopes in fluid inclusions: determination of the origins of salinity in magmatic fluids: Geochimica et Cosmochimica Acta, v. 64, p. 1785–1789.

Barley, M.E., Pickard, A.L., Hagemann, S.G., and Folkert, S.L., 1999, Hydrothermal origin for the 2 billion year old Mount Tom Price giant iron ore deposit, Hamersley Province, Western Australia: Mineralium Deposita, v. 34, p. 784–789.

Bekker, A., Planavsky, N.J., Krapež, B., Rasmussen, B., Hofmann, A., Slack, J.F., Rouxel, O.J., and Konhauser, K.O., 2014, Iron formations: their origins and implications for ancient seawater chemistry, in KK Turekian ed., Treatise on Geochemistry (Second Edition), Oxford, UK, Elsevier, p. 561–628.

Biagioni, C. and Pasero, M., 2014, The systematics of the spinel-type minerals: an overview: American Mineralogist, v. 99, p. 1254–1264.

Bodnar, R.J., Lecumberri-Sanchez, P., Moncada, D., and Steele-MacInnis, M., 2014, Fluid inclusions in hydrothermal ore deposits, in KK Turekian ed., Treatise on Geochemistry (2nd Edition), Oxford, UK, Elsevier, p. 119–142.

Bodnar, R.J. and Vityk, M.O., 1994, Interpretation of microthermometric data for NaCl-H_2O fluid inclusions, in B De Vivo and ML Frezzotti ed., Fluid inclusions in minerals: methods and applications, Blacksburg, Virginia, United States of America, Virginia Polytechnic Institute and State University, p. 117–131.

Bohlke, J.K. and Irwin, J.J., 1992, Laser microprobe analyses of noble gas isotopes and halogens in fluid inclusions: analyses of microstandards and synthetic inclusions in quartz: Geochimica et Cosmochimica Acta, v. 56, p. 187–201.

Bottrell, S.H., Yardley, B., and Buckley, F., 1988, A modified crush-leach method for the analysis of fluid inclusion electrolytes: Bulletin de Minéralogie, v. 111, p. 279–290.

Boutroy, E., Dare, S.A.S., Beaudoin, G., Barnes, S.J., and Lightfoot, P.C., 2014, Magnetite composition in Ni-Cu-PGE deposits worldwide: application to mineral exploration: Journal of Geochemical Exploration, v. 145, p. 64–81.

Bowers, T.S., Campbell, A.C., Measures, C.I., Spivack, A.J., Khadem, M., and Edmond, J.M., 1988, Chemical controls on the composition of vent fluids at 13°-11°N and 21°N, East Pacific Rise: Journal of Geophysical Research: Solid Earth, v. 93, p. 4522–4536.

Buddington, A.F. and Lindsley, D.H., 1964, Iron-titanium oxide minerals and synthetic equivalents: Journal of Petrology, v. 5, p. 310–357.

Cabral, A.R. and Rosière, C.A., 2013, The chemical composition of specular hematite from Tilkerode, Harz, Germany: implications for the genesis of hydrothermal hematite and comparison with the Quadrilátero Ferrífero of Minas Gerais, Brazil: Mineralium Deposita, v. 48, p. 907–924.

Campbell, A.C., Palmer, M.R., Klinkhammer, G.P., Bowers, T.S., Edmond, J.M., Lawrence, J.R., Casey, J.F., Thompson, G., Humphris, S., Rona, P., and Karson, J.A., 1988, Chemistry of hot springs on the Mid-Atlantic Ridge: Nature, v. 335, p. 514–519.

Campbell, A.R., Banks, D.A., Phillips, R.S., and Yardley, B.W.D., 1995, Geochemistry of Th-U-REE mineralizing magmatic fluids, Capitan Mountains, New Mexico: Economic Geology, v. 90, p. 1271–1287.

Carew, M.J., Mark, G., Oliver, N.H.S., and Pearson, N., 2006, Trace element geochemistry of magnetite and pyrite in Fe oxide (±Cu–Au) mineralized systems: Insights into the geochemistry of ore-forming fluids: Geochimica et Cosmochimica Acta, v. 70, p. A83.

Carpenter, A.B., Trout, M.L., and Pickett, E.E., 1974, Preliminary report on origin and chemical evolution of lead-rich and zinc-rich oil field brines in Central Mississippi: Economic Geology, v. 69, p. 1191–1206.

Clark, A.M., 1993, Hey's mineral index, mineral species, varieties and synonyms (3rd edition): London, United Kingdom, Chapman and Hall,

Cole, D.R., Horita, J., Polyakov, V.B., Valley, J.W., Spicuzza, M.J., and Coffey, D.W., 2004, An experimental

and theoretical determination of oxygen isotope fractionation in the system magnetite–H_2O from 300 to 800ºC: Geochimica et Cosmochimica Acta, v. 68, p. 3569–3585.
Connolly, C.A., Walter, L.M., Baadsgaard, H., and Longstaffe, F.J., 1990, Origin and evolution of formation waters, Alberta Basin, Western Canada sedimentary Basin. I. Chemistry: Applied Geochemistry, v. 5, p. 375–395.
Cornell, R.M. and Schwertmann, U., 2003, The iron oxides: structure, properties, reactions, occurrences, and uses (2nd edition): Weinheim, Germany, Wiley-VCH,
Dare, S.A.S., Barnes, S.J., and Beaudoin, G., 2012, Variation in trace element content of magnetite crystallized from a fractionating sulfide liquid, Sudbury, Canada: Implications for provenance discrimination: Geochimica et Cosmochimica Acta, v. 88, p. 27–50.
Dare, S.A.S., Barnes, S.J., Beaudoin, G., Méric, J., Boutroy, E., and Potvin-Doucet, C., 2014, Trace elements in magnetite as petrogenetic indicators: Mineralium Deposita, v. 49, p. 785–796.
De Ronde, C.E.J., Channer, D.M., Faure, K., Bray, C.J., and Spooner, E.T.C., 1997, Fluid chemistry of Archean seafloor hydrothermal vents: Implications for the composition of circa 3.2 Ga seawater: Geochimica et Cosmochimica Acta, v. 61, p. 4025–4042.
Duhig, N.C., Stolz, J., Davidson, G.J., and Large, R.R., 1992, Cambrian microbial and silica gel textures in silica iron exhalites from the Mount Windsor volcanic belt, Australia; their petrography, chemistry, and origin: Economic Geology, v. 87, p. 764–784.
Dupuis, C. and Beaudoin, G., 2011, Discriminant diagrams for iron oxide trace element fingerprinting of mineral deposit types: Mineralium Deposita, v. 46, p. 319–335.
Duuring, P. and Hagemann, S.G., 2013a, Genesis of superimposed hypogene and supergene Fe ore bodies in BIF at the Madoonga deposit, Yilgarn Craton, Western Australia: Mineralium Deposita, v. 48, p. 371–395.
Duuring, P. and Hagemann, S.G., 2013b, Leaching of silica bands and concentration of magnetite in Archean BIF by hypogene fluids: Beebyn Fe ore deposit, Yilgarn Craton, Western Australia: Mineralium Deposita, v. 48, p. 341–370.
Duuring, P., Hagemann, S.G., Novikova, J., Cudahy, T., and Laukamp, C., 2012, Targeting iron ore in banded iron formations using ASTER data: Weld Range greenstone belt, Yilgarn Craton, Western Australia: Economic Geology, v. 107, p. 585–597.
Duuring, P. and Laukamp, C., 2016, Mapping iron ore alteration patterns in banded iron-formation using hyperspectral data: Beebyn deposit, Yilgarn Craton, Western Australia: Geological Survey of Western Australia, Record 2016/16, 18p.
Evans, K.A., McCuaig, T.C., Leach, D., Angerer, T., and Hagemann, S.G., 2013, Banded iron formation to iron ore: A record of the evolution of Earth environments?: Geology, v. 41, p. 99–102.
Figueiredo e Silva, R., Lobato, L.M., Hagemann, S., and Danyushevsky, L., 2009, Laser-ablation ICP-MS analyses on oxides of hypogene iron ore from the giant Serra Norte jaspilite-hosted iron ore deposits, Carajás Mineral Province, Brazil (ext. abs.) Townsville, Australia, August 2009; Extended Abstracts, p. 570-572.
Figueiredo e Silva, R.C., Hagemann, S., Lobato, L.M., Rosière, C.A., Banks, D.A., Davidson, G.J., Vennemann, T., and Hergt, J., 2013, Hydrothermal fluid processes and evolution of the giant Serra Norte jaspilite-hosted iron ore deposits, Carajás Mineral Province, Brazil: Economic Geology, v. 108, p. 739–779.
Fleet, M.E., 1981, The structure of magnetite: Acta Crystallographica Section B, v. 37, p. 917–920.
Frost, B.R. and Lindsley, D.H., 1991, Occurrence of iron-titanium oxides in igneous rocks: Reviews in Mineralogy and Geochemistry, v. 25, p. 433–468.
Geringer, G.J., Pretorius, J.J., and Cilliers, F.H., 1987, Strata-bound copper–iron sulfide mineralization in a Proterozoic front arc setting at Boksputs, Northwest Cape, South Africa — a possible Besshi-type deposit: Mineralium Deposita, v. 22, p. 81–89.
Ghiorso, M.S. and Sack, O., 1991, Fe–Ti oxide geothermometry: thermodynamic formulation and the estimation of intensive variables in silicic magmas: Contributions to Mineralogy and Petrology, v. 108, p. 485–510.
Goldschmidt, V.M., 1954, Geochemistry: Oxford, UK, Clarendon Press,
Goldstein, R.H. and Reynolds, T.J., 1994, Systematics of fluid inclusions in diagenetic minerals: Society for Sedimentary Geology, Short Course 31, 199p.
Gole, M.J., 1980, Mineralogy and petrology of very-low-metamorphic grade Archaean banded iron-formations, Weld Range, Western Australia: American Mineralogist, v. 65, p. 8–25.
Golyshev, S.I., Padalko, N.L., and Pechenkin, S.A., 1981, Fractionation of stable isotopes of carbon and oxygen in carbonate systems: Geokhmiya, v. 10, p. 1427–1441.
Guilliamse, J., 2014, Assessing the potential for volcanic-associated massive sulfide mineralization at Weld Range, using Golden Grove for comparison: Geological Survey of Western Australia, Report 141, 61p.

Gutzmer, J., Banks, D.A., Lüders, V., Hoefs, J., Beukes, N.J., and von Bezing, K.L., 2003, Ancient sub-seafloor alteration of basaltic andesites of the Ongeluk Formation, South Africa: implications for the chemistry of Paleoproterozoic seawater: Chemical Geology, v. 201, p. 37–53.

Gutzmer, J., Beukes, N.J., de Kock, M.O., and Netshiozwi, S.T., 2005, Origin of high-grade iron ores at the Thabazimbi deposit, South Africa (ext. abs.): AusIMM Iron Ore Conference 2005, Fremantle, Western Australia, 19 September 2005-21 September 2005; Extended Abstracts, p. 57-65.

Hagemann, S.G., Angerer, T., Duuring, P., Rosière, C.A., Figueiredo e Silva, R.C., Lobato, L., Hensler, A.S., and Walde, D.H.G., 2016, BIF-hosted iron mineral system: a review: Ore Geology Reviews, v. 76, p. 317–359.

Hagemann, S.G., Barley, M.E., Folkert, S.L., Yardley, B.W.D., and Banks, D.A., 1999, A hydrothermal origin for the giant BIF-hosted Tom Price iron ore deposit (ext. abs.): Proceedings of the 5th Biennial SGA Meeting and the 10th Quadrennial IAGOD, Extended Abstracts, p. 41-44.

Hagemann, S.G., Rosière, C.A., Gutzmer, J., and Beukes, N.J., 2008, Glossary of terms, in SG Hagemann, CA Rosière, J Gutzmer and NJ Beukes ed., Banded iron formation-related high-grade iron ore, Society of Economic Geologists, p. 411–414.

Haggerty, S.E., 1991, Oxide mineralogy of the upper mantle: Reviews in Mineralogy and Geochemistry, v. 25, p. 355–416.

Hannington, M.D., 2014, Volcanogenic massive sulfide deposits, in KK Turekian ed., Treatise on Geochemistry (2nd Edition), Oxford, UK, Elsevier, p. 463–488.

Hatton, O.J. and Davidson, G.J., 2004, Soldiers Cap Group iron–formations, Mt Isa Inlier, Australia, as windows into the hydrothermal evolution of a base–metal–bearing Proterozoic rift basin: Australian Journal of Earth Sciences, v. 51, p. 85–108.

Hensler, A.S., Hagemann, S.G., Rosière, C.A., Angerer, T., and Gilbert, S., 2015, Hydrothermal and metamorphic fluid–rock interaction associated with hypogene 'hard' iron ore mineralisation in the Quadriláítero Ferrífero, Brazil: implications from in-situ laser ablation ICP-MS iron oxide chemistry: Ore Geology Reviews, v. 69, p. 325–351.

Hoefs, J., 2009, Stable isotope geochemistry: Berlin, Heidelberg (Germany), Springer-Verlag,

Horita, J., 2014, Oxygen and carbon isotope fractionation in the system dolomite–water–CO_2 to elevated temperatures: Geochimica et Cosmochimica Acta, v. 129, p. 111–124.

Huberty, J.M., Konishi, H., Heck, P.R., Fournelle, J.H., Valley, J.W., and Xu, H.F., 2012, Silician magnetite from the Dales Gorge member of the Brockman iron formation, Hamersley Group, Western Australia: American Mineralogist, v. 97, p. 26–37.

Huston, D.L., 1989, Aspects of the structure and stratigraphy of the Balcooma volcanogenic massive sulfide deposit, northern Queensland: Unpublished PhD thesis, Hobart, Tasmania, University of Tasmania

Ivanic, TJ 2009, Madoonga, WA Sheet 2444: Geological Survey of Western Australia, 1:100 000 Geological Series.

James, R.H., Elderfield, H., and Palmer, M.R., 1995, The chemistry of hydrothermal fluids from the Broken Spur site, 29-degrees N mid-Atlantic ridge: Geochimica et Cosmochimica Acta, v. 59, p. 651–659.

James, R.H., Green, D.R.H., Stock, M.J., Alker, B.J., Banerjee, N.R., Cole, C., German, C.R., Huvenne, V.A.I., Powell, A.M., and Connelly, D.P., 2014, Composition of hydrothermal fluids and mineralogy of associated chimney material on the East Scotia Ridge back-arc spreading centre: Geochimica et Cosmochimica Acta, v. 139, p. 47–71.

Johnson, L.H., Burgess, R., Turner, G., and Harris, J.W., 2000, Noble gas and halogen geochemistry of mantle fluids: comparison of African and Canadian diamonds: Geochimica et Cosmochimica Acta, v. 64, p. 717–732.

Kasai, K., Sakagawa, Y., Miyazaki, S., Sasaki, M., and Uchida, T., 1996, Supersaline brine obtained from Quaternary Kakkonda Granite by the NEDO's deep geothermal well WD-1a in the Kakkonda geothermal field, Japan, in DW McClain ed., Geothermal Development in the Pacific Rim, Davis, California, USA, Geothermal Resources Council, p. 623–629.

Kendrick, M.A., Burgess, R., Pattrick, R.A.D., and Turner, G., 2001, Fluid inclusion noble gas and halogen evidence on the origin of Cu-porphyry mineralising fluids: Geochimica et Cosmochimica Acta, v. 65, p. 2651–2668.

Kesler, S.E., Appold, M.S., Martini, A.M., Walter, L.M., Huston, T.J., and Kyle, J.R., 1995, Na–Cl–Br systematics of mineralizing brines in Mississippi valley-type deposits: Geology, v. 23, p. 641–644.

Kharaka, Y.K., Maest, A.S., Carothers, W.W., Law, L.M., Lamothe, P.J., and Fries, T.L., 1987, Geochemistry of metal-rich brines from central Mississippi Salt Dome basin, U.S.A.: Applied Geochemistry, v. 2, p. 543–561.

Knuckey, M.J. and Watkins, J.J., 1982, The geology of the Corbet massive sulphide deposit, Noranda district, Quebec, Canada, in CD Hutchinson, CD Spence and JM Franklin ed., Precambrian sulphide

deposits, Geological Association of Canada, p. 297–317.
Land, L.S., Macpherson, G.L., and Mack, L.E., 1988, Geochemistry of saline formation waters, Miocene, offshore Louisiana: Gulf Coast Association of Geologists Transactions, v. 38, p. 503–511.
Large, R.R., 1977, Chemical evolution and zonation of massive sulfide deposits in volcanic terrains: Economic Geology, v. 72, p. 549–572.
Lascelles, D.F., 2006, The Mount Gibson banded iron formation-hosted magnetite deposit: two distinct processes for the origin of high-grade iron ore: Economic Geology, v. 101, p. 651–666.
Lecumberri-Sanchez, P., Steele-MacInnis, M., and Bodnar, R.J., 2012, A numerical model to estimate trapping conditions of fluid inclusions that homogenize by halite disappearance: Geochimica et Cosmochimica Acta, v. 92, p. 14–22.
Lindsley, D.H., 1976, The crystal chemistry and structure of oxide minerals as exemplified by the Fe–Ti oxides, in D Rumble III ed., Oxide Minerals, Washington, D.C., Mineralogical Society of America, p. L1–L60.
Lüders, V., Reutel, C., Hoth, P., Banks, D.A., Mingram, B., and Pettke, T., 2005, Fluid and gas migration in the North German Basin: fluid inclusion and stable isotope constraints: International Journal of Earth Sciences, v. 94, p. 990–1009.
Makvandi, S., Ghasemzadeh-Barvarz, M., Beaudoin, G., Grunsky, E.C., McClenaghan, M.B., and Duchesne, C., 2016, Principal component analysis of magnetite composition from volcanogenic massive sulfide deposits: case studies from the Izok Lake (Nunavut, Canada) and Halfmile Lake (New Brunswick, Canada) deposits: Ore Geology Reviews, v. 72, Part 1, p. 60–85.
Marie, J.S., Kesler, S.E., and Allen, C.R., 2001, Origin of iron-rich Mississippi Valley-type deposits: Geology, v. 29, p. 59–62.
Maskell, A., Duuring, P., and Hagemann, S.G., 2014, Hydrothermal alteration events controlling magnetite-rich iron ore at the Matthew Ridge prospect, Jack Hills greenstone belt, Yilgarn Craton: Australian Journal of Earth Sciences, v. 61, p. 187–212.
McLennan, S.M., 1989, Rare earth elements in sedimentary rocks; influence of provenance and sedimentary processes: Reviews in Mineralogy and Geochemistry, v. 21, p. 169–200.
Milani, L., Bolhar, R., Cawthorn, R.G., and Frei, D., 2016, In situ LA-ICP-MS and EPMA trace element characterization of Fe-Ti oxides from the phoscorite-carbonatite association at Phalaborwa, South Africa: Mineralium Deposita, p. 1–22.
Mollo, S., Putirka, K., Iezzi, G., and Scarlato, P., 2012, The control of cooling rate on titanomagnetite composition: implications for a geospeedometry model applicable to alkaline rocks from Mt. Etna volcano: Contributions to Mineralogy and Petrology, v. 165, p. 457–475.
Morris, R.C., 1980, A textural and mineralogical study of the relationship of iron ore to banded iron-formation in the Hamersley Iron Province of Western Australia: Economic Geology, v. 75, p. 184–209.
Morris, R.C., 1985, Genesis of iron ore in banded iron-formation by supergene and supergene-metamorphic processes - a conceptual model, in KH Wolf ed., Handbook of strata-bound and stratiform ore deposits, vol. 13, Amsterdam, The Netherlands, Elsevier, p. 73–235.
Morris, R.C. and Kneeshaw, M., 2011, Genesis modelling for the Hamersley BIF-hosted iron ores of Western Australia: a critical review: Australian Journal of Earth Sciences, v. 58, p. 417–451.
Munz, I.A., Yardley, B.W.D., Banks, D.A., and Wayne, D., 1995, Deep penetration of sedimentary fluids in basement rocks from southern Norway: Evidence from hydrocarbon and brine inclusions in quartz veins: Geochimica et Cosmochimica Acta, v. 59, p. 239–254.
Nadoll, P., 2011, Geochemistry of magnetite from hydrothermal ore deposits and host rocks — case studies from the Proterozoic Belt Supergroup, Cu–Mo–porphyry + skarn and Climax-Mo deposits in the western United States: Unpublished PhD thesis, Auckland, New Zealand, University of Auckland
Nadoll, P., Angerer, T., Mauk, J.L., French, D., and Walshe, J., 2014, The chemistry of hydrothermal magnetite: A review: Ore Geology Reviews, v. 61, p. 1–32.
Neuendorf, K.K.E., Mehl Jr, J.P., and Jackson, J.A., 2005, Glossary of Geology (5th edition): American Geological Institute,
Oakes, C.S., Bodnar, R.J., and Simonson, J.M., 1990, The system $NaCl–CaCl_2–H_2O$: I. The ice liquidus at 1 atm total pressure: Geochimica et Cosmochimica Acta, v. 54, p. 603–610.
Ohmoto, H. and Rye, R.O., 1979, Isotopes of sulfur and carbon, in HL Barnes ed., Geochemistry of Hydrothermal Ore Deposits, 2nd Edition, New York, USA, John Wiley and Sons, p. 509–567.
Pope, E.C., Bird, D.K., and Rosing, M.T., 2012, Isotope composition and volume of Earth's early oceans: Proceedings of the National Academy of Sciences of the United States of America, v. 109, p. 4371–4376.
Potter, R.W., 1977, Pressure corrections for fluid-inclusion homogenization temperatures based on volumetric properties of system $NaCl–H_2O$: Journal of Research of the US Geological Survey, v. 5, p. 603–607.

Powell, C.M.c.A., Oliver, N.H.S., Li, Z.X., Martin, D.M.c.B., and Ronaszeki, J., 1999, Synorogenic hydrothermal origin for giant Hamersley iron oxide ore bodies: Geology, v. 27, p. 175–178.

Prokoph, A., Shields, G.A., and Veizer, J., 2008, Compilation and time-series analysis of a marine carbonate $\delta^{18}O$, $\delta^{13}C$, $^{87}Sr/^{86}Sr$ and $\delta^{34}S$ database through Earth history: Earth-Science Reviews, v. 87, p. 113–133.

Ramboz, C., Pichavant, M., and Weisbrod, A., 1982, Fluid immiscibility in natural processes: Use and isuse of fluid inclusion data: II. Interpretation of fluid inclusion data in terms of immiscibility: Chemical Geology, v. 37, p. 29–48.

Ridley, W.I., 2012, Geochemical characteristics in volcanogenic massive sulfide occurrence model, in WCP Shanks III and R Thurston ed., Volcanogenic Massive Sulfide Occurrence Model, Reston, Virginia, USA, U.S. Geological Survey, p. 207–225.

Rimstidt, J., 1997, Gangue mineral transport and deposition, in HL Barnes ed., Geochemistry of hydrothermal ore deposits, 3rd ed.: New York, John Wiley, p. 487–516.

Roedder, E., 1984, Fluid inclusions (Volume 12): Virginia, US, Mineralogical Society of America,

Rosenqvist, J., Kilpatrick, A.D., and Yardley, B.W.D., 2012, Solubility of carbon dioxide in aqueous fluids and mineral suspensions at 294 K and subcritical pressures: Applied Geochemistry, v. 27, p. 1610–1614.

Seward, T.M., Williams-Jones, A.E., and Migdisov, A.A., 2014, The chemistry of metal transport and deposition by ore-forming hydrothermal fluids, in KK Turekian ed., Treatise on Geochemistry (2nd Edition), Oxford, UK, Elsevier, p. 29–57.

Shanks III, W.C.P., 2014, Stable isotope geochemistry of mineral deposits, in KK Turekian ed., Treatise on Geochemistry (2nd Edition), Oxford, UK, Elsevier, p. 59–85.

Sharp, Z., 2006, Principles of stable isotope geochemistry: Upper Saddle River, New Jersey, US, Pearson Prentice Hall,

Sharp, Z.D. and Kirschner, D.L., 1994, Quartz-calcite oxygen isotope thermometry: A calibration based on natural isotopic variations: Geochimica et Cosmochimica Acta, v. 58, p. 4491–4501.

Sharpe, R., 1999, The Archean Cu–Zn magnetite-rich Gossan Hill VHMS deposit, Western Australia: Evidence of a structurally-focussed, exhalative and sub-seafloor replacement mineralising system: Unpublished PhD thesis, Hobart, Tasmania, University of Tasmania

Sharpe, R. and Gemmell, J.B., 2001, Alteration characteristics of the Archean Golden Grove Formation at the Gossan Hill deposit, Western Australia: Induration as a focusing mechanism for mineralizing hydrothermal fluids: Economic Geology, v. 96, p. 1239–1262.

Sharpe, R. and Gemmell, J.B., 2002, The Archean Cu–Zn magnetite-rich Gossan Hill volcanic-hosted massive sulfide deposit, Western Australia: genesis of a multistage hydrothermal system: Economic Geology, v. 97, p. 517–539.

Shepherd, T.J., Rankin, A.H., and Alderton, D.H.M., 1985, A practical guide to fluid inclusion studies: Glasgow, United Kingdom, Blackie and Son,

Singoyi, B., Danyushevsky, L., Davidson, G.J., Large, R., and Zaw, K., 2006, Determination of trace elements in magnetites from hydrothermal deposits using the LA-ICP-MS technique (ext. abs.): SEG 2006 Conference, Keystone, USA, 2 October 2006-5 October 2006; Extended Abstracts, p. 367-368.

Smalley, P.C. and Warren, E.A., 1994, North Sea formation waters: implications for diagenesis and production chemistry: Marine and Petroleum Geology, v. 11, p. 2–4.

Smith, M., Banks, D.A., Yardley, B.W.D., and Boyce, A.J., 1996, Fluid inclusion and stable isotope constraints on the genesis of the Cligga Head Sn-W deposit, S.W. England: European Journal of Mineralogy, v. 8, p. 961–974.

Spaggiari, C.V., 2006, Interpreted bedrock geology of the northern Murchison Domain, Youanmi Terrane, Yilgarn Craton: Geological Survey of Western Australia, Record 2006/10, 19p.

Steele-MacInnis, M., Han, L., Lowell, R.P., Rimstidt, J.D., and Bodnar, R.J., 2012, The role of fluid phase immiscibility in quartz dissolution and precipitation in sub-seafloor hydrothermal systems: Earth and Planetary Science Letters, v. 321–322, p. 139–151.

Sverjensky, D.A., 1986, Genesis of Mississippi Valley-type lead–zinc deposits: Annual Review of Earth and Planetary Sciences, v. 14, p. 177–199.

Taylor, D., Dalstra, H.J., Harding, A.E., Broadbent, G.C., and Barley, M.E., 2001, Genesis of high-grade hematite orebodies of the Hamersley Province, Western Australia: Economic Geology, v. 96, p. 837–873.

Thorne, W.S., Hagemann, S.G., and Barley, M.E., 2004, Petrographic and geochemical evidence for hydrothermal evolution of the North Deposit, Mt Tom Price, Western Australia: Mineralium Deposita, v. 39, p. 766–783.

Thorne, W.S., Hagemann, S.G., Sepe, D., Dalstra, H.J., and Banks, D.A., 2014, Structural control, hydrothermal alteration zonation, and fluid chemistry of the concealed, high-grade 4EE iron orebody at

the Paraburdoo 4E deposit, Hamersley Province, Western Australia: Economic Geology, v. 109, p. 1529–1562.

Trefry, J.H., Butterfield, D.B., Metz, S., Massoth, G.J., Trocine, R.P., and Feely, R.A., 1994, Trace metals in hydrothermal solutions from Cleft segment on the southern Juan de Fuca Ridge: Journal of Geophysical Research: Solid Earth, v. 99, p. 4925–4935.

Van Kranendonk, M.J. and Ivanic, T.J., 2009, A new lithostratigraphic scheme for the northeastern Murchison Domain, Yilgarn Craton, Geological Survey of Western Australia Annual Review 2007-08, Perth, Western Australia, Geological Survey of Western Australia, p. 34–53.

Von Damm, K.L. and Bischoff, J.L., 1987, Chemistry of hydrothermal solutions from the southern Juan de Fuca Ridge: Journal of Geophysical Research: Solid Earth, v. 92, p. 11334–11346.

Von Damm, K.L., Edmond, J.M., Grant, B., Measures, C.I., Walden, B., and Weiss, R.F., 1985, Chemistry of submarine hydrothermal solutions at 21 ºN, East Pacific Rise: Geochimica et Cosmochimica Acta, v. 49, p. 2197–2220.

Walford, P.C. and Franklin, J.M., 1982, The Anderson lake mine, Snow Lake, Manitoba, in CD Hutchinson, CD Spence and JM Franklin ed., Precambrian sulphide deposits, Waterloo, Ontario, Canada, Geological Association of Canada, p. 481–525.

Wechsler, B.A., Lindsley, D.H., and Prewitt, C.T., 1984, Crystal structure and cation distribution in titanomagnetites (Fe_{3-x} Ti_x O_4): American Mineralogist, v. 69, p. 754–770.

Whalen, J.B. and Chappell, B.W., 1988, Opaque mineralogy and mafic mineral chemistry of I- and S-type granites of the Lachlan fold belt, Southeast Australia: American Mineralogist, v. 73, p. 281–296.

Williams, A.E. and McKibben, M.A., 1989, A brine interface in the Salton Sea Geothermal System, California: Fluid geochemical and isotopic characteristics: Geochimica et Cosmochimica Acta, v. 53, p. 1905–1920.

Wilson, T.P. and Long, D.T., 1993a, Geochemistry and isotope chemistry of Ca–Na–Cl brines in Silurian strata, Michigan Basin, USA: Applied Geochemistry, v. 8, p. 507–524.

Wilson, T.P. and Long, D.T., 1993b, Geochemistry and isotope chemistry of Michigan Basin brines: Devonian formations: Applied Geochemistry, v. 8, p. 81–100.

Wingate, MTD, Kirkland, CL and Ivanic, TJ 2012, 194757: metadolerite, The Gap; Geochronology Record 1016: Geological Survey of Western Australia, 4p.

Wingate, MTD, Kirkland, CL, Van Kranendonk, MJ and Wyche, S 2013, 155569: metarhyolite, Weld Range; Geochronology Record 1096: Geological Survey of Western Australia, 4p.

Yardley, B.W.D., 2013, The chemical composition of metamorphic fluids in the crust, in DE Harlov and H Austrheim ed., Metasomatism and the Chemical Transformation of Rock, Berlin, Heidelberg (Germany), Springer-Verlag, p. 17–51.

Yardley, B.W.D., Banks, D.A., Bottrell, S.H., and Diamond, L.W., 1993, Post-metamorphic gold quartz veins from NW Italy: The composition and origin of the ore fluid: Mineralogical Magazine, v. 57, p. 407–422.

Yardley, B.W.D. and Bodnar, R.J., 2014, Fluids in the continental crust: Geochemical Perspectives, v. 3, p. 1–127.

Zengqian, H., Zaw, K., Rona, P., Yinqing, L., Xiaoming, Q., Shuhe, S., Ligui, P., and Jianjun, H., 2008, Geology, fluid inclusions, and oxygen isotope geochemistry of the Baiyinchang pipe-style volcanic-hosted massive sulfide Cu deposit in Gansu Province, northwestern China: Economic Geology, v. 103, p. 269–292.

Zheng, Y.F., 1999, Oxygen isotope fractionation in carbonate and sulfate minerals: Geochemical Journal, v. 33, p. 109–126.

Figure Captions

Fig. 1. Solid geology map of the Weld Range greenstone belt in Western Australia showing major lithological associations, structures, and locations of the BIF-hosted Beebyn and Madoonga iron deposits (modified after Van Kranendonk and Ivanic, 2009). The region includes multiply-deformed, steeply dipping supracrustal rocks that are locally intruded by granitic rocks. The inset map shows the location of the Weld Range district within the Yilgarn Craton (modified after Guilliamse, 2014)

Fig. 2. Simplified outcrop geology maps and cross sections for the Beebyn and Madoonga deposits. (A) Beebyn lithology and hypogene alteration maps show the location of prospect areas (e.g. W7 and W8) and the NW-SE cross section line. Magnetite-rich ore zones in BIF are located mainly at the W11, W10, and W9 prospects and are flanked by areas of carbonate-altered BIF (modified after Duuring and Hagemann, 2013b). (B) The outcrop geology map for the Madoonga deposit demonstrates that magnetite (-martite) veins are mostly located in the W14 prospect, while specular hematite-quartz vein crop out in the W15 prospect (modified after Duuring and Hagemann, 2013a). (C) Representative cross section for the Beebyn deposit. (D) Cross section for the Madoonga deposit (modified after Duuring and Hagemann, 2013a; Duuring and Hagemann, 2013b)

Fig. 3. Alteration mineral equilibrium assemblages for progressive hypogene and supergene alteration for the Beebyn deposit. Minerals are shown as major (thick bars), common (thin bars), or minor (dashed lines) phases (modified after Duuring and Hagemann, 2013b)

Fig. 4. Hand specimen examples of least-altered BIF and early carbonate±magnetite hypogene alteration at the Beebyn deposit (modified after Duuring and Hagemann, 2013b). (A) Thickly banded, least-altered BIF with alternating silica- and iron oxide-rich bands. (B) Stage 1 alteration: quartz-rich bands are replaced by siderite, ferroan dolomite, and disseminated euhedral magnetite. (C) Stage 2 alteration: ferroan dolomite veins cut primary bands and Stage 1 siderite-magnetite alteration zones. (D) Stage 2 alteration: ferroan dolomite replaces primary quartz bands and locally defines veins that cut primary bands and a Stage 1 siderite alteration zone. Note the minor occurrence of triangular Stage 3 magnetite-carbonate replacement zones. (E) Stage 3 alteration: quartz-rich bands are replaced by coarse-grained Stage 2 ferroan dolomite, which is in turn partly replaced by Stage 3 magnetite-carbonate. (F) Stage 3 alteration: Stage 2 ferroan dolomite is partly replaced by triangular domains of finer-grained Stage 3 ferroan dolomite and magnetite. In this example, cleavage intersections of the coarse-grained ferroan dolomite crystals likely controlled the location of the replacement zones. The asymmetry of the triangular domains in each band demonstrates the direction of progressive replacement of Stage 2 ferroan dolomite and the likely flow direction of Stage 3 fluids across bands in this sample. Abbreviations: Fe-Dol, ferroan dolomite; Mag, magnetite; Sd, siderite

Fig. 5. Hand specimen examples of post-magnetite ore alteration stages in BIF at the Beebyn deposit (modified after Duuring and Hagemann, 2013b). (A) Stage 4 alteration: specular hematite is intergrown with chlorite in shear zones. (B) Stage 4 alteration: primary and hypogene magnetite in proximal wallrock

to Stage 4 chlorite-hematite-altered shear zones are replaced by hematite (i.e. demonstrating the process of martitization). (C) Stage 5 alteration: Stage 2 ferroan dolomite domains are partly replaced by Stage 5 quartz. (D) Stage 6 alteration: ferroan dolomite-rich±quartz veins cut thinly-banded, Stage 4 hematite-chlorite-altered BIF. (E) Stage 7 alteration: 1 to 20 mm-thick, magnetite-siderite-Fe-rich chlorite veins cut primary bands. (F) Supergene-altered BIF displays oxidation of magnetite-rich bands to martite, and partial replacement of silicate minerals by goethite. Abbreviations: Chl, chlorite; Fe-Dol, ferroan dolomite; Gt, goethite; Hem, hematite; KMag, kenomagnetite; Mag, magnetite; Mt, martite; Qtz, quartz; Sd, siderite; Spec-Hem, specular hematite

Fig. 6. Alteration mineral equilibrium assemblages for progressive hypogene and supergene alteration for the Madoonga deposit. Minerals are shown as major (thick bars), common (thin bars), or minor (dashed lines) phases (modified after Duuring and Hagemann, 2013a)

Fig. 7. Hand specimen and matching thin section examples of selected hypogene alteration stages at the Madoonga deposit. (A and B) Semi-massive pyrite is intergrown with microcrystalline quartz and carbonate minerals in mudstone located along the southern margin of the Madoonga South BIF. (C) Madoonga Stage 2 magnetite-talc replaces Stage 1 jaspilite. (D) Madoonga Stage 3 specular hematite-quartz vein (modified after Duuring and Hagemann, 2013a)

Fig. 8. Representative mineral textural relationships and fluid inclusion assemblage maps for key hypogene alteration stages affecting BIF at the Beebyn deposit. (A) Beebyn Stage 1 magnetite-siderite/ferroan dolomite-altered BIF: a primary quartz-rich band has been comprehensively altered to disseminated euhedral magnetite and finer-grained, anhedral ferroan dolomite. (B) The Beebyn Stage 1 ferroan dolomite hosts a three-dimensional pseudosecondary trail of monophase (vapor) carbonic fluid inclusions with minor disseminated (opaque) magnetite inclusions (fluid inclusion assemblage BN-W9-104-C). (C) Beebyn Stage 2 ferroan dolomite veins cut Stage 1 magnetite-siderite±ferroan dolomite-altered bands. (D) Representative Beebyn Stage 2 ferroan dolomite hosts three-phase (L-V-H) aqueous fluid inclusions and disseminated magnetite (fluid inclusion assemblage BN-W10-013-B). Heating shows that these three-phase aqueous-rich fluid inclusion assemblages are completely homogenized by the dissolution of halite within the range of 275 to 327 ºC. The solid labelled as halite in the close-up image of a representative fluid inclusion is triangular and is most likely a sectional view of the corner of a halite cube. (E) A different example of Stage 2 ferroan dolomite that hosts two-phase (L-V) aqueous fluid inclusions with lower homogenization temperatures. The Stage 2 ferroan dolomites host abundant primary fluid inclusions in the centre of each euhedral crystal and contain fewer fluid inclusions with proximity to their grain boundaries. The boarders of some Stage 2 ferroan dolomites are embayed by Stage 5 quartz. (F) Stage 2 ferroan dolomite hosts magnetite inclusions and two-phase (L-V), aqueous, primary fluid inclusions that display lower homogenization temperatures (fluid inclusion assemblage BN-W10-021-F). Note the accidentally trapped solid that did not change with heating in the enlarged image of the F1 fluid inclusion. (G) Beebyn Stage 3 magnetite and ferroan dolomite define a triangular domain in a Stage 2 ferroan dolomite-rich band. Randomly oriented and elongate Stage 3 magnetites are intergrown with Stage 3 ferroan dolomite. (H)

The Beebyn Stage 3 ferroan dolomite hosts two-phase (L-V) fluid inclusions with disseminated magnetite inclusions (fluid inclusion assemblage BN-W10-013-I). All photographs were taken at 25 ºC in transmitted plane-polarized light, apart from photographs (C) and (D), which were taken using transmitted and reflected plane-polarized light. Temperatures for key phase transitions are shown for representative fluid inclusions, with all microthermometry data reported in Table A2. “Null” is used to identify situations where specific phase transitions were not observed. In the case of the carbonic fluid inclusions in (B), temperatures for CO_2 final melting and vapor homogenization are shown. For fluid inclusions that contain halite daughter crystals (D) temperatures are given for initial melting, homogenization to vapor, and halite melting transitions. For the two-phase aqueous fluid inclusions (F and H), temperatures are shown for initial melting, final ice melting, and final homogenization

Fig. 9. Representative mineral textural relationships fluid inclusion assemblage maps for post-ore alteration stages affecting BIF at the Beebyn deposit and the Madoonga Stage 3 specular hematite-quartz event. (A) Beebyn Stage 5 quartz replaces Stage 2 ferroan dolomite along cleavage planes. (B) Beebyn Stage 5 quartz hosts a cluster of three-phase (L-V-H) aqueous fluid inclusions and minor magnetite inclusions (fluid inclusion assemblage BN-W10-024-A). (C) Beebyn Stage 6 ferroan dolomite and disseminated subhedral magnetite define a 1 cm-wide vein that cuts magnetite-rich bands in BIF. (D) The Beebyn Stage 6 ferroan dolomite contains abundant two-phase (L-V), aqueous, primary fluid inclusions and magnetite in the centre of the crystal and demonstrates a later growth phase of fluid inclusion-free ferroan dolomite (fluid inclusion assemblage BN-W10-014-B). (E) Beebyn Stage 7 magnetite-siderite-Fe-rich chlorite vein cuts altered primary bands in BIF. A cluster of fluid inclusions is hosted by siderite with two prominent directions of cleavage shown. (F) Beebyn Stage 7 siderite hosts two-phase (L-V) aqueous fluid inclusions (fluid inclusion assemblage BN-W10-026-A). (G) Madoonga Stage 3 specular hematite-quartz vein from the W19 prospect shows specular hematite intergrown with coarse-grained, crystalline quartz. (H) Madoonga Stage 3 quartz hosts a central mineral growth zone defined by three-phase (L-V-H) primary fluid inclusions (fluid inclusion assemblage MD-W19-M02b-A2). All photographs were taken at 25 ºC in transmitted plane-polarized light, apart from photograph (G), which was taken using transmitted and reflected plane-polarized light. Temperatures for key phase transitions are shown for representative fluid inclusions, with all microthermometry data reported in Table A2. “Null” is used to identify situations where specific phase transitions were not observed. For fluid inclusions that contain halite daughter crystals (B and H) temperatures are given for initial melting, homogenization to vapor, and halite melting transitions. For the two-phase aqueous fluid inclusions (D and F), temperatures are shown for initial melting, final ice melting, and final homogenization

Fig. 10. Raman spectra image of a carbonic primary fluid inclusion hosted by Beebyn Stage 1 ferroan dolomite (fluid inclusion assemblage BN-W9-104-C). (A) Optical photograph of the analyzed fluid inclusion in ferroan dolomite, taken in reflected plane-polarized light at about 25 ºC. (B) Spectra of the homogeneous CO_2-rich fluid inclusion (in red) hosted by ferroan dolomite (blue). (C) Single point Raman spectrum showing the wavenumber intervals for the analyzed fluid inclusion, indicating the presence of CO_2 and the ferroan dolomite host. (D) Single point Raman spectrum for a representative area of the ferroan dolomite

host

Fig. 11. Box and whisker plots showing microthermometry data for fluid inclusion assemblages from hypogene fluid alteration stages affecting BIF in the Beebyn and Madoonga deposits. (A) Initial melting temperatures and T_{mCO2} for carbonic fluid inclusions. (B) Temperatures of total homogenization. (C) Calculated salinities. (D) Calculated densities. Dashed lines indicate densities for pure water (1.0 g/cm^3 at 4.0 ºC) and modern seawater (1.028 g/cm^3 at 4.0 ºC, assuming a salinity of 35 g/kg). Also shown for reference is the 1.0 to 1.3 g/cm3 density range of high salinity-type fluid inclusions from porphyry copper deposits at Bingham Canyon (Roedder, 1971). For box and whiskers, the upper and lower margins of each box represent the upper and lower 50 percentile of the data. The whiskers represent the upper and lower threshold values (95 percentile of the data). Median values are shown as solid black lines and mean values as solid black circles. Boxes are colored based on hand specimen samples

Fig. 12. Box and whisker plots showing cation and anion molar ratios for fluid inclusions liberated from separates of hypogene-altered BIF from the Beebyn and Madoonga deposits. (A) Cl/Br molar ratios. (B) Na/Br molar ratios. (C) Na/Cl molar ratios. (D) Na/K molar ratios. (E) Na/SO_4 molar ratios

Fig. 13. Comparison of representative LA-ICP-MS spectra for fluid inclusions hosted in ferroan dolomite (A and B) and quartz (C and D). In all examples, fluid inclusion signals are defined by prominent asymmetric peaks for Na and K. In the quartz examples, additional element peaks are identified for Ca, Fe, Mg, and Mn, whereas in the ferroan dolomite examples the presence of a fluid inclusion signature for these elements cannot be distinguished from the composition of the ferroan dolomite host

Fig. 14. Box and whisker plot that shows cation ratios versus Na for fluid inclusions analyzed by LA-ICP-MS. Data are grouped by hypogene alteration stages affecting BIF

Fig. 15. Box and whisker plots showing cation ratios versus Na for fluid inclusion assemblages from the different stages of hypogene alteration in BIF

Fig. 16. Carbon and oxygen stable isotope fluid data calculated from analyzed quartz and carbonate minerals from hypogene-altered BIF in the Beebyn and Madoonga deposits. The paired carbon and oxygen isotopic fluid values are from carbonate mineral separates, whereas stand-alone, oxygen isotopic data are for quartz analyzed with the CAMECA IMS 1280 ion probe. Also shown are reference isotopic values for common rock types and fluid sources (i.e. solid line boxes) reported by Sharp (2006). Carbon and oxygen isotope ranges for Archean seawater (i.e. dashed line boxes) are sourced from two alternate geological models; (i) C and O isotopic data derived from chemical sediments and compiled by Prokoph et al. (2008) and (ii) O isotopic fluid data interpreted from Archean seawater alterations and formation of serpentinites from the 3.8 Ga Isua supracrustal belt, Greenland (Pope et al., 2012). Oxygen isotope ranges for meteoric waters, basaltic rocks, and sedimentary rocks are from Hoefs (2009)

Fig. 17. SEM images of magnetite and hematite grains from altered BIF from the Beebyn and Madoonga deposits that were analyzed by LA-ICP-MS. All images were collected using backscattered secondary electron conditions, with an accelerating voltage of 20.0 kV and a beam intensity of 15.00. Image (D) was taken using maximum contrast settings to highlight compositional differences between magnetite (bright) and martite (darker)

Fig. 18. Box and whisker plots showing selected minor and trace element abundances in magnetite and hematite as determined by LA-ICP-MS. Data are plotted for each element in order of hypogene alteration stage at the Beebyn and Madoonga deposits

Fig. 19. Salinity versus total homogenization temperatures for aqueous-rich fluid inclusion assemblages hosted by hypogene carbonate minerals and quartz from the Beebyn and Madoonga deposits. (A) Beebyn Stages 2 and 3 magnetite-carbonate replacement of primary silica-rich bands in BIF. (B) Beebyn Stages 5 to 7 represent post-ore alteration events affecting BIF. (C) Madoonga Stage 3 specular hematite-quartz veins. (D). All data plotted for comparison

Fig. 20. Diagrams showing cation and anion molar ratios for fluid inclusions obtained from separates of hypogene-altered BIF from the Beebyn and Madoonga deposits. (A) Na/Cl vs. Cl/Br molar ratio. (B) Na/Br vs. Cl/Br molar ratio. (C) Na/K vs. Cl/Br molar ratio. (D) Na/SO_4 vs. Cl/Br molar ratio. The grey shaded boxes represent Cl/Br ranges for magmatic fluids based on values reported by Bohlke and Irwin (1992), Banks et al. (2000b), Johnson et al. (2000), Kendrick et al. (2001), Banks et al. (2002), and Baker et al. (2006). Compositional ratios for 3.2 Ga seawater, 3.2 Ga vent fluid, and modern seawater are from De Ronde et al. (1997). The arrow intersecting the 3.2 Ga vent fluid position marks the compositional trajectory of Paleoproterozoic seawater demonstrated by Gutzmer et al. (2003), whereas the arrow intersecting the average value for modern seawater shows the compositional range from literature data compiled by Gutzmer et al. (2003). The dashed coloured lines in each binary diagram represent the compositional ranges for black smoker fluids, geothermal brines, seawater, oil field formation waters, low-grade metamorphic fluids, orogenic Au-quartz fluids, basinal fluids from basement rocks, and magmatic fluids based on summary data reported by Yardley (2013) and Yardley and Bodnar (2014), with original sources for the data indicated in Fig. 21

Fig. 21. (A) Cl/Br molar ratio versus Ca/Ca+Na molar ratio and (B) log (K/Na) versus 1/T for fluid compositional data for fluids hosted by Beebyn and Madoonga hypogene alteration stages in BIF. The Beebyn and Madoonga fluid data are derived by crush-leach analysis (filled symbols) and LA-ICP-MS on fluid inclusions (open symbols). Fields for a range of natural crustal fluids and the microcline-albite equilibrium curve (dashed line) are shown for comparison. These ranges are contoured from data presented by Yardley and Bodnar (2014) with original data derived from: a, North Sea Formation Waters (Smalley and Warren, 1994); b, Central Mississippi brines (Carpenter et al., 1974); c, Alberta Basin Brines (Connolly et al., 1990); d, Michigan Basin (Wilson and Long, 1993a; Wilson and Long, 1993b); e, Offshore Louisiana (Land et al., 1988); f, Columbian Emerald deposits (Banks et al., 2000a); g, Modum Complex

(Munz et al., 1995); h, Salton Sea geothermal brines (Williams and McKibben, 1989); i, Cornwall (Bottrell et al., 1988; Smith et al., 1996); j, Mole Granite (Audetat et al., 2000a; Audetat et al., 2000b); k, Capitan Pluton (Campbell et al., 1995); l, Kakkonda Granite Brine (Kasai et al., 1996); m, Orogenic Au-quartz fluids from Brusson, northern Italy (Yardley et al., 1993). The compositional field “n” for Black smoker fluids is sourced from Von Damm et al. (1985), Bowers et al. (1988), Von Damm and Bischoff (1987), Campbell et al. (1988), James et al. (1995), and Trefry et al. (1994). Black smoker compositional field “o” is derived from compiled end-member fluid composition data reported by James et al. (2014) for the East Scotia Ridge, as well as other vent fluids from back-arc basins and mid-ocean ridge sites in the Atlantic, Pacific, and Indian oceans closes to the East Scotia Ridge (see James et al., 2014 for sources)

Fig. 22. Ternary plots showing LA-ICP-MS data for fluid inclusions hosted by ferroan dolomite and quartz at the Beebyn and Madoonga deposits. Fields for a range of natural crustal fluids are shown for comparison, with details about data sources included in Figure Fig. 21. Fluid fields shown in Fig. 22B are of natural and experimentally produced MVT brines (Carpenter et al., 1974; Sverjensky, 1986; Kharaka et al., 1987), whereas the region “A” shows the composition of Pb-rich brines from the central Mississippi and southwest Arkansas (modified after Marie et al., 2001)

Fig. 23. Magnetite and hematite mineral chemistry data for diagenetic/metamorphic and hypogene alteration stages at the Beebyn and Madoonga deposits. (A) Ga vs. Al plot tests for possible inheritance of least mobile elements in successive hypogene magnetite stages at the Beebyn deposit. Data for hypogene specular hematite are shown for comparison. (B) Mg/W vs. Mn/Al differentiates the multiple stages of hypogene magnetite and hematite alteration at the Beebyn and Madoonga deposits. (C) Mn vs. Ti plot showing the clear separation of hypogene magnetite from diagenetic/metamorphic magnetite at the Beebyn deposit. (D) Al + Mn vs. Ti + V plot with deposit fields proposed by Dupuis and Beaudoin (2011), Nadoll (2011), and Nadoll et al. (2014). Magnetite compositional data from Beebyn and Madoonga coincide with the compositional range of magnetite from BIF defined by Nadoll et al. (2014), with Stages 1, 3 and 7 magnetite most similar in composition to hydrothermal magnetite from Ag-Pb-Zn veins. (E) Al/Ga vs. Mn/Ti plot that shows the effects of hypogene alteration on magnetite chemistry.

Fig. 24. Fluid alteration model for hypogene magnetite and specular hematite orebodies in BIF in the Weld Range district. (A) The Beebyn Stage 1 event involved upward movement of hot, silica-poor, magmatic-derived fluids through mafic igneous rocks and BIF. Phase separation resulted in a CO_2-rich fluid that replaced primary quartz bands with Stage 1 siderite and ferroan dolomite. Dissolve silica was transported away from the carbonate-altered BIF and potentially released into the ancient ocean. (B) The Stage 2 event represents the transition from a magmatic- to an emerging seawater-dominated hydrothermal system with time (and distance from central fluid pathways). Hot, silica-poor, reduced, aqueous fluids, with magmatic and seawater isotopic and compositional signatures, continued to replace primary quartz bands with ferroan dolomite. (C) The Stage 3 event is marked by the termination of the magmatic-dominated system, and the circulation of lower-temperature, silica-poor seawater along existing fluid pathways. Stages 1 and 2 carbonate minerals are replaced by Stage 3 magnetite and minor ferroan dolomite. In

addition, the Stage 3 alteration event was associated with a volume decrease in BIF, the residual concentration of primary magnetite-rich bands, and the genesis of the magnetite replacement-style orebody at the Beebyn deposit. (D) The Stage 4 event is characterized by specular hematite-quartz veins hosted by shear zones at the Beebyn and Madoonga deposits. These narrow zones post-date the folding and tilting of the Weld Range lithotectonic unit and the magnetite replacement-style orebody. Iron was most likely mobilized within BIF in its reduced state by heated meteoric fluids or seawater and precipitated as a consequence of oxidation and cooling of the fluid.

Tables

Table 1 Summary of all hypogene fluid data and interpretations for the Beebyn deposit
Table 2 Summary of all hypogene fluid data and interpretations for the Madoonga deposit

Appendix. Supplementary electronic data

Appendix 1 Methods

Appendix 2 Hand specimen and matching thin section examples of progressive hypogene alteration in North BIF from Duuring et al. (2013b). (A and B) Stage 1 alteration: quartz-rich bands are partly replaced by fine-grained Stage 1 siderite with disseminated clusters of euhedral Stage 1 hypogene magnetite. (C and D) Stage 2 alteration: coarse-grained, subhedral, ferroan dolomite replaces primary quartz-rich bands. Note the subsequent partial replacement of Stage 2 ferroan dolomite by Stage 3 magnetite-carbonate. (E and F) Stage 3 alteration: Stage 2 ferroan dolomite is partly to completely replaced by fine-grained, subhedral Stage 3 carbonate minerals and euhedral, mineral inclusion-poor magnetite. (G and H) Stage 4 alteration: a specular hematite-chlorite altered shear zone in BIF. Coarse-grained, bladed hematite grains are partly replaced by kenomagnetite. (I and J) Stage 5 alteration: Fine- to coarse-grained, anhedral to euhedral, translucent Stage 5 quartz locally replaces Stages 2 and 3 ferroan dolomite. (K and L) Stage 6 alteration: ferroan dolomite-rich±quartz veins cut thinly-banded, Stage 4 hematite-chlorite-altered BIF. Stage 6 ferroan dolomite crystals are coarse-grained and euhedral. (M and N) Stage 7 alteration: minor, 1 to 20 mm-thick, magnetite-siderite-Fe-rich chlorite veins. (O and P) Supergene-altered BIF displays the oxidation of magnetite-rich bands to kenomagnetite and martite, and partial replacement of silicate minerals by goethite. Thin section photomicrographs were taken in transmitted cross-polarized light (B and D), reflected plane-polarized light (F, H, P), and a combination of transmitted and reflected plane-polarized light (J, L, N). Abbreviations: Cal, calcite; Cb, carbonate minerals; Chl, chlorite; Fe-Dol, ferroan dolomite; Gt, goethite; Hem, hematite; KMag, kenomagnetite; Mag, magnetite; Mt, martite; Qtz, quartz; Sd, siderite; Spec-Hem, specular hematite

Appendix 3 Hand specimen and matching thin section examples of the step-wise hypogene alteration of the North and South BIF units at the Madoonga deposit from Duuring et al. (2013a). (A and B) Stage 1 jaspilite with alternating Fe oxide- and silica-rich (jasper) bands. (C and D) Stage 2 magnetite-talc

replacement of Stage 1 jaspilite. Bladed Stage 2 magnetite is intergrown with fibrous talc. (E and F) Stage 2 magnetite-talc preferentially replaces silica-rich bands. (G and H) Stage 3 specular hematite is intergrown with coarse-grained, crystalline quartz. Specular hematite hosts patches of kenomagnetite that are partly replaced by finer-grained hematite. (I and J) Silica- and Fe oxide-rich bands are partly replaced by disseminated coarse-grained, euhedral, microplaty hematite. (K and L) Stage 4 siderite-quartz vein cuts and hosts fragments of siderite-altered BIF. (M and N) Stage 5 chlorite-pyrite vein cuts Stage 2 magnetite-talc-altered BIF. (P and P) Stage 6 quartz preferentially replaces silica-rich bands in jaspilite. Thin section photomicrographs were taken in transmitted plane-polarized light (B, L, N, P), reflected plane-polarized light (F, H, J), and a combination of transmitted and reflected plane-polarized light (D). Abbreviations: Cal, calcite; Cb, carbonate minerals; Chl, chlorite; Hem, hematite; KMag, kenomagnetite; Mag, magnetite; Mplaty Hem, microplaty hematite; Mt, martite; Qtz, quartz; Py, pyrite; Sd, siderite; Spec-Hem, specular hematite; Tlc, talc

Table A1 Summary of microthermometry data from the Beebyn and Madoonga deposits, Weld Range iron camp

Table A2 Microthermometry data from the Beebyn and Madoonga deposits, Weld Range iron camp

Table A3 Cation and anion concentrations in fluid inclusions from the Beebyn and Madoonga deposits, Weld Range iron camp

Table A4 Summary LA-ICP-MS data for fluid inclusion compositions from the Beebyn and Madoonga deposits, Weld Range iron camp

Table A5 LA-ICP-MS data for fluid inclusion compositions from the Beebyn and Madoonga deposits, Weld Range iron camp

Table A6 Oxygen isotope data for diagenetic or metamorphosed quartz from primary silica-rich bands in BIF and selected quartz-bearing hypogene alteration zones in BIF from the Beebyn and Madoonga deposits

Table A7 Oxygen and carbon isotope compositions of hypogene carbonate alteration stages at the Beebyn and Madoonga deposits, Weld Range iron camp

Table A8 Oxygen isotope values and calculated temperatures for Stage 1 hypogene magnetite at the Beebyn deposit, Weld Range iron camp

Table A9 LA-ICP-MS summary data for magnetite and hematite from the Beebyn and Madoonga deposits, Weld Range iron camp

Table A10 LA-ICP-MS mineral chemistry data for magnetite and hematite from the Beebyn and Madoonga deposits, Weld Range iron camp

Table A11 Summary of all hypogene fluid data and interpretations for the Beebyn and Madoonga deposits

Table A12 Average detection limits for each element analyzed by LA-ICP-MS, using a laser beam spot size of 75 μm

Table 1 Summary of all hypogene fluid data and interpretations for the Beebyn deposit

Hypogene fluid event	Timing	Alteration mineral assemblage	Microthermometry (primary FIA)	Cation contents	Minimum trapping temperatures (°C)	Calculated salinities (equiv. wt.% NaCl or $CaCl_2$)	Ion chromatography	In-situ LA-ICP-MS data for fluid inclusions (listed in order of abundance)	$\delta^{13}C_{CO2}$ (‰) V-PDB	$\delta^{18}O_{H2O}$ (‰) V-SMOW	C and O isotope interpretation	In-situ LA-ICP-MS data for magnetite and hematite (relative to metamorphic magnetite or Beebyn Stage 4 martite compositions)	Whole-rock geochemistry (relative to least-altered BIF)	Interpreted fluid source citing key supporting evidence
Beebyn Stage 1	Pre-ore	Magnetite-siderite ± ferroan dolomite	Monophase (vapor-rich), carbonic, low-density (0.65 to 0.79 g/cm^3)		444 to 465				-5.27 to -4.29	7.23 to 9.97	Overlaps reported ranges for magmatic, carbonatite, metamorphic; as well as semi-massive pyrite-quartz veins at Madoonga	Enrichments: Mg, Mn, Ba, Mo, P, Rb, Ti, V, As, Ca, K, Na, Pb, Sc, Sr, and W. Depletions: Si		**Magmatic fluids:** high-temperature (>445 °C), carbonic, alkaline, reduced fluid. Potentially evidence for fluid boiling, phase immiscibility, and trapping vapor-only fluid inclusions. C and O isotopes are comparable to reported ranges for magmatic fluids. Stage 1 fluids are enriched in Ca, Mg, Mn, Rb, W, Sr, P, K, Na, Ba, C, Fe, Ti, V, As, Ca, Pb, Sc, and Mo; depleted in Si. Fluid contents are likely affected by chemical exchange with surrounding mafic country rocks. Siderite-ferroan dolomite-magnetite replaced primary silica-rich bands as a result of kilometer-scale, fluid circulation and replacement processes, controlled by the prograde solubility of quartz and retrograde solubility of carbonate minerals
Beebyn Stage 2	Pre-ore	Ferroan dolomite ± magnetite ± apatite ± monazite ± xenotime	Higher-temperature FIA: three-phase (liquid-vapor-halite), aqueous-rich	Mixed	275 to 327	36 to 40	Cl-dominant, Na, K, SO_4, and Br. Molar Cl/Br indicate halite dissolution and overlaps magmatic fluid values. Significant cation exchange between the fluid and mafic country rocks, enriching Na in the fluid	Fe, Ca, ?Mg, Mn, Na, K, Sr, Cu, Ba, Zn, Pb, W, and Co. Enriched in Cu and Zn relative to Pb. Mn-rich fluids are compatible with reported data for magmatic fluids, black smoker fluids, and geothermal brines	-10.36 to -10.11	-0.45 to 1.01	Overlaps reported ranges for magmatic, carbonatite, metamorphic, and locally with Archean seawater		Beebyn Stages 1 and 2 were not analyzed separately. Enrichments: CaO, Rb, W, Sr, K_2O, Na_2O, P_2O_5, MgO, Ba, LOI, C, Fe_2O_{3T}, and MnO. Depletions: SiO_2, Cr, Ta, Sc, S, Mo, and Pb	**Magmatic fluids with local influence from Archean seawater**: higher-temperature (>275 °C), alkaline, reduced, high-salinity brines that are Cl-dominant and contain multiple cations, including Fe, Ca, Mg, Mn, Na, K, Rb, P, Sr, Cu, Ba, Zn, Pb, W, S, and Co; depleted in Si. Cl/Br values overlap reported magmatic fluid ranges and indicate the Stage 2 fluid dissolved halite, possibly via interaction with an evaporite. C and O isotopes are comparable to magmatic fluids, with local interaction from Archean seawater. Major addition of Na to the fluid from mafic country rock. Stage 2 alteration minerals replaced primary silica-rich bands on a kilometer scale with local development of veins
			Lower-temperature FIA: two-phase (liquid-vapor), aqueous-rich	Mixed	125 to 257	3 to 23			-7.03 to -6.54	0.99 to 7.42	Overlaps reported ranges for Archean seawater with interaction with organic carbon from mudstones and shales			**Magmatic fluids with major influence from Archean seawater**: lower-temperature (>125 to 257 °C), alkaline, reduced, low to high-salinity brines that are Cl-dominant and contain multiple cations, including Fe, Ca, Mg, Mn, Na, K, Rb, P, Sr, Cu, Ba, Zn, Pb, W, S, and Co; depleted in Si. Cl/Br values overlap reported magmatic fluid ranges and indicate the Stage 2 fluid dissolved halite, possibly via interaction with an evaporite. C and O isotopes are comparable to magmatic fluids, but interacted with Archean seawater and organic carbon from shales and mudstones. Addition of Na to the fluid through interaction with mafic country rocks. These lower-temperature fluids have a temporal and/or spatial distinction from the higher-temperature fluids, but are considered to be part of the overall Stage 2 event
Beebyn Stage 3	Syn-ore (magnetite)	Magnetite-ferroan dolomite ± pyrite ± chalcopyrite	Two-phase (liquid-vapor), aqueous-rich	Mixed	98 to 175	4 to 17	Cl-dominant, Na, K, SO_4, and Br. Molar Cl/Br indicate halite precipitation and similar to Archean seawater and vent fluid values	Fe, Ca, ?Mg, Mn, Na, K, Sr, Ba, Zn, Pb, and Co. Mn-rich fluids are compatible with reported data for magmatic fluids, black smoker fluids, and geothermal brines				Enrichments: As, Ba, Ca, K, Mo, Na, Pb, Sr, W, Mg, Mn, Ti, V, Bi, Cr, Cu, Ge, and Nb. Depletions: Si	Enrichments: Rb, K_2O, Pb, CaO, Sr, Ba, W, Cu, P_2O5, Sc, and Fe_2O_{3T}. Depletions: SiO_2, Cr, Mo, LOI, Ni, and C	**Modified Archean seawater:** lower-temperature (>98 to 175 °C), alkaline, reduced, low to high-salinity brines that are Cl-dominant and contain multiple cations, including Fe, Ca, Mg, Mn, Na, K, Rb, P, Sr, Sc, Cu, Ba, Zn, Pb, W, S, As, Mo, Bi, Cr, and Co; depleted in Si. Cl/Br values overlap reported fluid ranges for Archean seawater and Archean vent fluids. Alteration was by replacement of Stage 1 and 2 carbonate minerals, localized as a series of 50 m to 1 km-long lenses within the broader Stages 1 and 2 carbonate alteration halo
Beebyn Stage 4	Syn-ore (specularite)	Hematite-chlorite ± talc										Enrichments: Al, As, Ba, Bi, Ca, Cu, Mo, Nb, P, Sb, Sc, Sr, Ta, Ti, U, V, and W. Depletions: Ge, Ni, and Si	Enrichments: K_2O, Ga, V, Zn, Cu, Na_2O, Sr, Rb, Nb, Mo, Th, U, La, Ce, Pr, Nd, Sm, and Fe_2O_{3T}. Depletions: C and SiO_2	**Syn-tectonic hydorthermal fluid (syn-folding and shearing):** oxidized fluid enriched in Si, As, Ba, Bi, Ca, Cu, Fe, K, Mo, Na, Nb, P, Rb, Sb, Sc, Sr, Ta, Ti, Th, U, V, W, and Zn. Vein and shear zone-hosted
Beebyn Stage 5	Post-ore	Quartz-magnetite ± chalcopyrite	Three-phase (liquid-vapor-halite), aqueous-rich	Mixed	133 to 196	28 to 32	Cl-dominant, Na, K, SO_4, and Br. Molar Cl/Br indicate halite dissolution and affinities with low-grade metamorphic fluids, geothermal brines, or oil field formation waters. Major cation exchange for Na	Ca, Na, Fe, Mg, K, Mn, Cu, Sr, Ba, Zn, Pb, Bi, Sn, Co, and W. Enriched in Cu and Zn relative to Pb. Mn-content is comparable with reported data for geothermal brines, low-grade metamorphic fluids and basinal brines from basement rocks		-2.51 to 1.47	High degrees of interaction with Archean seawater and/or meteoric fluids			**Modified Archean seawater and possible meteoric waters:** lower-temperature (>133 to 196 °C), reduced, high-salinity brines that are Cl-dominant and contain multiple cations, including Si, Ca, Na, Fe, Mg, K, Mn, Cu, Sr, Ba, Zn, Pb, Bi, Sn, S, Co, and W. Cl/Br values overlap reported fields for low-grade metamorphic fluids, geothermal brines, or oil field formation waters; and indicate halite dissolution with significant cation exchange for Na. C and O isotopes are comparable to values for Archean seawater or meteoric waters. Minor fluid alteration event
Beebyn Stage 6	Post-ore	Calcite-ferroan dolomite ± magnetite ± pyrite ± chalcopyrite	Two-phase (liquid-vapor), aqueous-rich	Mixed	115 to 152	10 to 19		?Fe, ?Ca, ?Mg, ?Mn, Na, K, Sr, Ba, Pb, Zn, W, and Co	-10.97 to -5.47	-2.84 to 2.05	High degrees of interaction with Archean seawater and/or meteoric fluids, with local influences of organic carbon	Enrichments: Ba, Ge, Sr, V, Mg, and Mn. Depletions: Si, Sb, Ni, W, and Ti		**Modified Archean seawater and possible meteoric waters:** lower-temperature (>115 to 152 °C), reduced, moderate-salinity brines with multiple cations, including Fe, Ca, Mg, Mn, Na, K, Sr, Ba, Ge, V, Pb, Zn, S, W, and Co; depleted in Si. C and O isotopes are comparable to values for Archean seawater or meteoric waters, with local interaction with organic carbon from shales. Minor fluid alteration event
Beebyn Stage 7	Post-ore	Siderite-magnetite	Two-phase (liquid-vapor), aqueous-rich	Mixed	125 to 180	12 to 17						Enrichments: As, Ba, Ca, Ge, Mg, Mn, Mo, Na, P, Pb, Rb, Sr, Ti, and V. Depletions: Si and Zn		**Modified Archean seawater and possible meteoric waters:** lower-temperature (>125 to 180 °C), reduced, moderate-salinity brines with multiple cations, including Fe, As, Ba, Ca, Ge, Mg, Mn, Mo, Na, P, Pb, Rb, Sr, Ti, and V; depleted in Si. Minor fluid alteration event

Table 2 Summary of all hypogene fluid data and interpretations for the Madoonga deposit

Hypogene fluid event	Timing	Alteration mineral assemblage	Microthermometry (primary FIA)	Cation contents	Minimum trapping temperatures (°C)	Calculated salinities (equiv. wt.% NaCl or $CaCl_2$)	Ion chromatography	In-situ LA-ICP-MS data for fluid inclusions (listed in order of abundance)	$\delta^{13}C_{CO2}$ (‰) V-PDB	$\delta^{18}O_{H2O}$ (‰) V-SMOW	C and O isotope interpretation	In-situ LA-ICP-MS data for magnetite and hematite (relative to metamorphic magnetite)	Whole-rock geochemistry (relative to least-altered BIF)	Interpreted fluid source citing key supporting evidence
Madoonga Stage 1	Pre-ore	Hematite												**Diagenesis or early regional low-grade metamorphism:** district-wide event
Madoonga Stage 2	Syn-ore (magnetite)	Magnetite-talc ± apatite ± monazite ± xenotime					Cl-dominant, Na, K, SO_4, and Br. Molar Cl/Br indicate halite dissolution and affinities with low-grade metamorphic fluids, geothermal brines, or oil field formation waters. Major cation exchange for Na					Enrichments: Ca, Cr, K, Mo, P, Sc, Ti, U, and V. Depletions: Mn and Si	Enrichments: Fe_2O_{3T}, P_2O_5, Na_2O, K_2O, CaO, MgO, Sc, Ba, Sr, Ga, Zn, and Pb. Depletions in SiO_2, Cr, Mo, and MnO	**Syn-tectonic hydrothermal fluid (faulting):** reduced brine with Fe, Na, K, Ca, Mg, Cr, K, Mo, P, Sc, Ba, Sr, Ga, Zn, Pb, S, Ti, U, and V; depleted in Si. Cl/Br values overlap reported fields for low-grade metamorphic fluids, geothermal brines, or oil field formation waters; and indicate halite dissolution with significant cation exchange for Na
			W15 prospect: two-phase (liquid-vapor), aqueous-rich	Na-dominant	108 to 222	0 to 22	Cl-dominant, Na, K, SO_4, and Br. Molar Cl/Br indicate halite dissolution and affinities with low-grade metamorphic fluids, geothermal brines, or oil field formation waters. Minor cation exchange for Na	Fe, Ca, Na, Mg, K, Mn, Cu, Sr, Ba, Zn, Pb, Sn, Co, W, and Bi. Enriched in Cu and Zn relative to Pb.				Enrichments: Ga, Cu, and Zn. Depletions: Si, Mg, Ti, Cr, Co, and Mo		**Syn-tectonic hydorthermal fluid (Archean seawater):** lower-temperature (>108 to 222 °C), oxidized, low to moderate-salinity brines that are NaCl-dominant and additionally contain Fe, Ca, Mg, K, Mn, Cu, Sr, Ba, Zn, Pb, S, Ga, Sn, Co, W, and Bi. Cl/Br values overlap reported fields for low-grade metamorphic fluids, geothermal brines, or oil field formation waters; and indicate halite dissolution with minor cation exchange for Na through albitization of mafic country rocks. Vein and shear zone-hosted
Madoonga Stage 3	Syn-ore (specularite)	Hematite-quartz	W19 prospect: three-phase (liquid-vapor-halite), aqueous-rich	Mixed	132 to 146	29 to 30	Cl-dominant, Na, K, SO_4, and Br. Molar Cl/Br indicate halite dissolution and affinities with low-grade metamorphic fluids, geothermal brines, or oil field formation waters. Significant cation exchange for Na	Fe, Ca, Na, Mg, K, Mn, Cu, Sr, Ba, Zn, Pb, Sn, Co, W, and Bi. Enriched in Cu and Zn relative to Pb		-6.73 to -6.34	High degrees of interaction with Archean seawater and/or meteoric fluids			**Syn-tectonic hydorthermal fluid (Archean seawater):** lower-temperature (>132 to 146 °C), oxidized, high-salinity brines that are CaCl-dominant and additionally contain Fe, Na, Mg, K, Mn, Cu, Sr, Ba, Zn, Pb, S, Ga, Sn, Co, W, and Bi. Cl/Br values overlap reported fields for low-grade metamorphic fluids, geothermal brines, or oil field formation waters; and indicate halite dissolution with cation exchange for Na through albitization of mafic countre rocks. O isotopes are comparable to values for Archean seawater or meteoric waters. Vein and shear zone-hosted. Potentially demonstrates greater fluid interaction with mafic country rocks at the W19 prospect, compared with the NaCl-dominant and lower-salinity fluids measured at the W15 prospect
Madoonga Stage 4	Post-ore	Siderite-quartz							-9.04	-3.12	High degrees of interaction with Archean seawater and/or meteoric fluids, with local influences of organic carbon			**Archean seawater or meteoric waters:** alkaline fluid containing Fe and Si. C and O isotopes are comparable to values for Archean seawater or meteoric waters, with local interaction with organic carbon. Minor fluid alteration event
Madoonga Stage 5	Post-ore	Chlorite-pyrite ± chalcopyrite												
Madoonga Stage 6	Post-ore	Quartz-ferroan dolomite ± pyrite							-12.33 to -6.22	-8.76 to -0.63	High degrees of interaction with Archean seawater and/or meteoric fluids, with local influences of organic carbon			**Archean seawater or meteoric waters:** alkaline fluid containing Fe, Si, Mg, and S. C and O isotopes are comparable to values for Archean seawater or meteoric waters, with local interaction with organic carbon. Minor fluid alteration event

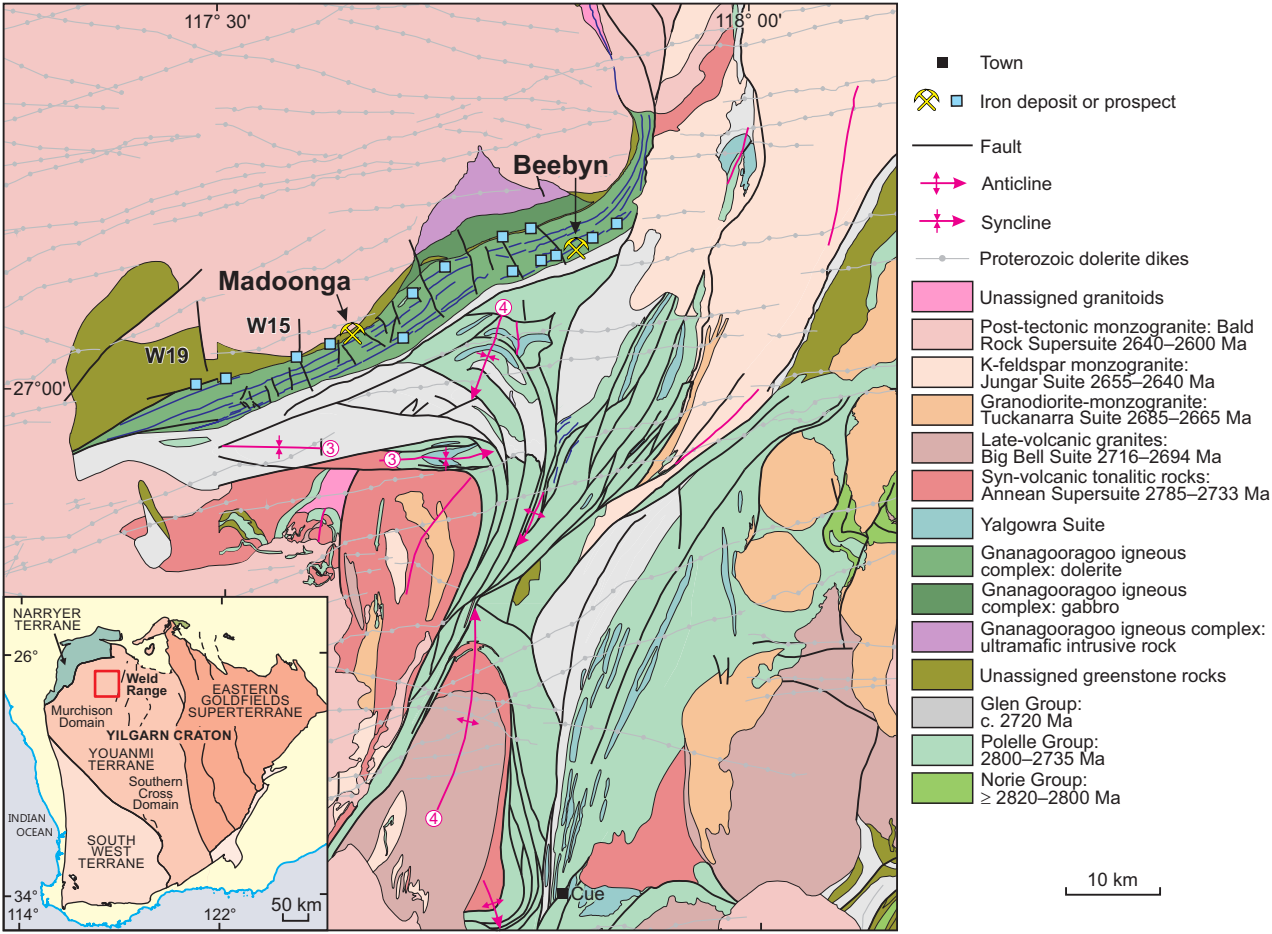
117° 30'
118° 00'
27°00'
Beebyn
Madoonga
W15
W19
Cue
Town
Iron deposit or prospect
Fault
Anticline
Syncline
Proterozoic dolerite dikes
Unassigned granitoids
Post-tectonic monzogranite: Bald Rock Supersuite 2640–2600 Ma
K-feldspar monzogranite: Jungar Suite 2655–2640 Ma
Granodiorite-monzogranite: Tuckanarra Suite 2685–2665 Ma
Late-volcanic granites: Big Bell Suite 2716–2694 Ma
Syn-volcanic tonalitic rocks: Annean Supersuite 2785–2733 Ma
Yalgowra Suite
Gnanagooragoo igneous complex: dolerite
Gnanagooragoo igneous complex: gabbro
Gnanagooragoo igneous complex: ultramafic intrusive rock
Unassigned greenstone rocks
Glen Group: c. 2720 Ma
Polelle Group: 2800–2735 Ma
Norie Group: ≥ 2820–2800 Ma
10 km
NARRYER TERRANE
26°
Weld Range
Murchison Domain
EASTERN GOLDFIELDS SUPERTERRANE
YILGARN CRATON
YOUANMI TERRANE
Southern Cross Domain
INDIAN OCEAN
SOUTH WEST TERRANE
34°
114°
122°
50 km

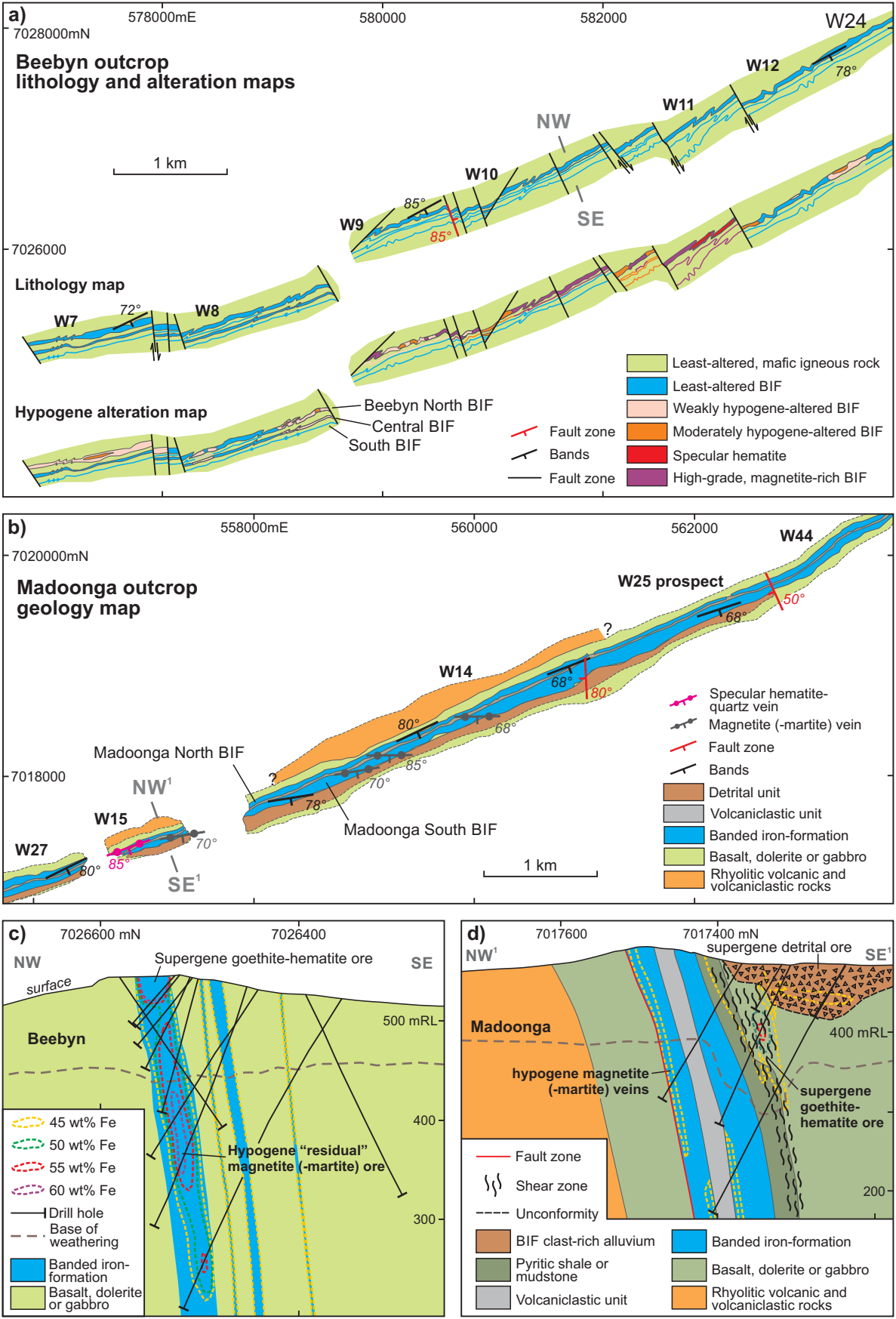
a)
578000mE
580000
582000
7028000mN
W24
Beebyn outcrop
lithology and alteration maps
W12
78°
W11
NW
1 km
W10
W9
85°
85°
SE
7026000
Lithology map
W7
72°
W8
Hypogene alteration map
Beebyn North BIF
Central BIF
South BIF
Fault zone
Bands
Fault zone
Least-altered, mafic igneous rock
Least-altered BIF
Weakly hypogene-altered BIF
Moderately hypogene-altered BIF
Specular hematite
High-grade, magnetite-rich BIF
b)
558000mE
560000
562000
7020000mN
W44
Madoonga outcrop
geology map
W25 prospect
50°
68°
?
W14
68°
80°
80°
68°
85°
70°
Madoonga North BIF
?
7018000
NW1
W15
78°
Madoonga South BIF
70°
85°
W27
80°
SE1
1 km
Specular hematite-quartz vein
Magnetite (-martite) vein
Fault zone
Bands
Detrital unit
Volcaniclastic unit
Banded iron-formation
Basalt, dolerite or gabbro
Rhyolitic volcanic and volcaniclastic rocks
c)
7026600 mN
7026400
NW
Supergene goethite-hematite ore
SE
surface
Beebyn
500 mRL
400
300
45 wt% Fe
50 wt% Fe
55 wt% Fe
60 wt% Fe
Drill hole
Base of weathering
Banded iron-formation
Basalt, dolerite or gabbro
Hypogene "residual" magnetite (-martite) ore
d)
7017600
7017400 mN
NW1
supergene detrital ore
SE1
Madoonga
400 mRL
hypogene magnetite (-martite) veins
supergene goethite-hematite ore
200
Fault zone
Shear zone
Unconformity
BIF clast-rich alluvium
Pyritic shale or mudstone
Volcaniclastic unit
Banded iron-formation
Basalt, dolerite or gabbro
Rhyolitic volcanic and volcaniclastic rocks

Beebyn North BIF — **Hypogene alteration** — **Supergene**

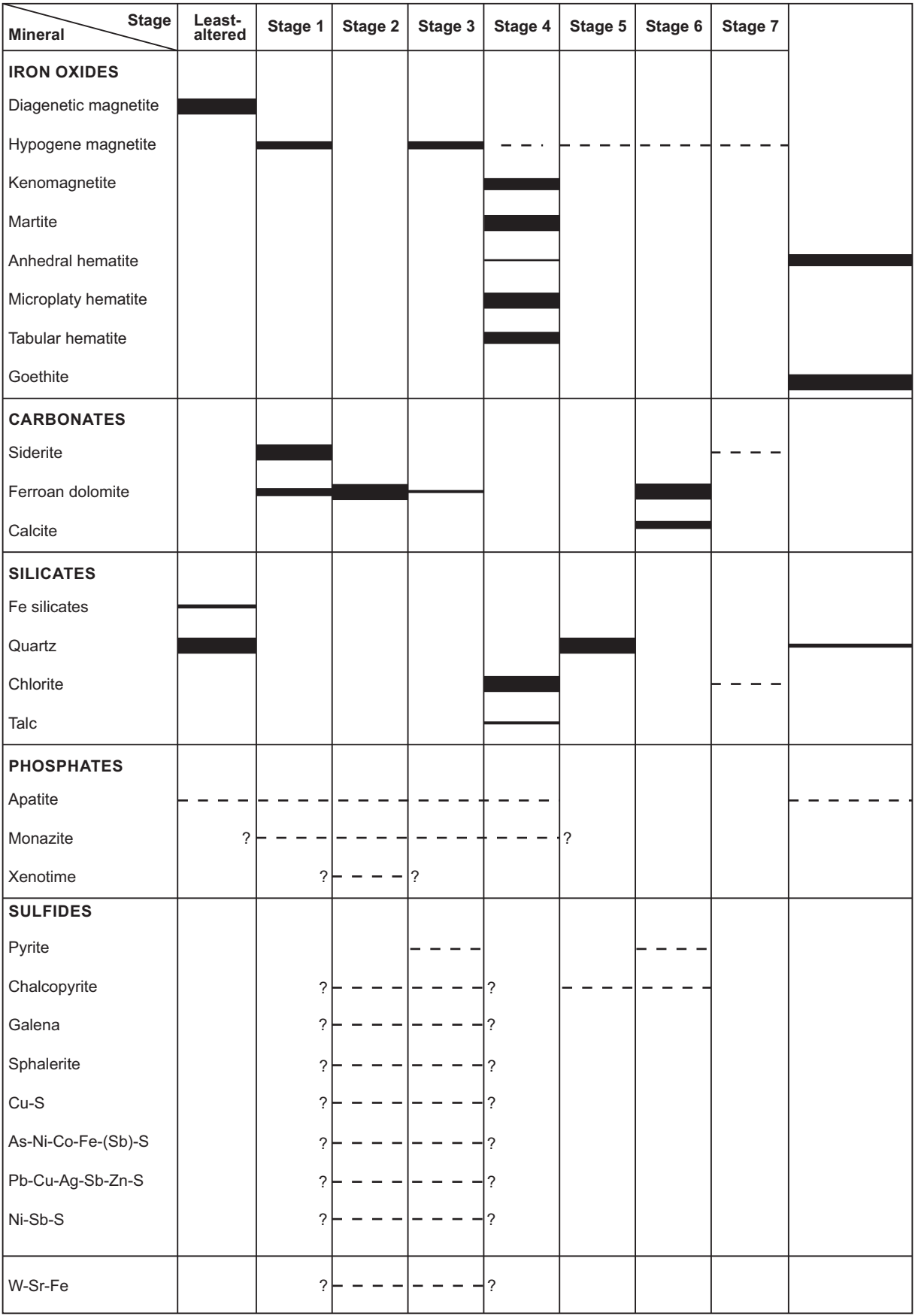

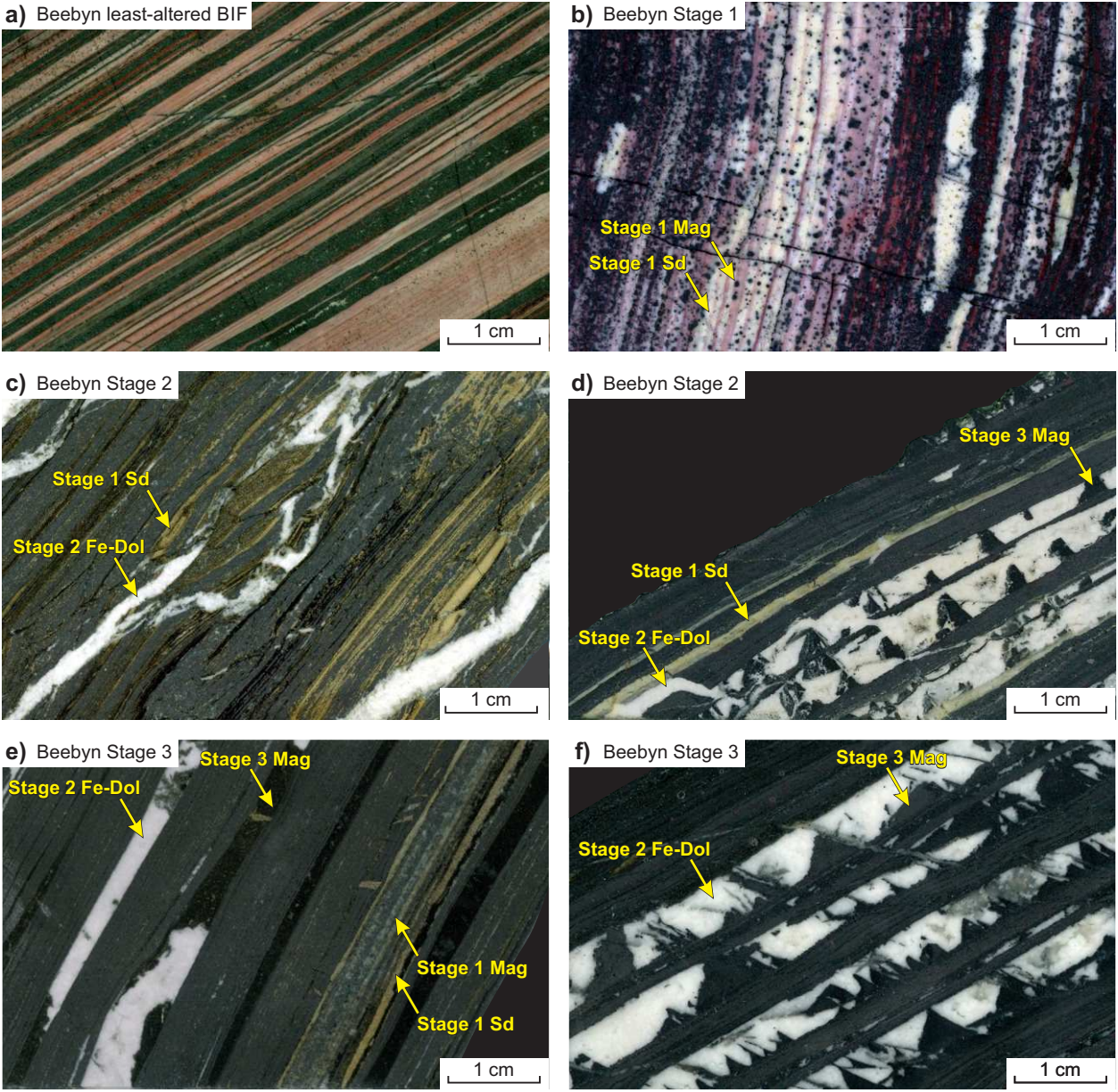
a) Beebyn least-altered BIF
1 cm
b) Beebyn Stage 1
Stage 1 Mag
Stage 1 Sd
1 cm
c) Beebyn Stage 2
Stage 1 Sd
Stage 2 Fe-Dol
1 cm
d) Beebyn Stage 2
Stage 3 Mag
Stage 1 Sd
Stage 2 Fe-Dol
1 cm
e) Beebyn Stage 3
Stage 3 Mag
Stage 2 Fe-Dol
Stage 1 Mag
Stage 1 Sd
1 cm
f) Beebyn Stage 3
Stage 3 Mag
Stage 2 Fe-Dol
1 cm

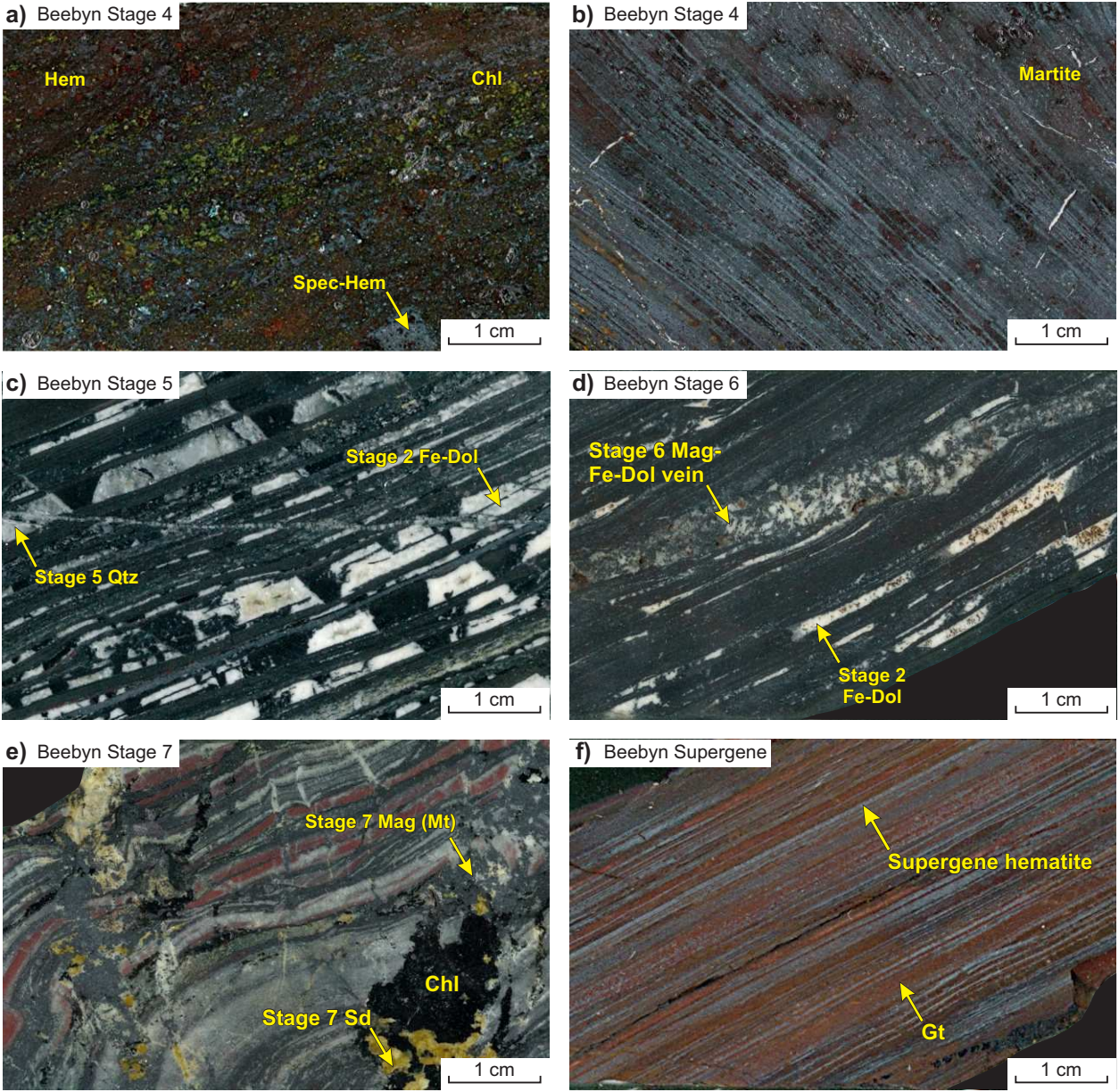
a) Beebyn Stage 4
Hem
Chl
Spec-Hem
1 cm
b) Beebyn Stage 4
Martite
1 cm
c) Beebyn Stage 5
Stage 2 Fe-Dol
Stage 5 Qtz
1 cm
d) Beebyn Stage 6
Stage 6 Mag-Fe-Dol vein
Stage 2 Fe-Dol
1 cm
e) Beebyn Stage 7
Stage 7 Mag (Mt)
Chl
Stage 7 Sd
1 cm
f) Beebyn Supergene
Supergene hematite
Gt
1 cm

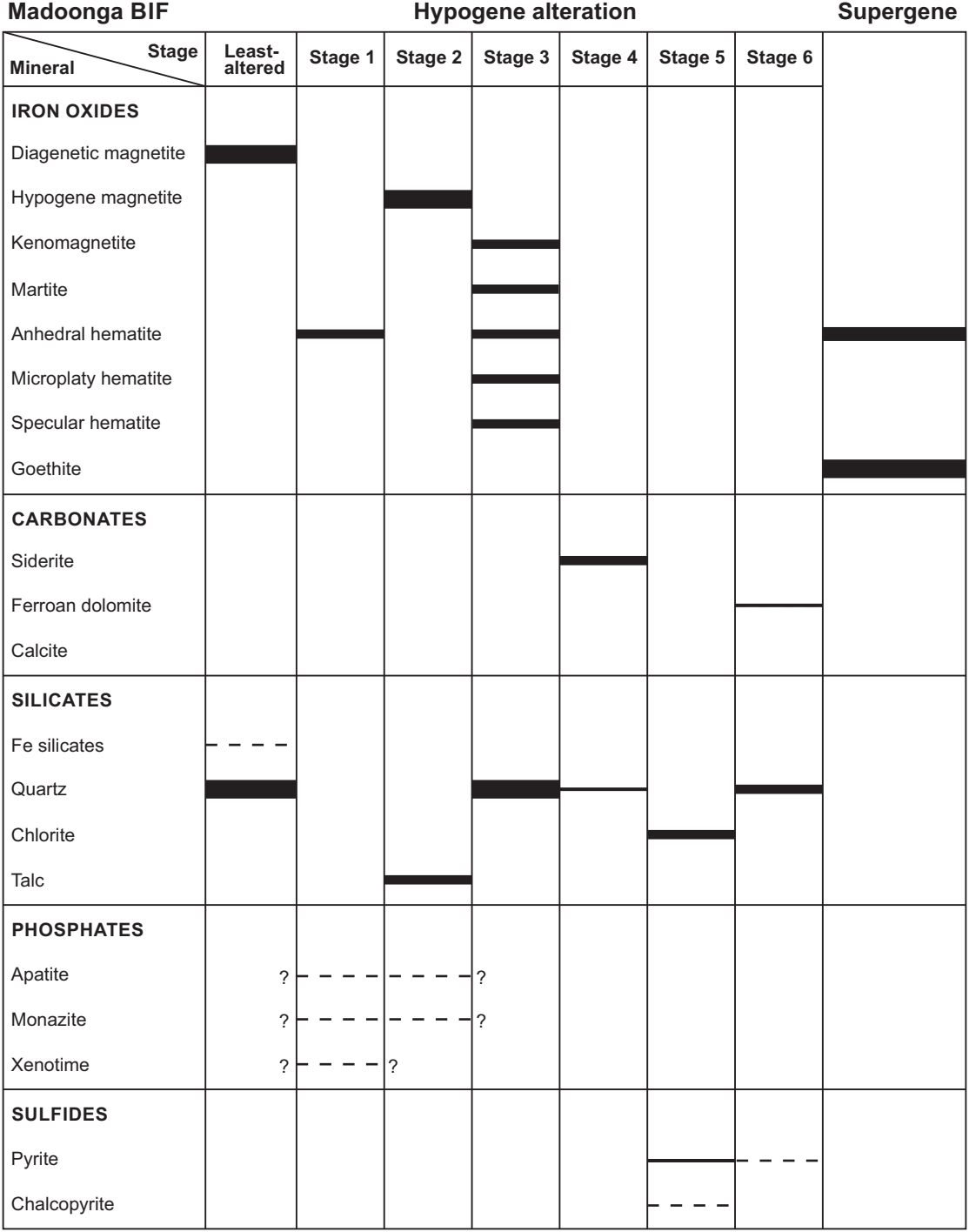
Madoonga BIF
Hypogene alteration
Supergene
Stage
Mineral
Least-altered
Stage 1
Stage 2
Stage 3
Stage 4
Stage 5
Stage 6
IRON OXIDES
Diagenetic magnetite
Hypogene magnetite
Kenomagnetite
Martite
Anhedral hematite
Microplaty hematite
Specular hematite
Goethite
CARBONATES
Siderite
Ferroan dolomite
Calcite
SILICATES
Fe silicates
Quartz
Chlorite
Talc
PHOSPHATES
Apatite
Monazite
Xenotime
SULFIDES
Pyrite
Chalcopyrite

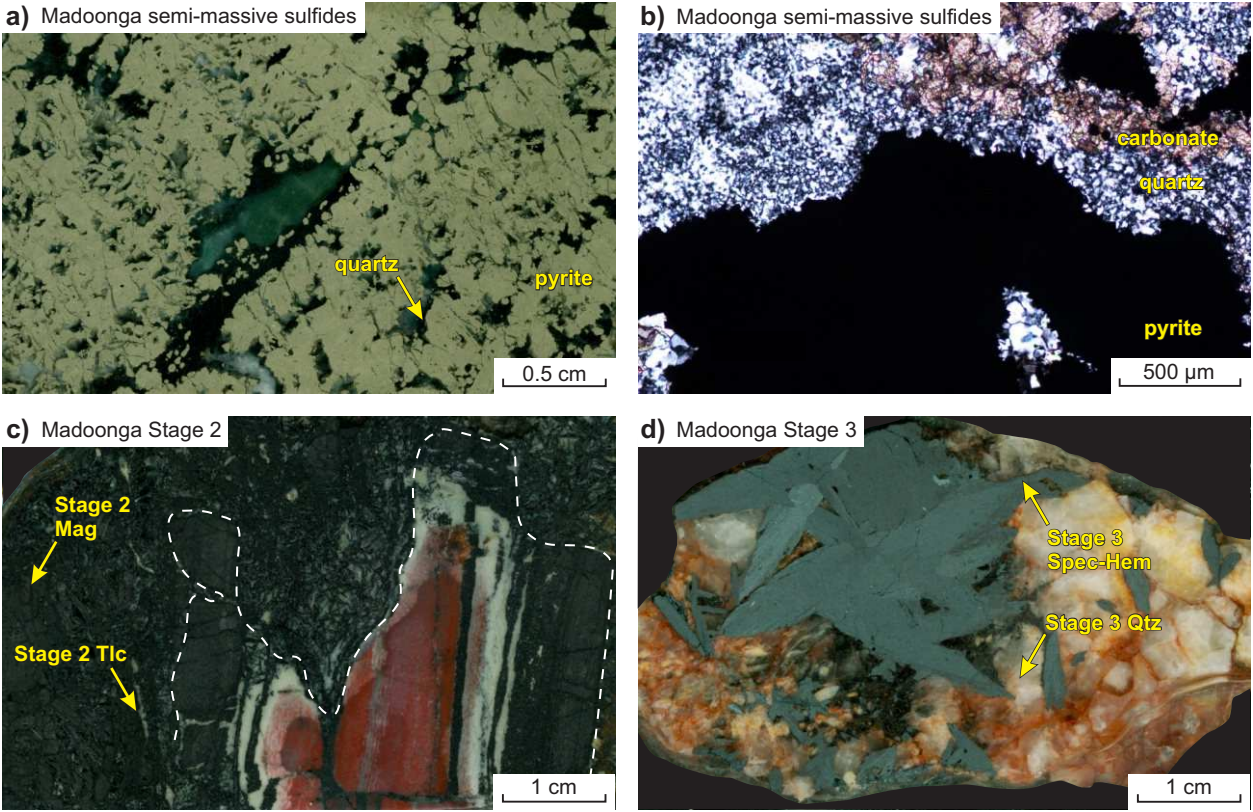
a) Madoonga semi-massive sulfides
quartz
pyrite
0.5 cm
b) Madoonga semi-massive sulfides
carbonate
quartz
pyrite
500 µm
c) Madoonga Stage 2
Stage 2 Mag
Stage 2 Tlc
1 cm
d) Madoonga Stage 3
Stage 3 Spec-Hem
Stage 3 Qtz
1 cm

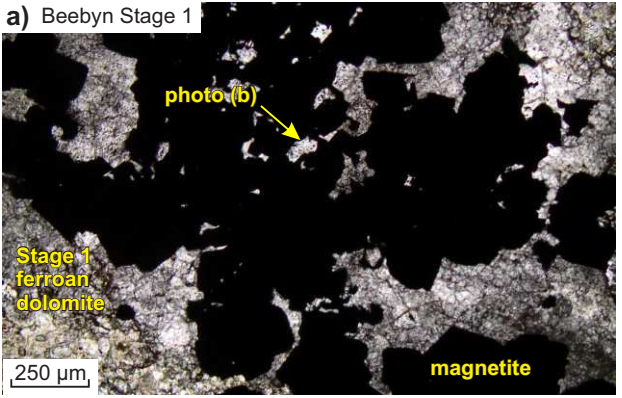
a) Beebyn Stage 1
photo (b)
Stage 1 ferroan dolomite
magnetite
250 µm

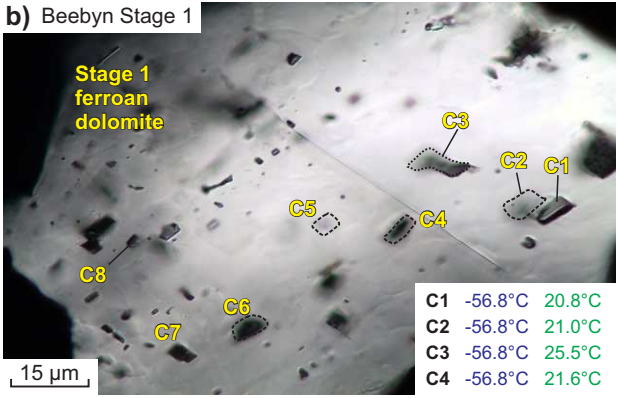
b) Beebyn Stage 1
Stage 1 ferroan dolomite
C1
C2
C3
C4
C5
C6
C7
C8
15 µm
C1 -56.8°C 20.8°C
C2 -56.8°C 21.0°C
C3 -56.8°C 25.5°C
C4 -56.8°C 21.6°C

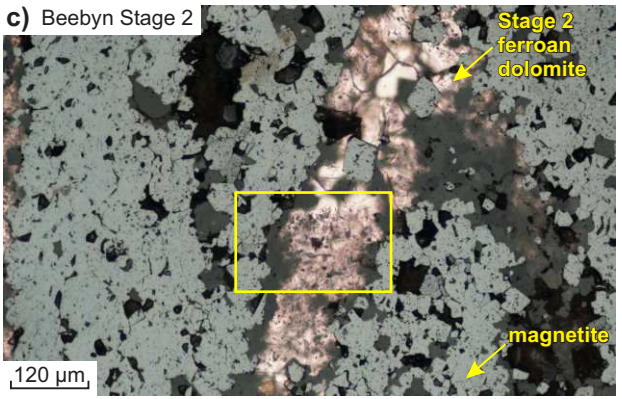
c) Beebyn Stage 2
Stage 2 ferroan dolomite
magnetite
120 µm

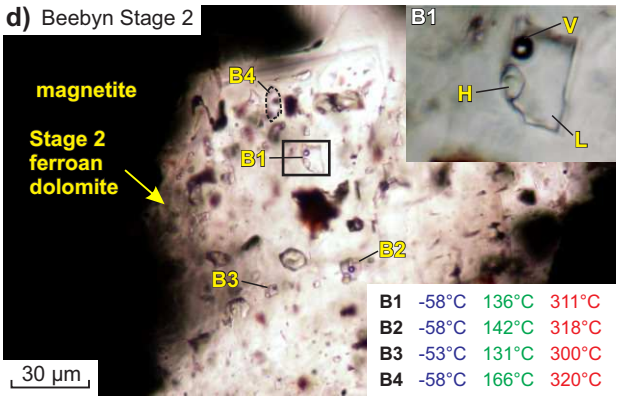
d) Beebyn Stage 2
magnetite
Stage 2 ferroan dolomite
B1
B2
B3
B4
V
H
L
30 µm
B1 -58°C 136°C 311°C
B2 -58°C 142°C 318°C
B3 -53°C 131°C 300°C
B4 -58°C 166°C 320°C

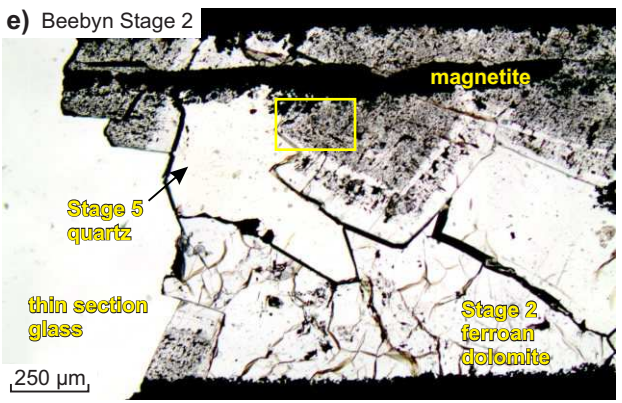
e) Beebyn Stage 2
magnetite
Stage 5 quartz
thin section glass
Stage 2 ferroan dolomite
250 µm

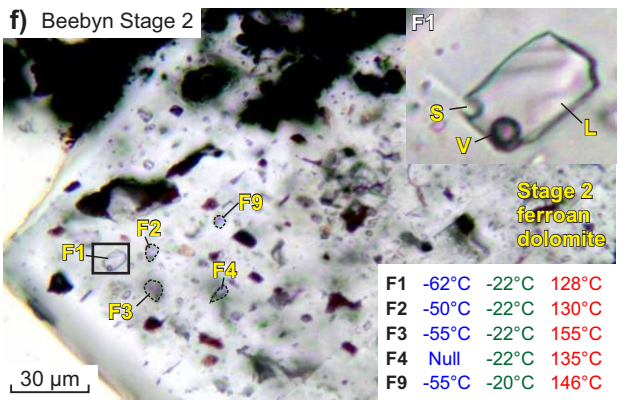
f) Beebyn Stage 2
F1
F2
F3
F4
F9
S
V
L
Stage 2 ferroan dolomite
30 µm
F1 -62°C -22°C 128°C
F2 -50°C -22°C 130°C
F3 -55°C -22°C 155°C
F4 Null -22°C 135°C
F9 -55°C -20°C 146°C

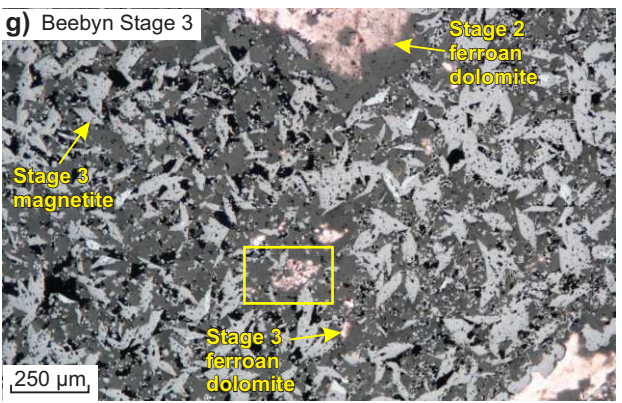
g) Beebyn Stage 3
Stage 2 ferroan dolomite
Stage 3 magnetite
Stage 3 ferroan dolomite
250 µm

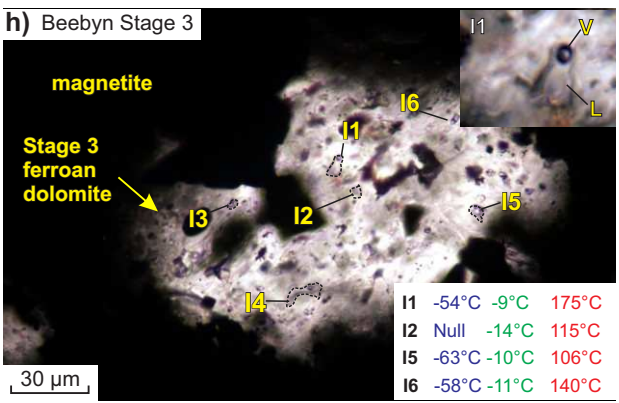
h) Beebyn Stage 3
magnetite
Stage 3 ferroan dolomite
I1
I2
I3
I4
I5
I6
V
L
30 µm
I1 -54°C -9°C 175°C
I2 Null -14°C 115°C
I5 -63°C -10°C 106°C
I6 -58°C -11°C 140°C

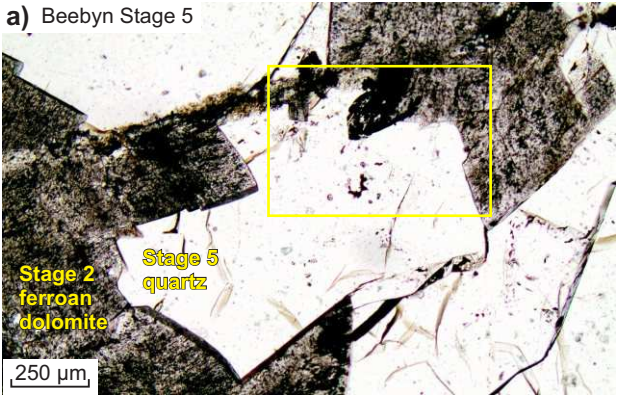
a) Beebyn Stage 5
Stage 2 ferroan dolomite
Stage 5 quartz
250 µm

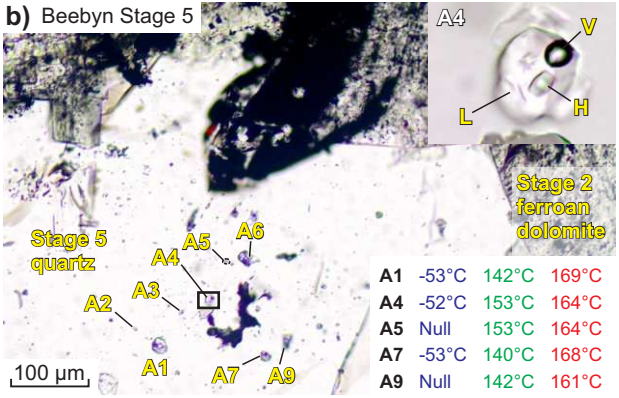
b) Beebyn Stage 5
A4
V
L
H
Stage 2 ferroan dolomite
Stage 5 quartz
A6
A5
A4
A3
A2
A1
A7
A9
100 µm
A1 -53°C 142°C 169°C
A4 -52°C 153°C 164°C
A5 Null 153°C 164°C
A7 -53°C 140°C 168°C
A9 Null 142°C 161°C

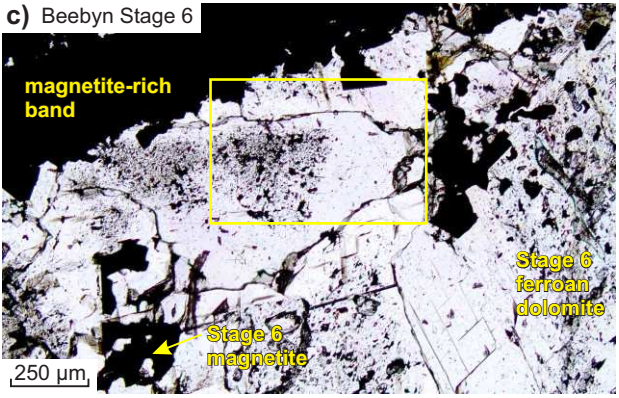
c) Beebyn Stage 6
magnetite-rich band
Stage 6 ferroan dolomite
Stage 6 magnetite
250 µm

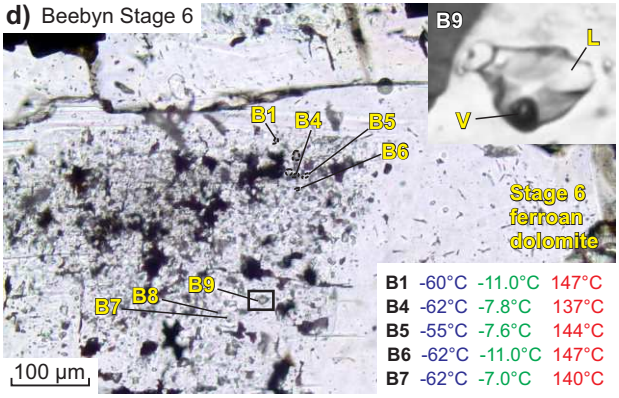
d) Beebyn Stage 6
B9
L
V
B1
B4
B5
B6
Stage 6 ferroan dolomite
B7
B8
B9
100 µm
B1 -60°C -11.0°C 147°C
B4 -62°C -7.8°C 137°C
B5 -55°C -7.6°C 144°C
B6 -62°C -11.0°C 147°C
B7 -62°C -7.0°C 140°C

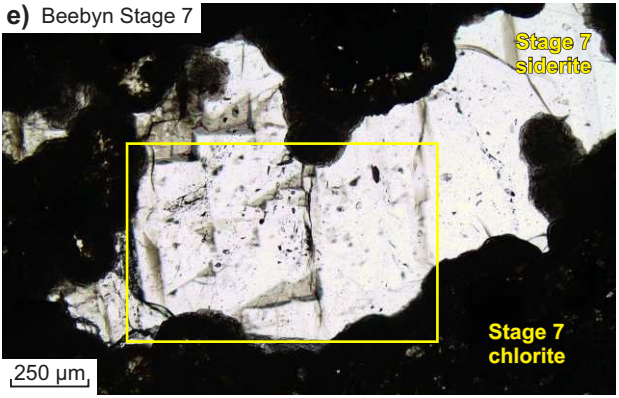
e) Beebyn Stage 7
Stage 7 siderite
Stage 7 chlorite
250 µm

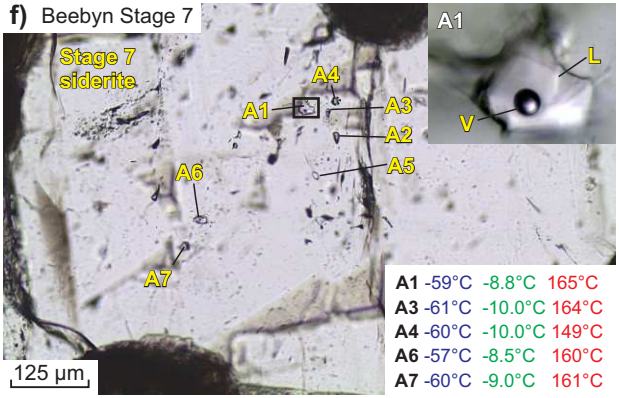
f) Beebyn Stage 7
A1
L
V
Stage 7 siderite
A4
A1
A3
A2
A5
A6
A7
125 µm
A1 -59°C -8.8°C 165°C
A3 -61°C -10.0°C 164°C
A4 -60°C -10.0°C 149°C
A6 -57°C -8.5°C 160°C
A7 -60°C -9.0°C 161°C

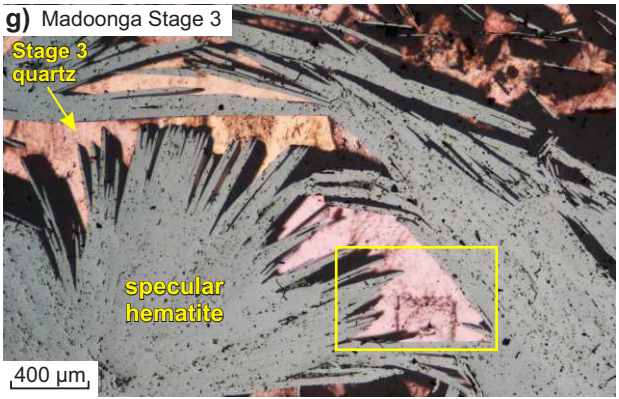
g) Madoonga Stage 3
Stage 3 quartz
specular hematite
400 µm

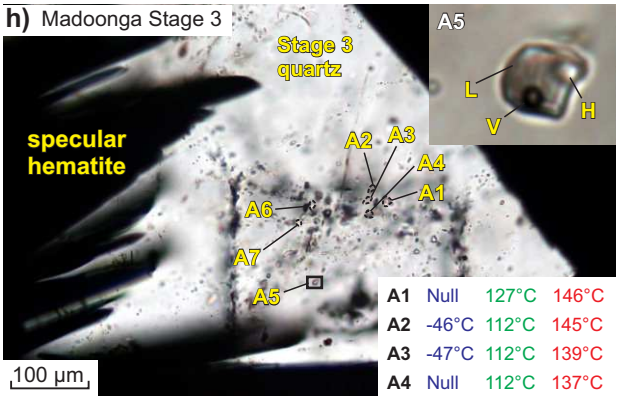
h) Madoonga Stage 3
A5
L
V
H
Stage 3 quartz
specular hematite
A2
A3
A4
A1
A6
A7
A5
100 µm
A1 Null 127°C 146°C
A2 -46°C 112°C 145°C
A3 -47°C 112°C 139°C
A4 Null 112°C 137°C

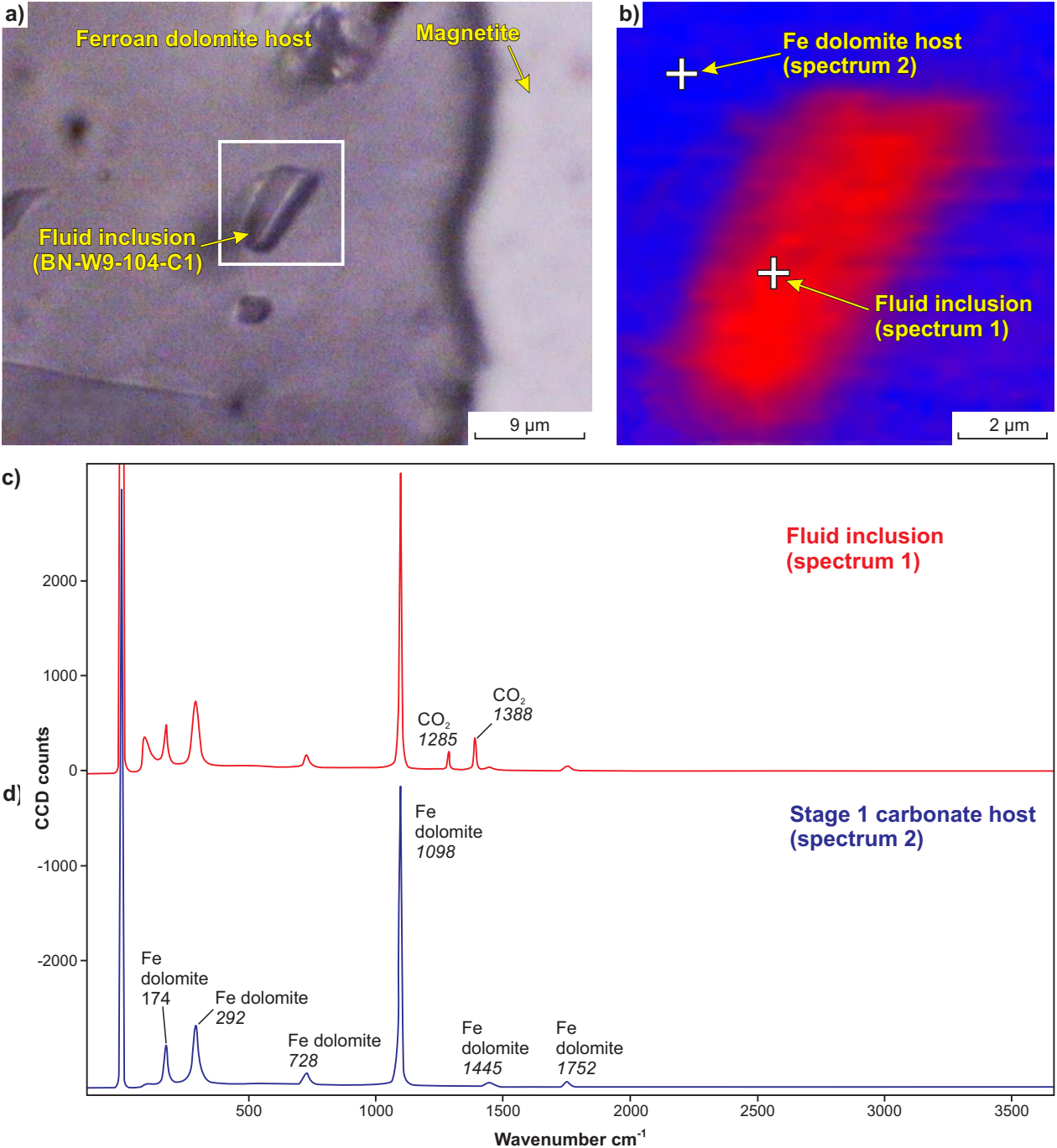
a)
Ferroan dolomite host
Magnetite
Fluid inclusion
(BN-W9-104-C1)
9 µm
b)
Fe dolomite host
(spectrum 2)
Fluid inclusion
(spectrum 1)
2 µm
c)
Fluid inclusion
(spectrum 1)
CO2
1285
CO2
1388
d)
Stage 1 carbonate host
(spectrum 2)
Fe
dolomite
1098
Fe
dolomite
174
Fe dolomite
292
Fe dolomite
728
Fe
dolomite
1445
Fe
dolomite
1752
CCD counts
2000
1000
0
-1000
-2000
500
1000
1500
2000
2500
3000
3500
Wavenumber cm-1

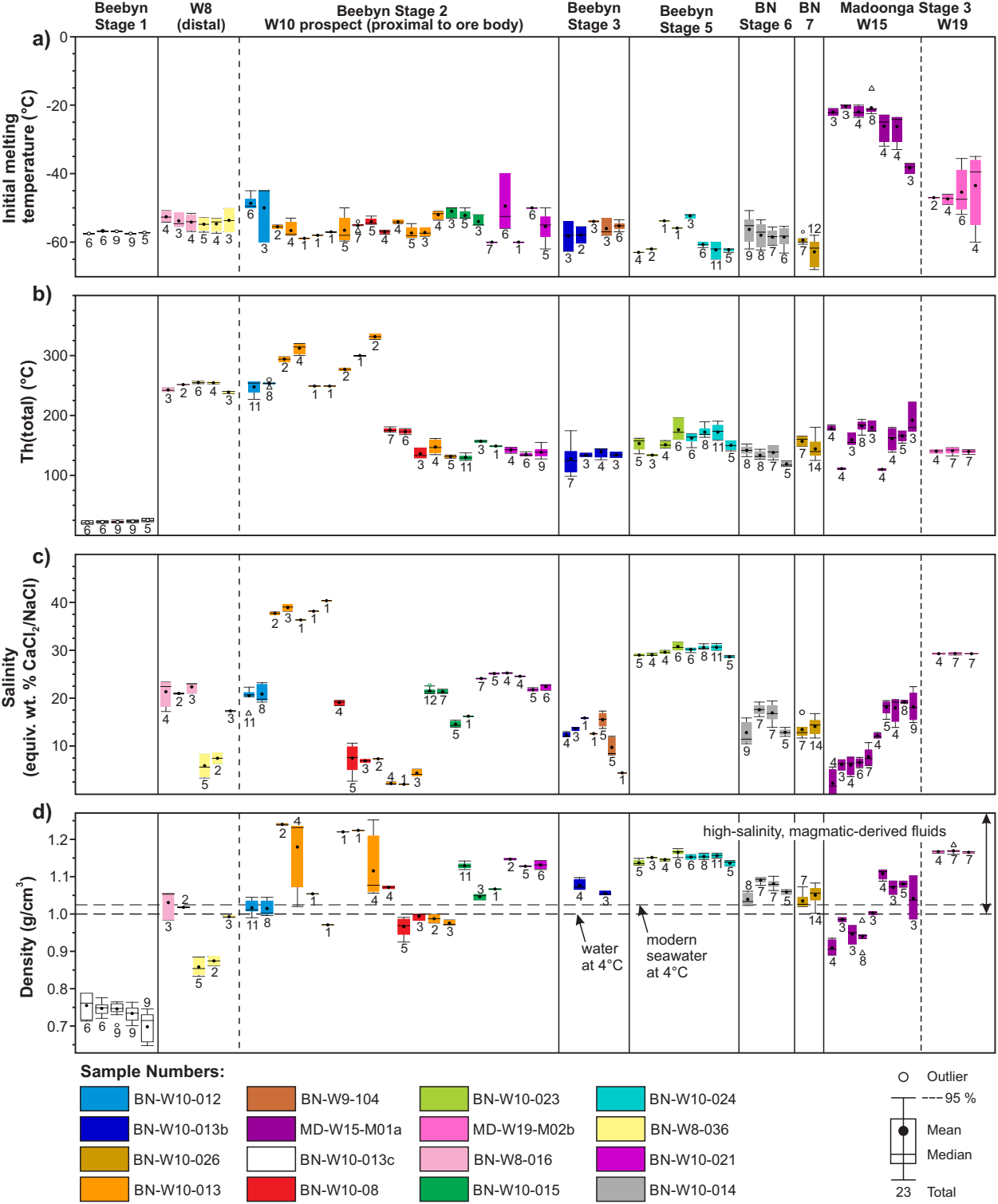
Beebyn Stage 1
W8 (distal)
Beebyn Stage 2
W10 prospect (proximal to ore body)
Beebyn Stage 3
Beebyn Stage 5
BN Stage 6
BN 7
Madoonga Stage 3
W15
W19
a)
Initial melting temperature (°C)
b)
Th(total) (°C)
c)
Salinity (equiv. wt. % CaCl2/NaCl)
d)
Density (g/cm3)
high-salinity, magmatic-derived fluids
water at 4°C
modern seawater at 4°C
Sample Numbers:
BN-W10-012
BN-W9-104
BN-W10-023
BN-W10-024
BN-W10-013b
MD-W15-M01a
MD-W19-M02b
BN-W8-036
BN-W10-026
BN-W10-013c
BN-W8-016
BN-W10-021
BN-W10-013
BN-W10-08
BN-W10-015
BN-W10-014
Outlier
95 %
Mean
Median
Total

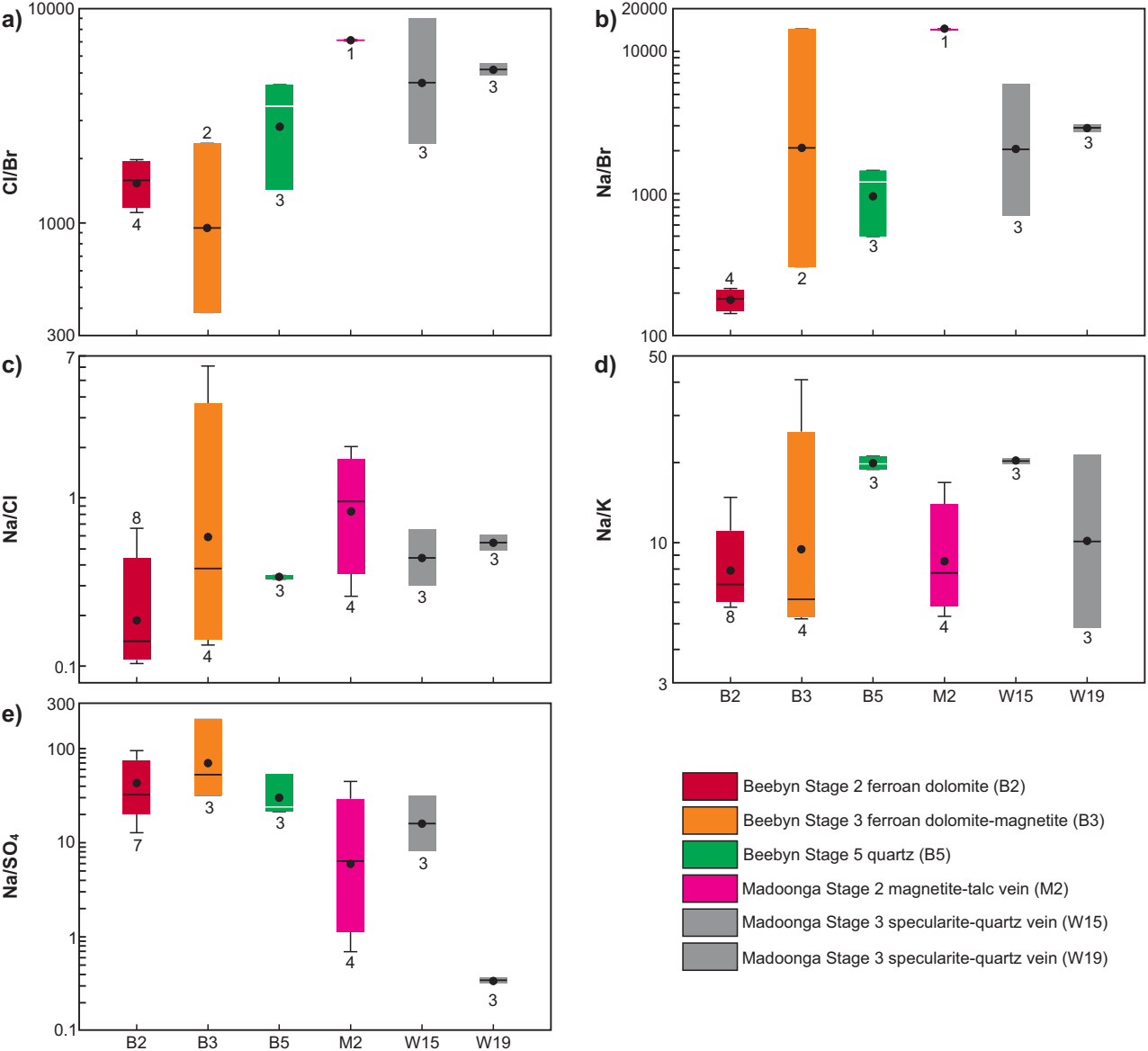
a)
Cl/Br
10000
1000
300
b)
Na/Br
20000
10000
1000
100
c)
Na/Cl
7
1
0.1
d)
Na/K
50
10
3
e)
Na/SO4
300
100
10
1
0.1
B2
B3
B5
M2
W15
W19
Beebyn Stage 2 ferroan dolomite (B2)
Beebyn Stage 3 ferroan dolomite-magnetite (B3)
Beebyn Stage 5 quartz (B5)
Madoonga Stage 2 magnetite-talc vein (M2)
Madoonga Stage 3 specularite-quartz vein (W15)
Madoonga Stage 3 specularite-quartz vein (W19)

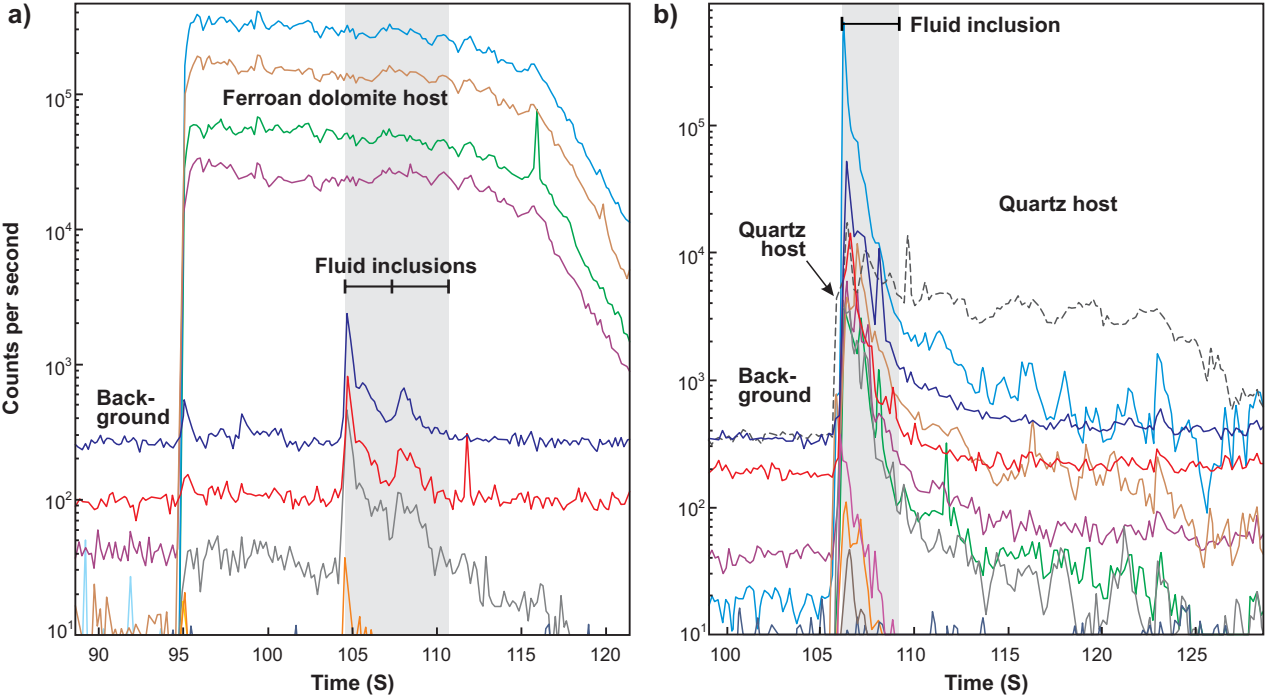
a)
Ferroan dolomite host
Fluid inclusions
Back-
ground
Counts per second
Time (S)
b)
Fluid inclusion
Quartz host
Quartz
host
Back-
ground
Time (S)
Na
Si
Ca
Fe
Zn
Ba
Pb
Mg
K
Mn
Cu
Sr
W

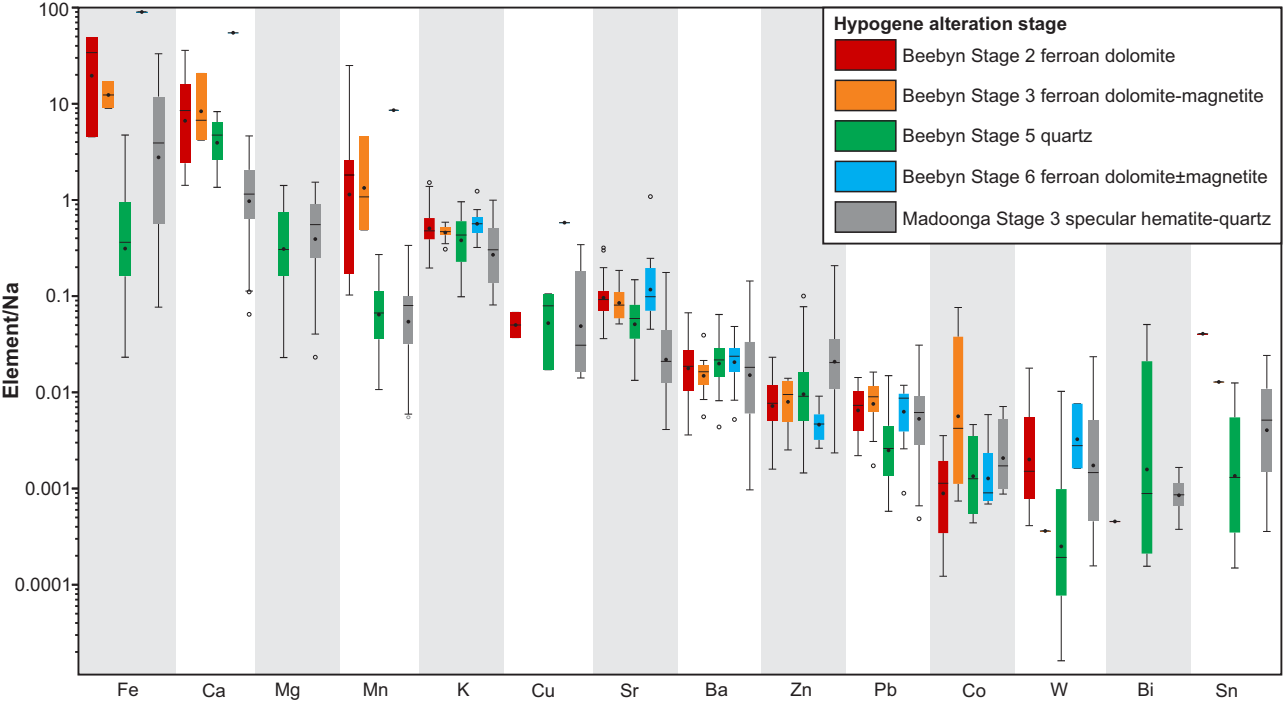
Hypogene alteration stage
Beebyn Stage 2 ferroan dolomite
Beebyn Stage 3 ferroan dolomite-magnetite
Beebyn Stage 5 quartz
Beebyn Stage 6 ferroan dolomite±magnetite
Madoonga Stage 3 specular hematite-quartz
Element/Na
100
10
1
0.1
0.01
0.001
0.0001
Fe
Ca
Mg
Mn
K
Cu
Sr
Ba
Zn
Pb
Co
W
Bi
Sn

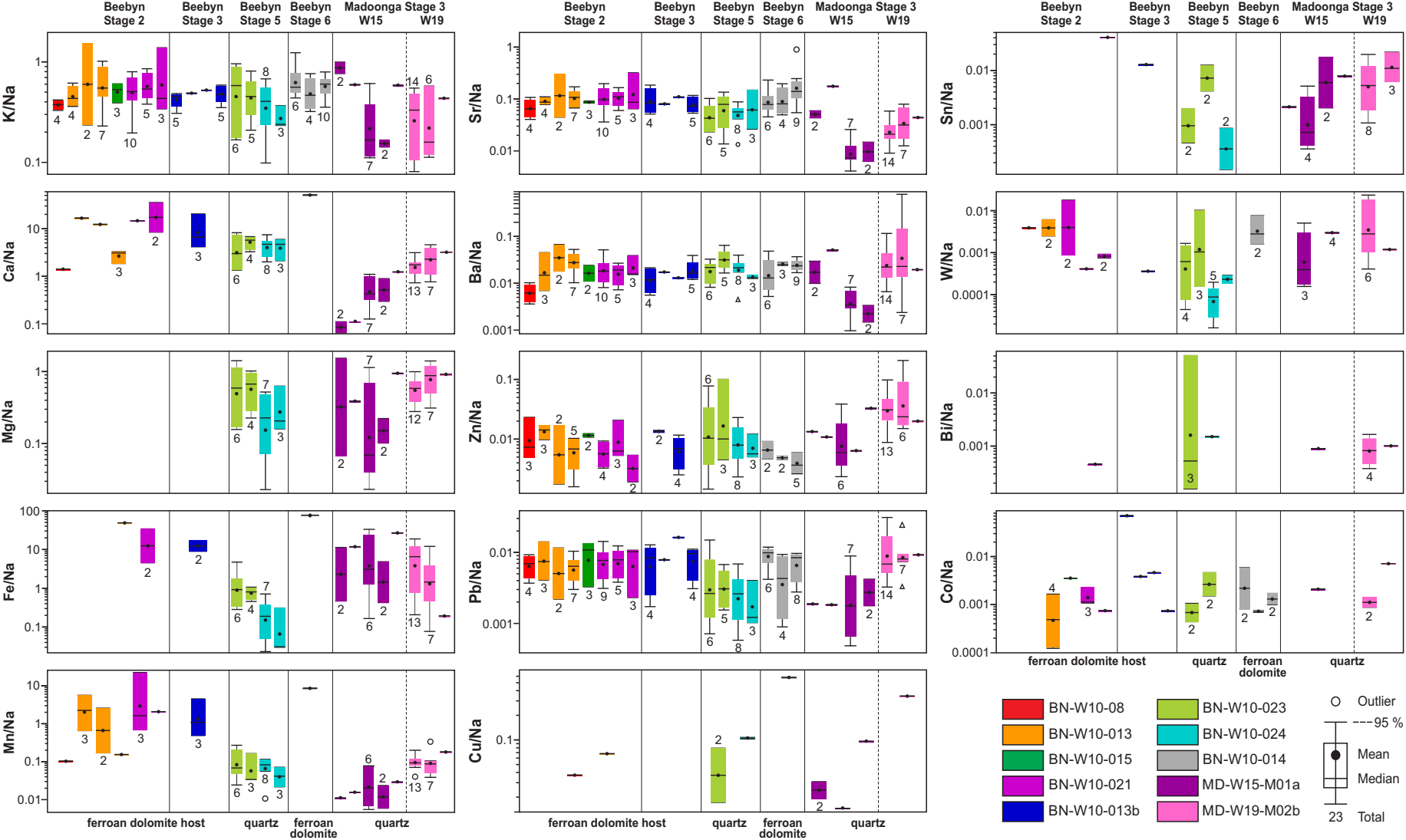
Beebyn Stage 2
Beebyn Stage 3
Beebyn Stage 5
Beebyn Stage 6
Madoonga W15
Madoonga Stage 3 W19
K/Na
Sr/Na
Sn/Na
Ca/Na
Ba/Na
W/Na
Mg/Na
Zn/Na
Bi/Na
Fe/Na
Pb/Na
Co/Na
Mn/Na
Cu/Na
ferroan dolomite host
quartz
ferroan dolomite
quartz
BN-W10-08
BN-W10-013
BN-W10-015
BN-W10-021
BN-W10-013b
BN-W10-023
BN-W10-024
BN-W10-014
MD-W15-M01a
MD-W19-M02b
Outlier
95 %
Mean
Median
Total

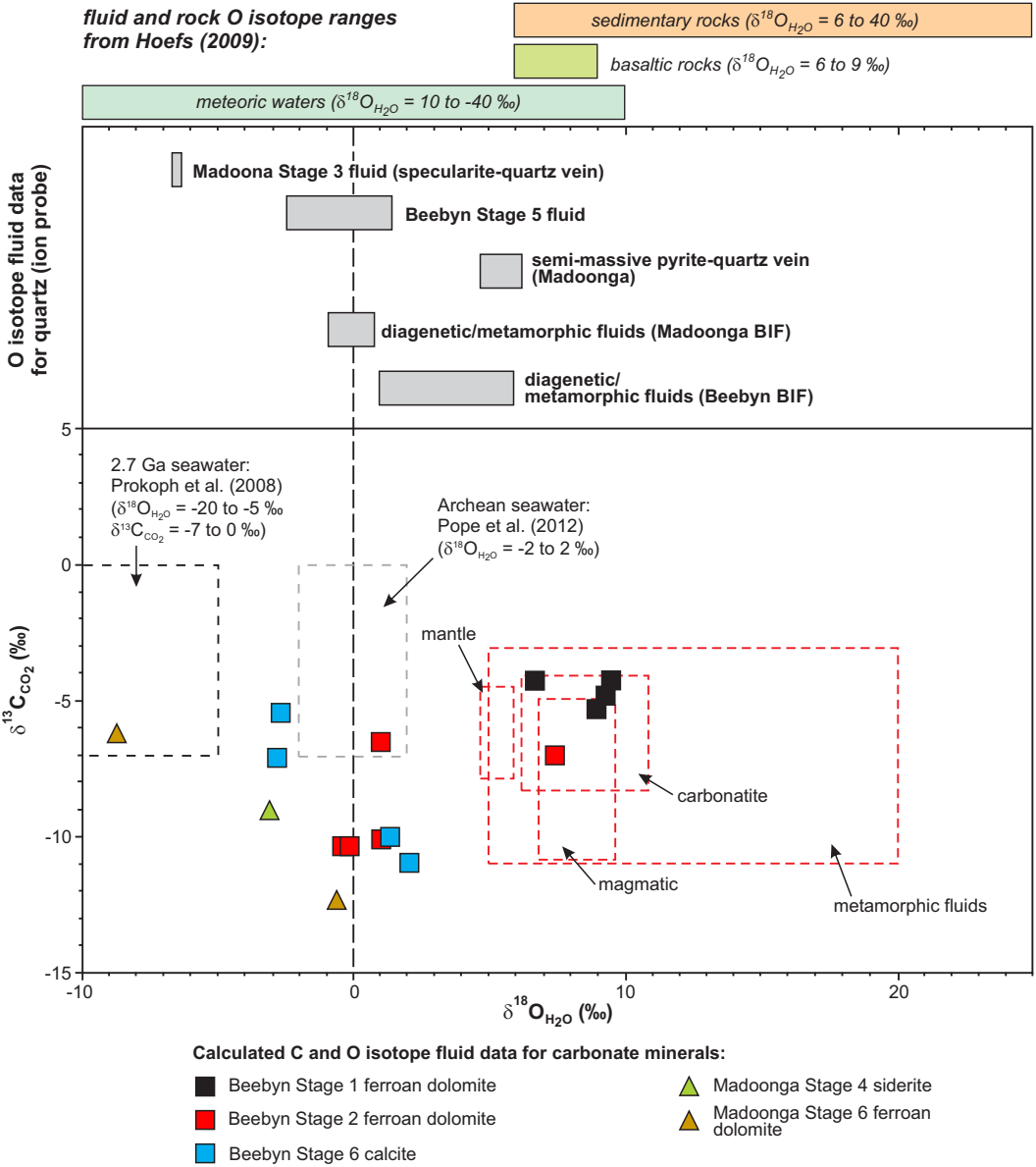
fluid and rock O isotope ranges from Hoefs (2009):
sedimentary rocks ($\delta^{18}O_{H_2O}$ = 6 to 40 ‰)
basaltic rocks ($\delta^{18}O_{H_2O}$ = 6 to 9 ‰)
meteoric waters ($\delta^{18}O_{H_2O}$ = 10 to -40 ‰)
O isotope fluid data for quartz (ion probe)
Madoona Stage 3 fluid (specularite-quartz vein)
Beebyn Stage 5 fluid
semi-massive pyrite-quartz vein (Madoonga)
diagenetic/metamorphic fluids (Madoonga BIF)
diagenetic/ metamorphic fluids (Beebyn BIF)
2.7 Ga seawater: Prokoph et al. (2008) ($\delta^{18}O_{H_2O}$ = -20 to -5 ‰ $\delta^{13}C_{CO_2}$ = -7 to 0 ‰)
Archean seawater: Pope et al. (2012) ($\delta^{18}O_{H_2O}$ = -2 to 2 ‰)
mantle
carbonatite
magmatic
metamorphic fluids
$\delta^{13}C_{CO_2}$ (‰)
$\delta^{18}O_{H_2O}$ (‰)
5
0
-5
-10
-15
-10
0
10
20
Calculated C and O isotope fluid data for carbonate minerals:
Beebyn Stage 1 ferroan dolomite
Beebyn Stage 2 ferroan dolomite
Beebyn Stage 6 calcite
Madoonga Stage 4 siderite
Madoonga Stage 6 ferroan dolomite

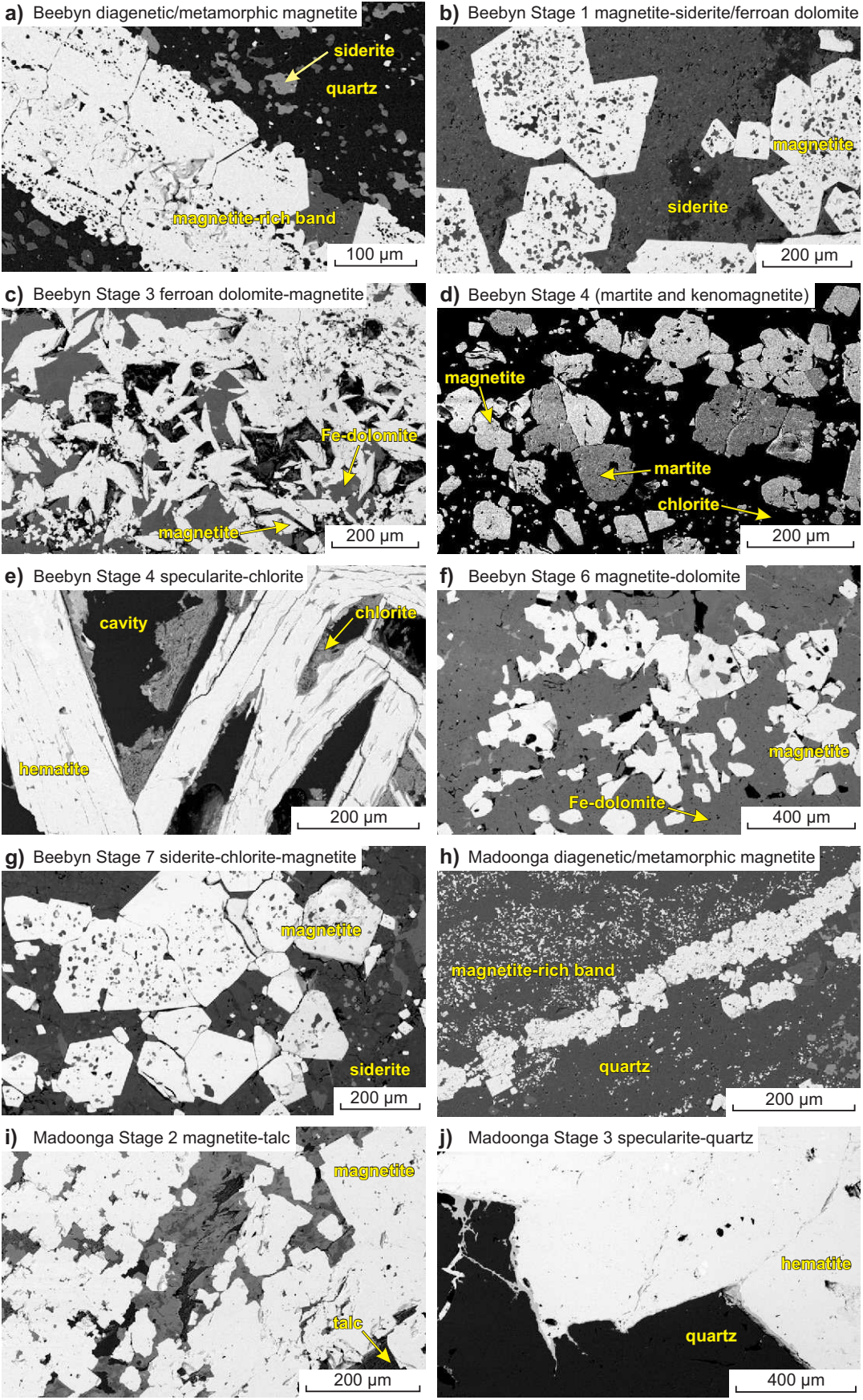
a) Beebyn diagenetic/metamorphic magnetite
siderite
quartz
magnetite-rich band
100 µm
b) Beebyn Stage 1 magnetite-siderite/ferroan dolomite
magnetite
siderite
200 µm
c) Beebyn Stage 3 ferroan dolomite-magnetite
Fe-dolomite
magnetite
200 µm
d) Beebyn Stage 4 (martite and kenomagnetite)
magnetite
martite
chlorite
200 µm
e) Beebyn Stage 4 specularite-chlorite
cavity
chlorite
hematite
200 µm
f) Beebyn Stage 6 magnetite-dolomite
magnetite
Fe-dolomite
400 µm
g) Beebyn Stage 7 siderite-chlorite-magnetite
magnetite
siderite
200 µm
h) Madoonga diagenetic/metamorphic magnetite
magnetite-rich band
quartz
200 µm
i) Madoonga Stage 2 magnetite-talc
magnetite
talc
200 µm
j) Madoonga Stage 3 specularite-quartz
hematite
quartz
400 µm

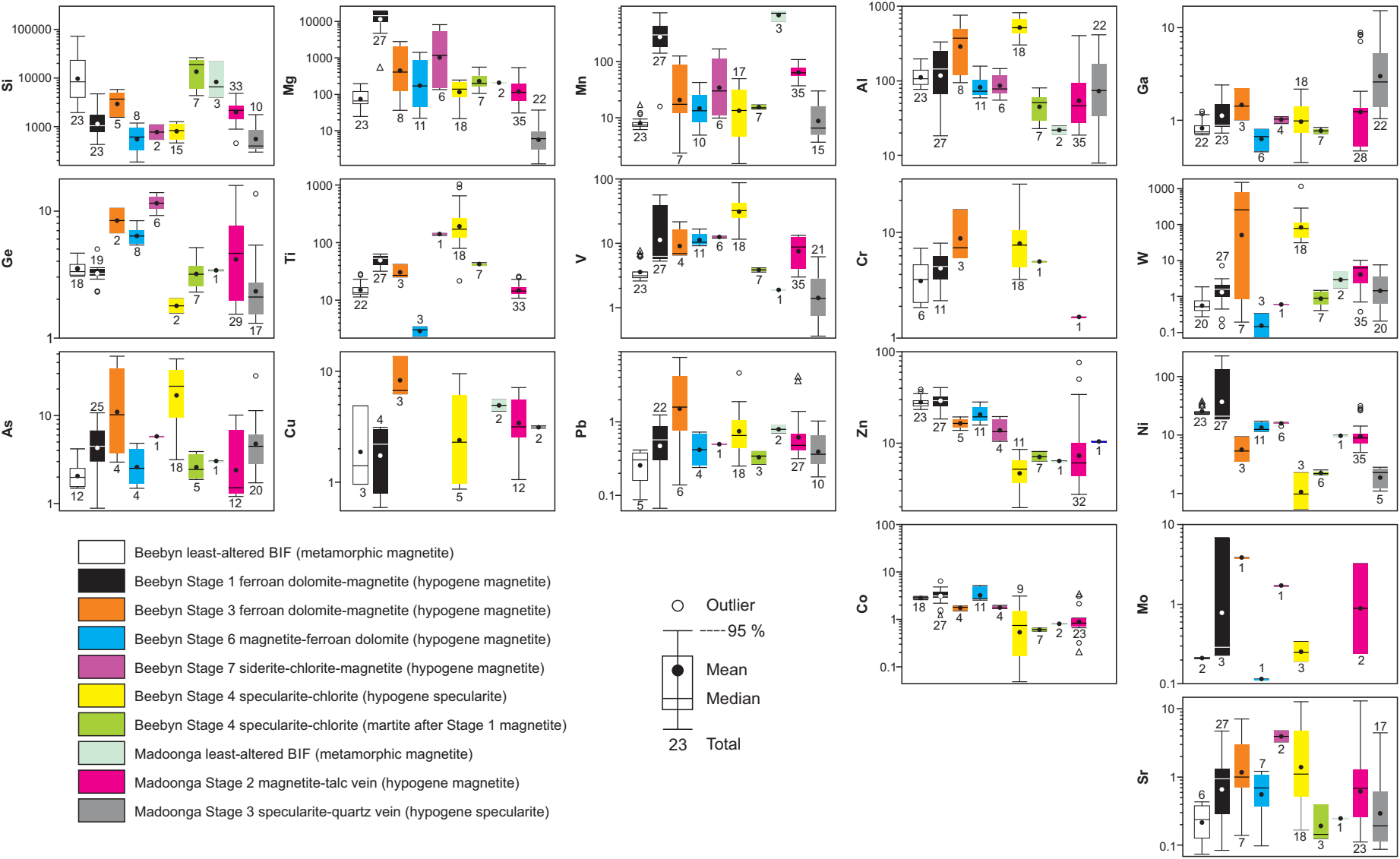
Si
Mg
Mn
Al
Ga
Ge
Ti
V
Cr
W
As
Cu
Pb
Zn
Ni
Co
Mo
Sr
Beebyn least-altered BIF (metamorphic magnetite)
Beebyn Stage 1 ferroan dolomite-magnetite (hypogene magnetite)
Beebyn Stage 3 ferroan dolomite-magnetite (hypogene magnetite)
Beebyn Stage 6 magnetite-ferroan dolomite (hypogene magnetite)
Beebyn Stage 7 siderite-chlorite-magnetite (hypogene magnetite)
Beebyn Stage 4 specularite-chlorite (hypogene specularite)
Beebyn Stage 4 specularite-chlorite (martite after Stage 1 magnetite)
Madoonga least-altered BIF (metamorphic magnetite)
Madoonga Stage 2 magnetite-talc vein (hypogene magnetite)
Madoonga Stage 3 specularite-quartz vein (hypogene specularite)
Outlier
95 %
Mean
Median
Total

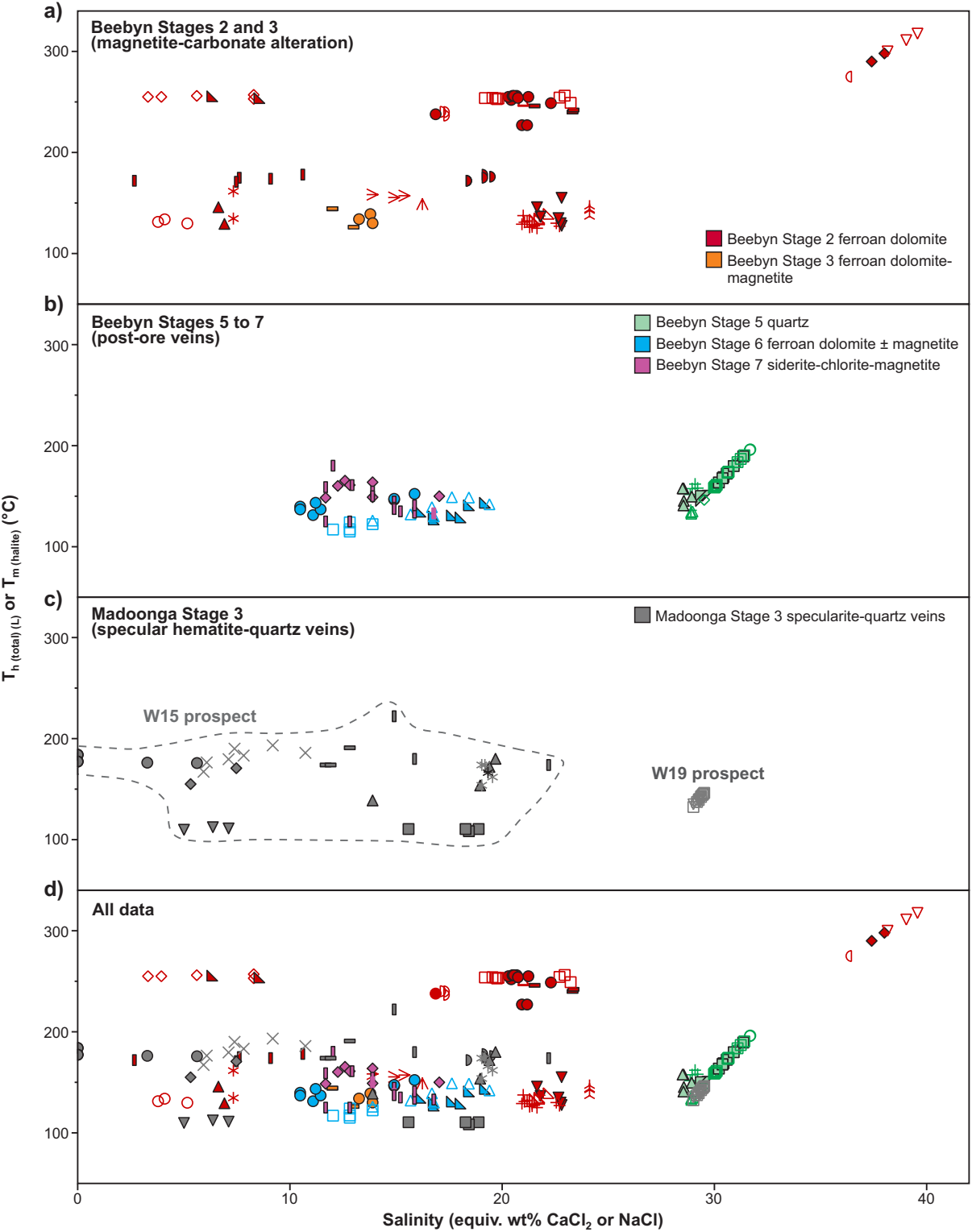
a)
Beebyn Stages 2 and 3
(magnetite-carbonate alteration)
Beebyn Stage 2 ferroan dolomite
Beebyn Stage 3 ferroan dolomite-magnetite
b)
Beebyn Stages 5 to 7
(post-ore veins)
Beebyn Stage 5 quartz
Beebyn Stage 6 ferroan dolomite ± magnetite
Beebyn Stage 7 siderite-chlorite-magnetite
c)
Madoonga Stage 3
(specular hematite-quartz veins)
Madoonga Stage 3 specularite-quartz veins
W15 prospect
W19 prospect
d)
All data
300
200
100
0
10
20
30
40
$T_{h\ (total)\ (L)}$ or $T_{m\ (halite)}$ (°C)
Salinity (equiv. wt% $CaCl_2$ or NaCl)

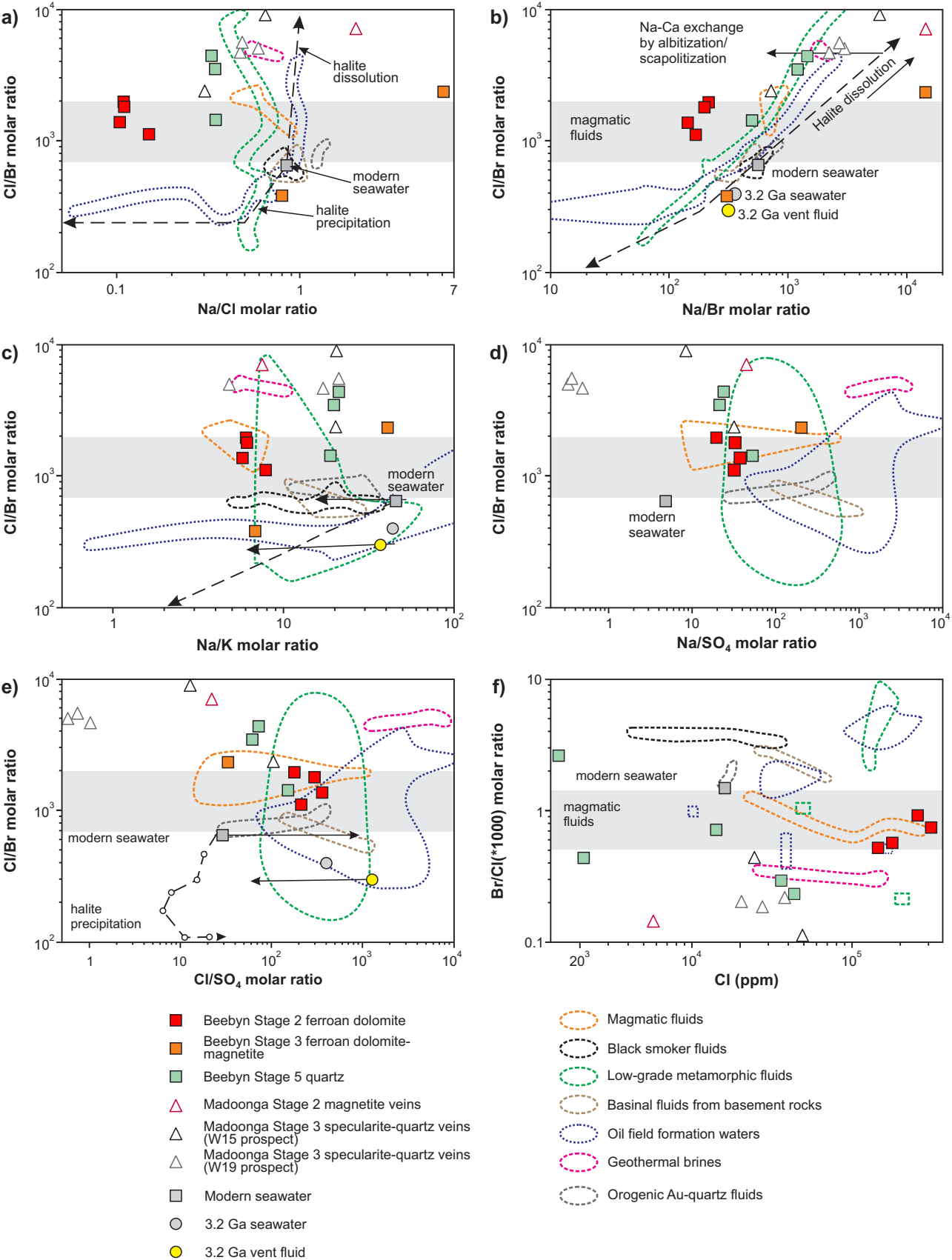
a)
Cl/Br molar ratio
Na/Cl molar ratio
halite dissolution
modern seawater
halite precipitation
b)
Na-Ca exchange by albitization/ scapolitization
magmatic fluids
Halite dissolution
modern seawater
3.2 Ga seawater
3.2 Ga vent fluid
Na/Br molar ratio
c)
modern seawater
Na/K molar ratio
d)
modern seawater
Na/SO4 molar ratio
e)
modern seawater
halite precipitation
Cl/SO4 molar ratio
f)
modern seawater
magmatic fluids
Br/Cl(*1000) molar ratio
Cl (ppm)
Beebyn Stage 2 ferroan dolomite
Beebyn Stage 3 ferroan dolomite-magnetite
Beebyn Stage 5 quartz
Madoonga Stage 2 magnetite veins
Madoonga Stage 3 specularite-quartz veins (W15 prospect)
Madoonga Stage 3 specularite-quartz veins (W19 prospect)
Modern seawater
3.2 Ga seawater
3.2 Ga vent fluid
Magmatic fluids
Black smoker fluids
Low-grade metamorphic fluids
Basinal fluids from basement rocks
Oil field formation waters
Geothermal brines
Orogenic Au-quartz fluids

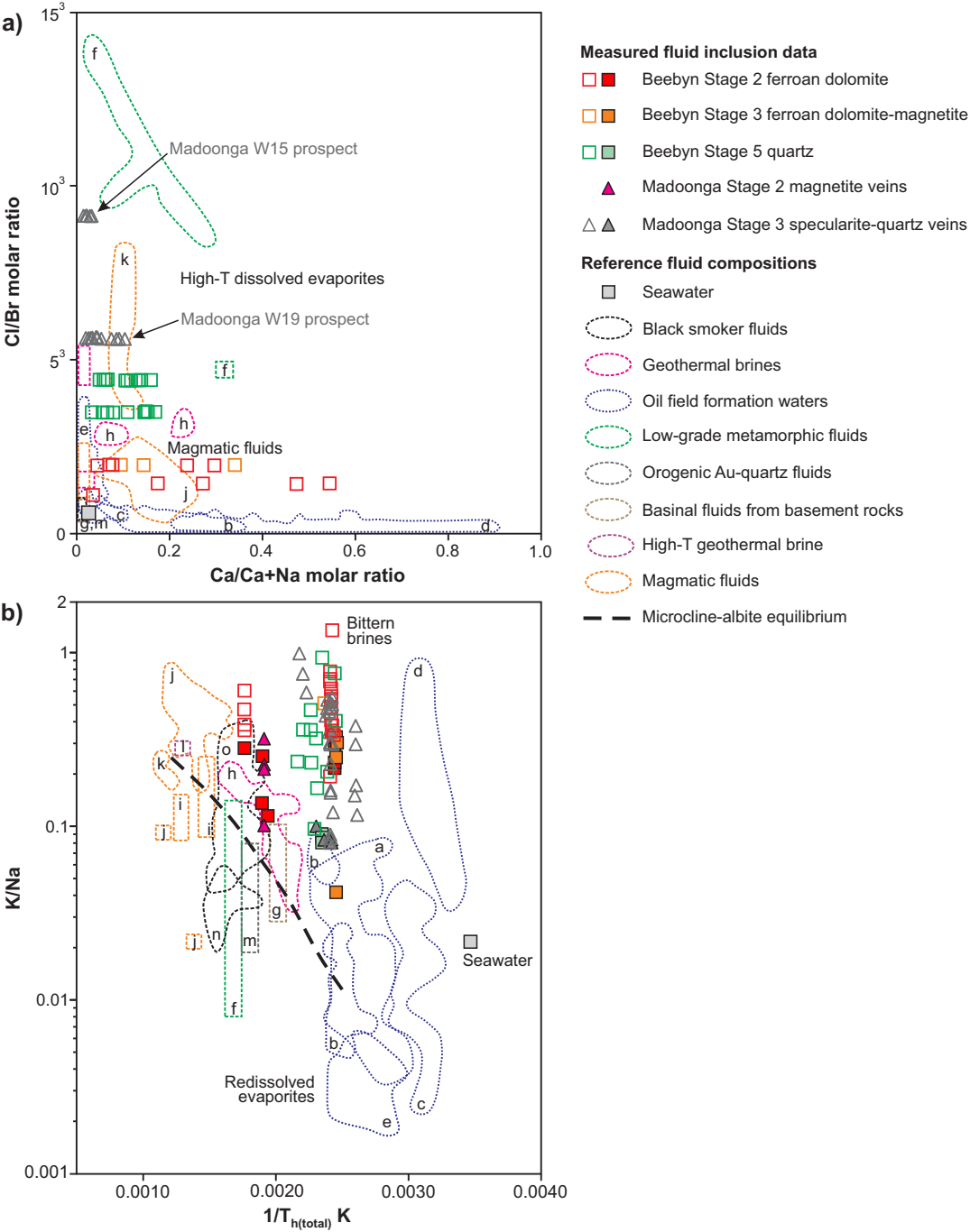
a)
Cl/Br molar ratio
Ca/Ca+Na molar ratio
Madoonga W15 prospect
Madoonga W19 prospect
High-T dissolved evaporites
Magmatic fluids
b)
K/Na
1/T h(total) K
Bittern brines
Seawater
Redissolved evaporites
Measured fluid inclusion data
Beebyn Stage 2 ferroan dolomite
Beebyn Stage 3 ferroan dolomite-magnetite
Beebyn Stage 5 quartz
Madoonga Stage 2 magnetite veins
Madoonga Stage 3 specularite-quartz veins
Reference fluid compositions
Seawater
Black smoker fluids
Geothermal brines
Oil field formation waters
Low-grade metamorphic fluids
Orogenic Au-quartz fluids
Basinal fluids from basement rocks
High-T geothermal brine
Magmatic fluids
Microcline-albite equilibrium

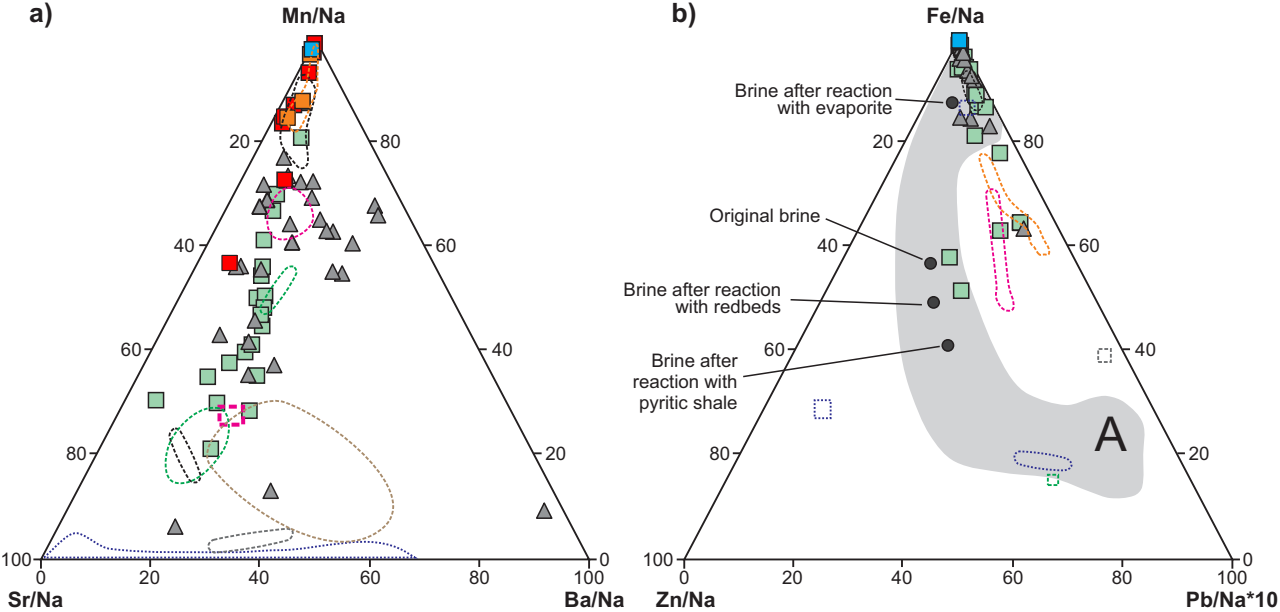

Beebyn Stage 2 ferroan dolomite

Beebyn Stage 3 ferroan dolomite-magnetite

Beebyn Stage 5 quartz

Beebyn Stage 6 ferroan dolomite and calcite veins

Madoonga Stage 3 specularite-quartz veins

Magmatic fluids

Black smoker fluids

Low-grade metamorphic fluids

Basinal fluids from basement rocks

Oil field formation waters

Geothermal brines

Orogenic Au-quartz fluids

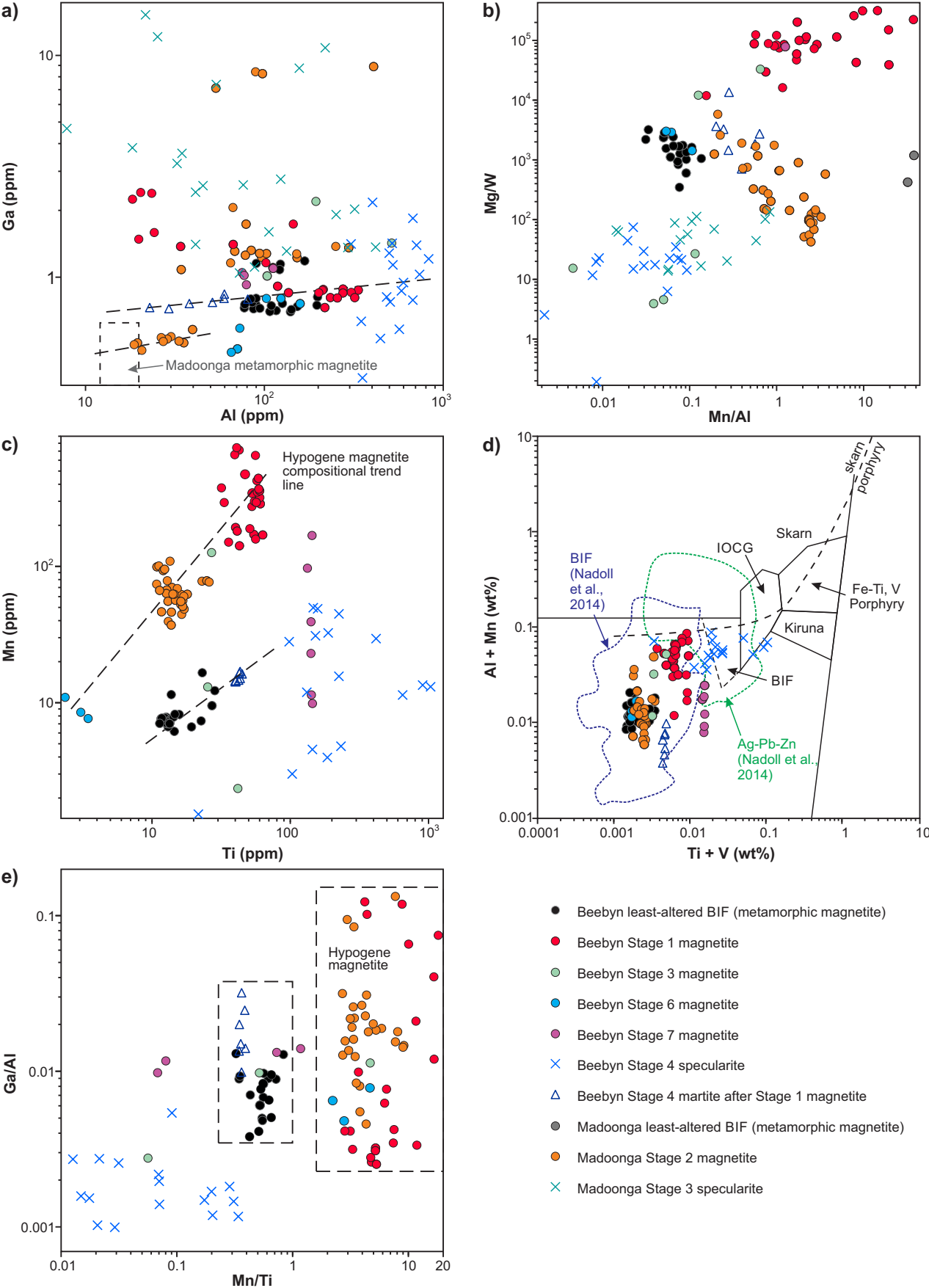
a)
Ga (ppm)
Al (ppm)
Madoonga metamorphic magnetite
b)
Mg/W
Mn/Al
c)
Mn (ppm)
Ti (ppm)
Hypogene magnetite compositional trend line
d)
Al + Mn (wt%)
Ti + V (wt%)
skarn – porphyry
Skarn
IOCG
Fe-Ti, V Porphyry
Kiruna
BIF
BIF (Nadoll et al., 2014)
Ag-Pb-Zn (Nadoll et al., 2014)
e)
Ga/Al
Mn/Ti
Hypogene magnetite
Beebyn least-altered BIF (metamorphic magnetite)
Beebyn Stage 1 magnetite
Beebyn Stage 3 magnetite
Beebyn Stage 6 magnetite
Beebyn Stage 7 magnetite
Beebyn Stage 4 specularite
Beebyn Stage 4 martite after Stage 1 magnetite
Madoonga least-altered BIF (metamorphic magnetite)
Madoonga Stage 2 magnetite
Madoonga Stage 3 specularite

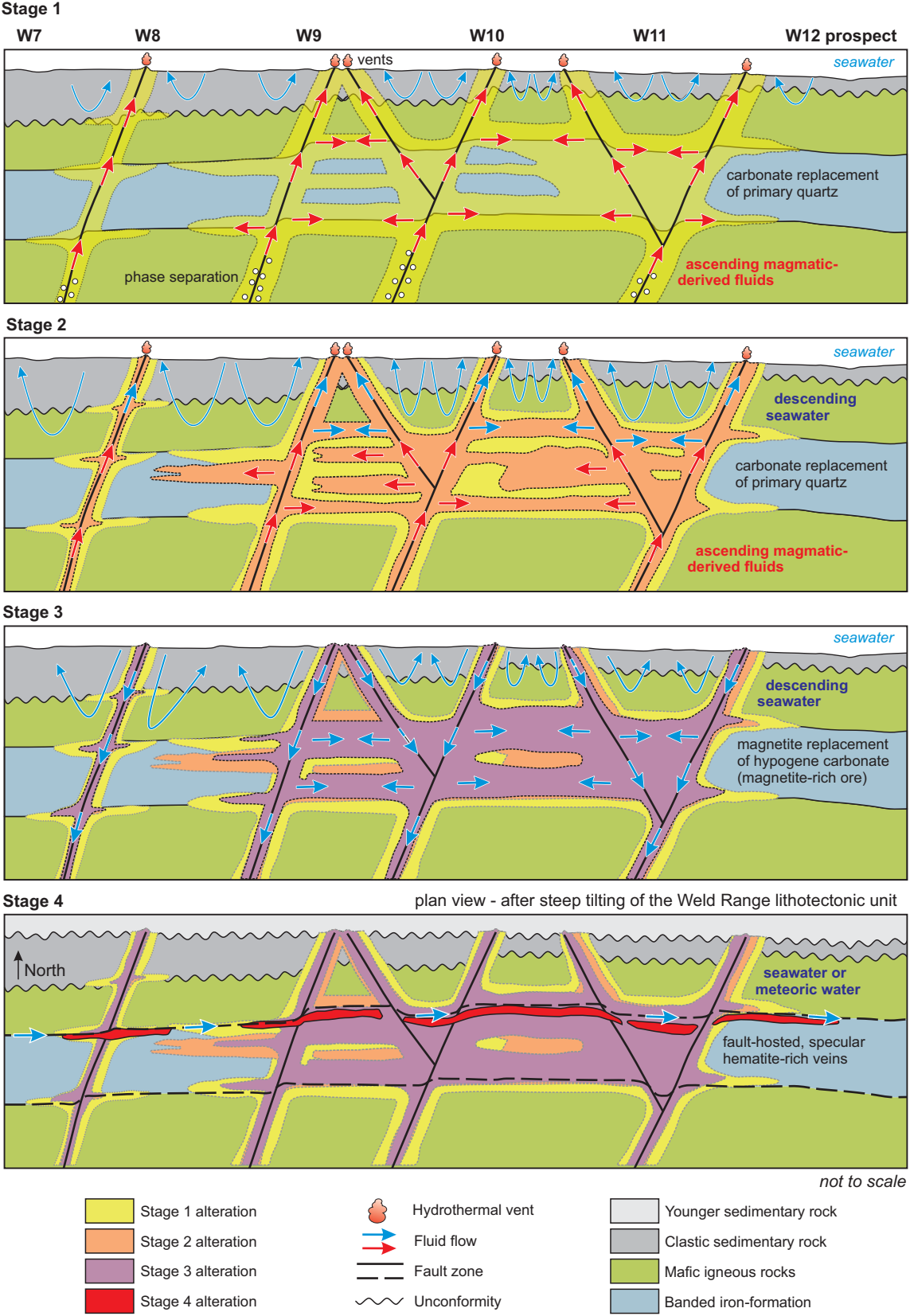
Stage 1
W7
W8
W9
W10
W11
W12 prospect
vents
seawater
carbonate replacement of primary quartz
phase separation
ascending magmatic-derived fluids
Stage 2
seawater
descending seawater
carbonate replacement of primary quartz
ascending magmatic-derived fluids
Stage 3
seawater
descending seawater
magnetite replacement of hypogene carbonate (magnetite-rich ore)
Stage 4
plan view - after steep tilting of the Weld Range lithotectonic unit
North
seawater or meteoric water
fault-hosted, specular hematite-rich veins
not to scale
Stage 1 alteration
Stage 2 alteration
Stage 3 alteration
Stage 4 alteration
Hydrothermal vent
Fluid flow
Fault zone
Unconformity
Younger sedimentary rock
Clastic sedimentary rock
Mafic igneous rocks
Banded iron-formation

Appendix 1 Methods

Hand-specimens of hypogene-altered BIF were collected from outcrop and diamond drill core from the Beebyn and Madoonga deposits for thin section petrography, fluid inclusion, stable (O and C) isotope, and mineral chemistry studies. The samples were collected from different areas of both deposits to ensure that they are representative of each deposit.

Fluid inclusion heating and freezing analyses were conducted on a Linkam THMSG 600 stage with a TMS 93 temperature programmer at the University of Western Australia (UWA), Perth. Doubly-polished thin sections containing specular hematite were studied with an Olympus BX53 microscope configured with infrared transmitted light functionality. A QImaging Retiga-2000R CCD camera was used that allows ovservations in the near infrared spectral range to about 1000 nm. The precision for microthermometric measurements is ±0.2 ºC for temperatures below 30 ºC and ±2 ºC for temperatures above 30 ºC. Salinity (wt% NaCl or $CaCl_2$ equiv), bulk composition, and density were calculated using the MacFlinCor (Brown and Hagemann, 1995) and HokieFlincs_H2O-NaCl programs (Steele-MacInnis et al. (2012), and the Bodnar and Vityk (1994) and Lecumberri-Sanchez et al. (2012) equation of states for the H_2O-NaCl-(KCl) system. The Oakes et al. (1990) equation of state was used for the H_2O-NaCl-$CaCl_2$ system, whereas the Kerrick and Jacobs (1981) equation of state was applied for the pure CO_2 system.

Laser Raman analyses were used to determine the composiition of the vapor and solid phases within fluid inclusions in quartz and dolomite. Raman spectroscopy, conducted at the Centre for Microscopy, Characterisation and Analysis (CMCA) at UWA, involved the use of a WITec Alpha300RA+ confocal Raman microscope system (WITec, Ulm, Germany) equipped with an infrared diode laser module (λ = 785 nm; 300 mW power; 150 mW at the fiber end). Raman spectra were recorded with integration times of 20 seconds using a 100x/0.9 NA objective (Zeiss, Germany), which produces a laser spot with a size of 300 nm laterally and approximately 700 nm vertically. The system was calibrated using the first order Raman peak of silicon prior to the measurements. For analysis of the vapor phases of the fluid inclusions, single spectra and their diagnostic peaks were used to identify CO_2 (the Fermi diad at ~1285 and 1388 cm^{-1}) (Herzberg, 1950; Rosso and Bodnar, 1995; Burke, 2001). The WITec project FOUR software was used for analyses and image processing. Raman detection limits (Wopenka and Pasteris, 1986) are estimated to be about 0.1 mole % for CO_2. Errors in the calculated gas ratios are generally less than 1 mole %.

Laser Ablation Inductively Coupled Plasma Mass Spectrometry was performed on fluid inclusions hosted by quartz and ferroan dolomite at the University of Leeds, United Kingdom, using an ArF 193-nm Geolas Q Plus excimer laser equipped with imaging optics (Günther et al., 1997). The material liberated during the ablation was carried by helium, purging the ablation cell, into the Agilent 7500 quadrupole mass spectrometer. An octopole reaction cell was used for analyses of ^{40}Ca and ^{56}Fe. Fluid inclusion analyses were calibrated using NIST standard SRM 610. A laser spot size of 25 µm was used for analysis. Sixteen elements were included for analysis: ^{23}Na, ^{24}Mg, ^{29}Si, ^{39}K, ^{40}Ca, ^{55}Mn, ^{56}Fe, ^{59}Co, ^{63}Cu, ^{66}Zn, ^{88}Sr, ^{118}Sn, ^{137}Ba, ^{182}W, ^{208}Pb, and ^{209}Bi. Analytical data for the standard and unknowns were processed using SILLS v.1.3.2 software (Guillong et al., 2008). Charge-balancing to NaCl-H_2O equivalent chloride molality was used for data reduction. Further information about method and validation of the procedure can be found in Allan et al. (2005).

Crush-leach analyses were performed on fluid inclusions hosted by quartz, carbonate, magnetite, and hematite at the University of Leeds following the bulk crush-leach method of Banks et al. (2000). Hand-picked, 1 to 2.5 g, mineral separates with particle sizes of between 1 and 2 mm were cleaned by repeated boiling and rinsing in 18.2 MΩ water. Dried samples were crushed to a fine powder using an agate mortar and pestle. Powders were transferred to individual containers and approximately 5 ml of 18.2 MΩ water was added to redissolve the dried salts released from crushed fluid inclusions. The resultant solutions were filtered through a 0.2-µm pore size nylon filter. The leachates were analyzed for Cl^-, Br^-, and SO^{2-}_4 using ion chromatography, and Na^+ and K^+ by atomic absorption. Detection limits for Cl, Br, SO_4, Na and K are 10, 0.2, 10, 30 and 30 ppb, respectively (Heijlen et al., 2003). The typical precision is 5 % relative standard deviation (RSD).

Carbon and oxygen stable isotope analyses were performed on hand-picked, 1 to 2 g, separates of siderite, ferroan dolomite, and calcite at the G.G. Hatch Isotope Laboratories, University of Ottawa, Canada. The $\delta^{18}O$ and $\delta^{13}C$ mineral values are reported in per mil relative to the Vienna Standard Mean Ocean Water (VSMOW) and Pee Dee Belemnite (PDB), respectively. The analytical precision (2 σ) is ± 0.1 ‰. In situ oxygen isotopic data for quartz were collected using a CAMECA IMS 1280 multi-collector ion probe at the CMCA, UWA using conditions similar to those documented by Kita et al. (2009). The quartz standard UWQ-1 was used to measure accuracy and instrument drift. Using a 10 µm analysis spot size, $\delta^{18}O$ values for the quartz standard and unknowns have an accuracy and precision of ± 0.2 ‰. In addition, four samples of hand-picked magnetite grains were analyzed for oxygen isotopes at the University of Wisconsin-Madison. Approximately 5 mg of coarsely powdered magnetite was loaded in a sample holder and pre-fluorinated overnight. Oxygen was extracted from magnetite by laser fluorination reaction with BrF_5 (e.g. Clayton and Mayeda, 1963; Sharp, 1990; Valley et al., 1995; Cole et al., 2004) and analyzed by the Finnigan MAT 251 gas-source mass spectrometer. The garnet standard UWG-2 (Valley et al., 1995) was used to define an accuracy of better than 0.19 ‰ for magnetite analyses.

Electron microprobe analyses were performed on polished thin sections and 2.5 cm-diameter polished sample mounts of magnetite and hematite to test their homogeneity at the CMCA, UWA using a JEOL 6400 SEM and Energy-dispersive X-ray spectroscopy (EDS). A copper standard was used. Analytical conditions were 15 keV and 20 nA. Microprobe results were accepted only if the weight percent total was between 98.5 and 101.5 %. The ferric iron content of each analysis was calculated based on the assumption of stoichiometry and an ideal AB_2O_4 formula. Back-scattered electron imaging was performed using an acceleration voltage of 20 keV and a beam current of 15 nA. Wavelength Dispersion Spectroscopy (WDS) was performed on one representative polished thin section of hypogene iron ore from the Beebyn deposit. Quantitative element maps and prior instrument calibration were acquired on a JEOL 8530F hyperprobe equipped with five tunable wavelength dispersive spectrometers. The operating conditions were 40 degrees take-off angle, and a beam energy of 20 keV. The beam current used was 50 nA and the beam was fully focussed. Elements were acquired using analyzing crystals LiF for Fe kα, Mn kα, Ni kα, Ba lα, Zn kα, Cu kα; PET for Ca kα, P kα, S kα, and TAP for Al kα, Na kα, Mg kα, Si kα. The standards employed were an assortment of commercially available metals, oxides, silicates, sulfates and phosphates. For instrument calibration, counting time was 20 seconds for the kα lines for Si, Al, Na, Fe, P, and Ca, and 40 seconds for Mg kα, Mn kα, Ni kα, Ba lα, Zn kα, Cu kα, S

kα. Mean atomic number background corrections were employed throughout (Donovan and Tingle, 1996). Unknown and standard intensities were corrected for deadtime and the ZAF algorithm used for matrix absorption (Armstrong, 1988). Standard intensities were corrected for standard drift over time. On peak interference corrections were applied as appropriate (Donovan et al., 1993). Detection limits ranged from 0.007 wt% for S kα to 0.010 wt% for Ca kα to 0.014 wt% for P kα to 0.016 wt% for Ni kα to 0.028 wt% for Ba lα. Quantitative chemical maps were acquired using the calibration set up described above for Na, Al, Ba, Mn, P, Mg, Si, Zn, Fe, Ca, Cu, Ni and S. Detection limit maps were acquired for these elements and applied as the minimum cut-off values for all maps. Map acquisition used a 100 nA beam current with a 2 x 2 µm pixel dimension and 100 msec dwell time per pixel. Data were processed using the Calcimage software package and output to Surfer® for further processing and enhancement.

Major and trace element concentrations for magnetite and hematite were completed by in situ LA-ICP-MS analysis at the AGOS-GeoHistory LA-ICP-MS Facility, Curtin University, in Perth, Australia. The reference materials, GSD-1G, NIST-610, and NIST-612 were used to measure accuracy and instrument drift. An analytical spot size of 75 µm and ablation time of 40 seconds per analysis was used. Forty-eight elements were included in the analyses: ^{23}Na, ^{24}Mg, ^{27}Al, ^{28}Si, ^{31}P, ^{39}K, ^{44}Ca, ^{45}Sc, ^{49}Ti, ^{51}V, ^{52}Cr, ^{55}Mn, ^{57}Fe, ^{59}Co, ^{60}Ni, ^{65}Cu, ^{66}Zn, ^{71}Ga, ^{74}Ge, ^{75}As, ^{87}Rb, ^{88}Sr ^{89}Y, ^{92}Zr, ^{93}Nb, ^{95}Mo, ^{115}In, ^{118}Sn, ^{121}Sb, ^{137}Ba, ^{139}La, ^{140}Ce, ^{141}Pr, ^{146}Nd, ^{147}Sm, ^{153}Eu, ^{157}Gd, ^{163}Dy, ^{165}Ho, ^{166}Er, ^{172}Yb, ^{175}Lu, ^{181}Ta, ^{182}W, ^{208}Pb, ^{209}Bi, ^{232}Th, and ^{238}U. LA-ICP-MS data were processed using SILLS v.1.3.2 software (Guillong et al., 2008) to exclude spectra or parts of spectra that are affected by mineral inclusions. Iron (^{57}Fe) was used as the internal standard element using the stoichiometric Fe contents of magnetite and hematite (723,600 ppm and 699,400 ppm, respectively), because SEM-EDS analyses did not demonstrate significant variations from stoichiometric Fe concentrations within the analytical uncertainty. Average detection limits are reported in Table A12.

References

Allan, M.M., Yardley, B.W.D., Forbes, L.J., Shmulovich, K.I., Banks, D.A., and Shepherd, T.J., 2005, Validation of LA–ICP-MS fluid inclusion analysis with synthetic fluid inclusions: American Mineralogist, v. 90, p. 1767–1775.

Armstrong, J.T., 1988, Quantitative analysis of silicate and oxide minerals: comparison of Monte Carlo, ZAF and phi-rho-z procedures: Microbeam analysis, v. 23, p. 239–246.

Banks, D.A., Green, R., Cliff, R.A., and Yardley, B.W.D., 2000, Chlorine isotopes in fluid inclusions: determination of the origins of salinity in magmatic fluids: Geochimica et Cosmochimica Acta, v. 64, p. 1785–1789.

Bodnar, R.J. and Vityk, M.O., 1994, Interpretation of microthermometric data for NaCl-H_2O fluid inclusions, in B De Vivo and ML Frezzotti ed., Fluid inclusions in minerals: methods and applications, Blacksburg, Virginia, United States of America, Virginia Polytechnic Institute and State University, p. 117–131.

Brown, P.E. and Hagemann, S.G., 1995, MacFlinCor and its application to fluids in Archaean lode-gold deposits: Geochimica et Cosmochimica Acta, v. 59, p. 3943–3952.

Burke, E.A.J., 2001, Raman microspectrometry of fluid inclusions: Lithos, v. 55, p. 139–158.

Clayton, R.N. and Mayeda, T.K., 1963, The use of bromine pentafluoride in the extraction of oxygen from oxides and silicates for isotopic analysis: Geochimica et Cosmochimica Acta, v. 27, p. 43–52.

Cole, D.R., Horita, J., Polyakov, V.B., Valley, J.W., Spicuzza, M.J., and Coffey, D.W., 2004, An experimental and theoretical determination of oxygen isotope fractionation in the system magnetite–H_2O from 300 to 800ºC: Geochimica et Cosmochimica Acta, v. 68, p. 3569–3585.

Donovan, J.J., Snyder, D.A., and Rivers, M.L., 1993, An improved interference correction for trace element analysis: Microbeam analysis, v. 2, p. 23–28.

Donovan, J.J. and Tingle, T.N., 1996, An improved mean atomic number correction for quantitative microanalysis: Journal of Microscopy, v. 2, p. 1–7.
Guillong, M., Meier, D.L., Allan, M.M., Heinrich, C.A., and Yardley, B.W.D., 2008, Appendix A6: SILLS: a MATLAB-based program for the reduction of laser ablation ICP-MS data of homogeneous materials and inclusions, in P Sylvester ed., Laser ablation ICP-MS in the Earth Sciences: Current practices and outstanding issues, Vancouver, British Columbia, Mineral Association of Canada, p. 328–333.
Günther, D., Frischknecht, R., Heinrich, C.A., and Kahlert, H.-J., 1997, Capabilities of an argon fluoride 193 nm excimer laser for laser ablation inductively coupled plasma mass spectometry microanalysis of geological materials: Journal of Analytical Atomic Spectrometry, v. 12, p. 939–944.
Heijlen, W., Muchez, P., Banks, D.A., Schneider, J., Kucha, H., and Keppens, E., 2003, Carbonate-hosted Zn–Pb deposits in Upper Silesia, Poland: Origin and evolution of mineralizing fluids and constraints on genetic models: Economic Geology, v. 98, p. 911–932.
Herzberg, G., 1950, Molecular spectra and molecular structure (2nd edition): New York, USA, Van Nostrand,
Kerrick, D.M. and Jacobs, G.K., 1981, A modified Redlich-Kwong equation for H_2O, CO_2, and H_2O-CO_2 mixtures at elevated pressures and temperatures: American Journal of Science, v. 281, p. 735–767.
Kita, N., Ushikubo, T., and Valley, J., 2009, High precision SIMS oxygen isotope analysis and the effect of sample topography: Chemical Geology, v. 264, p. 43–57.
Lecumberri-Sanchez, P., Steele-MacInnis, M., and Bodnar, R.J., 2012, A numerical model to estimate trapping conditions of fluid inclusions that homogenize by halite disappearance: Geochimica et Cosmochimica Acta, v. 92, p. 14–22.
Oakes, C.S., Bodnar, R.J., and Simonson, J.M., 1990, The system NaCl–$CaCl_2$–H_2O: I. The ice liquidus at 1 atm total pressure: Geochimica et Cosmochimica Acta, v. 54, p. 603–610.
Rosso, K.M. and Bodnar, R.J., 1995, Microthermometric and Raman spectroscopic detection limits of $C0_2$ in fluid inclusions and the Raman spectroscopic characterization of $C0_2$: Geochimica et Cosmochimica Acta, v. 59, p. 3961–3975.
Sharp, Z.D., 1990, A laser-based microanalytical method for the in situ determination of oxygen isotope ratios of silicates and oxides: Geochimica et Cosmochimica Acta, v. 54, p. 1353–1357.
Steele-MacInnis, M., Lecumberri-Sanchez, P., and Bodnar, R.J., 2012, HokieFlincs_H2O-NaCl: A Microsoft Excel spreadsheet for interpreting microthermometric data from fluid inclusions based on the PVTX properties of H_2O–NaCl: Computers & Geosciences, v. 49, p. 334–337.
Valley, J.W., Kitchen, N., Kohn, M.J., Niendorf, C.R., and Spicuzza, M.J., 1995, UWG-2, a garnet standard for oxygen isotope ratios: Strategies for high precision and accuracy with laser heating: Geochimica et Cosmochimica Acta, v. 59, p. 5223–5231.
Wopenka, B. and Pasteris, J.D., 1986, Limitations to quantitative analysis of fluid inclusions in geological samples by laser Raman microprobe spectroscopy: Applied Spectroscopy, v. 40, p. 144–151.

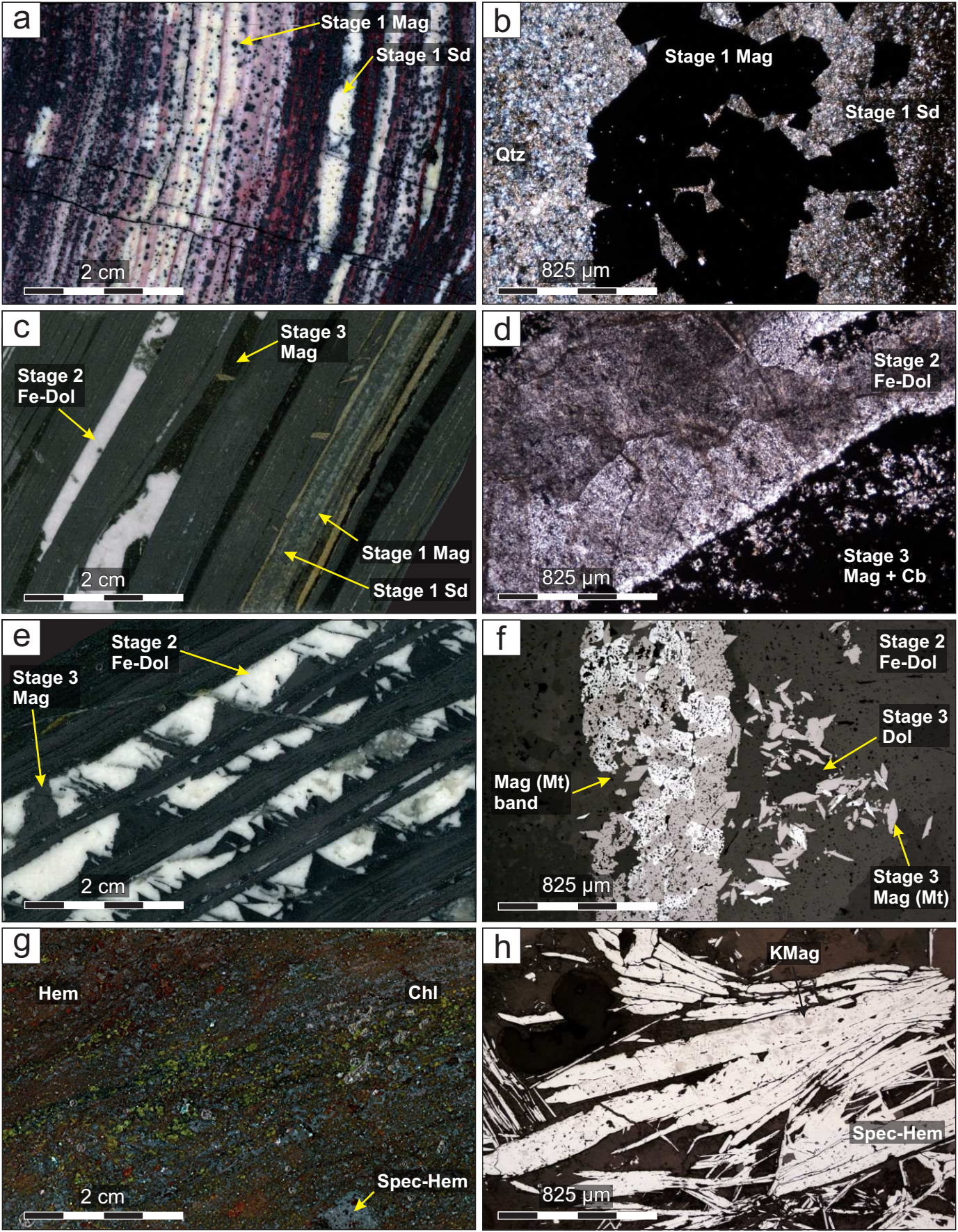
a
Stage 1 Mag
Stage 1 Sd
2 cm
b
Stage 1 Mag
Stage 1 Sd
Qtz
825 µm
c
Stage 3
Mag
Stage 2
Fe-Dol
Stage 1 Mag
Stage 1 Sd
2 cm
d
Stage 2
Fe-Dol
Stage 3
Mag + Cb
825 µm
e
Stage 2
Fe-Dol
Stage 3
Mag
2 cm
f
Stage 2
Fe-Dol
Stage 3
Dol
Mag (Mt)
band
Stage 3
Mag (Mt)
825 µm
g
Hem
Chl
Spec-Hem
2 cm
h
KMag
Spec-Hem
825 µm

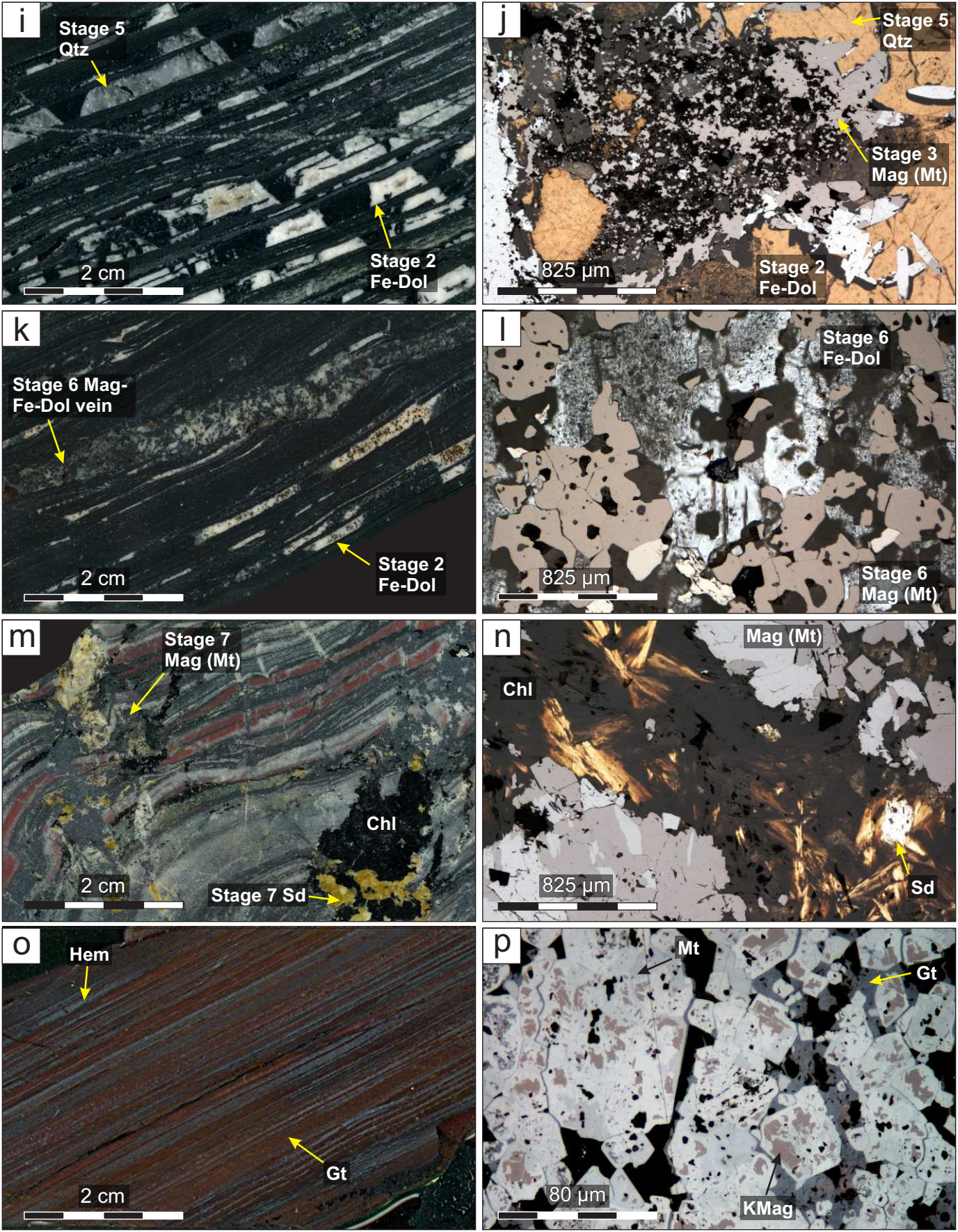
i
Stage 5
Qtz
2 cm
Stage 2
Fe-Dol
j
Stage 5
Qtz
Stage 3
Mag (Mt)
825 µm
Stage 2
Fe-Dol
k
Stage 6 Mag-
Fe-Dol vein
2 cm
Stage 2
Fe-Dol
l
Stage 6
Fe-Dol
825 µm
Stage 6
Mag (Mt)
m
Stage 7
Mag (Mt)
Chl
2 cm
Stage 7 Sd
n
Mag (Mt)
Chl
825 µm
Sd
o
Hem
Gt
2 cm
p
Mt
Gt
80 µm
KMag

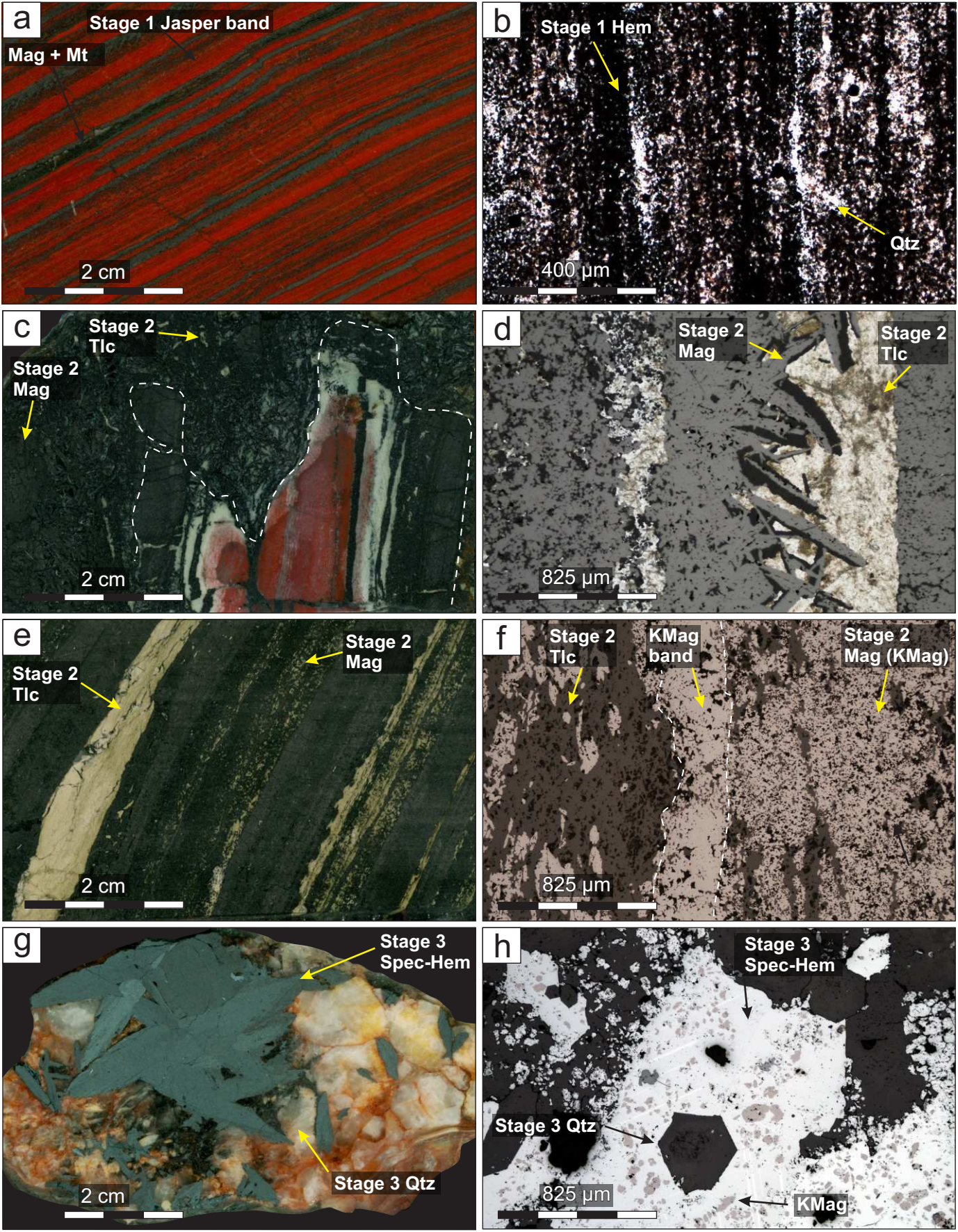
a
Stage 1 Jasper band
Mag + Mt
2 cm
b
Stage 1 Hem
Qtz
400 µm
c
Stage 2
Tlc
Stage 2
Mag
2 cm
d
Stage 2
Mag
Stage 2
Tlc
825 µm
e
Stage 2
Mag
Stage 2
Tlc
2 cm
f
Stage 2
Tlc
KMag
band
Stage 2
Mag (KMag)
825 µm
g
Stage 3
Spec-Hem
Stage 3 Qtz
2 cm
h
Stage 3
Spec-Hem
Stage 3 Qtz
825 µm
KMag

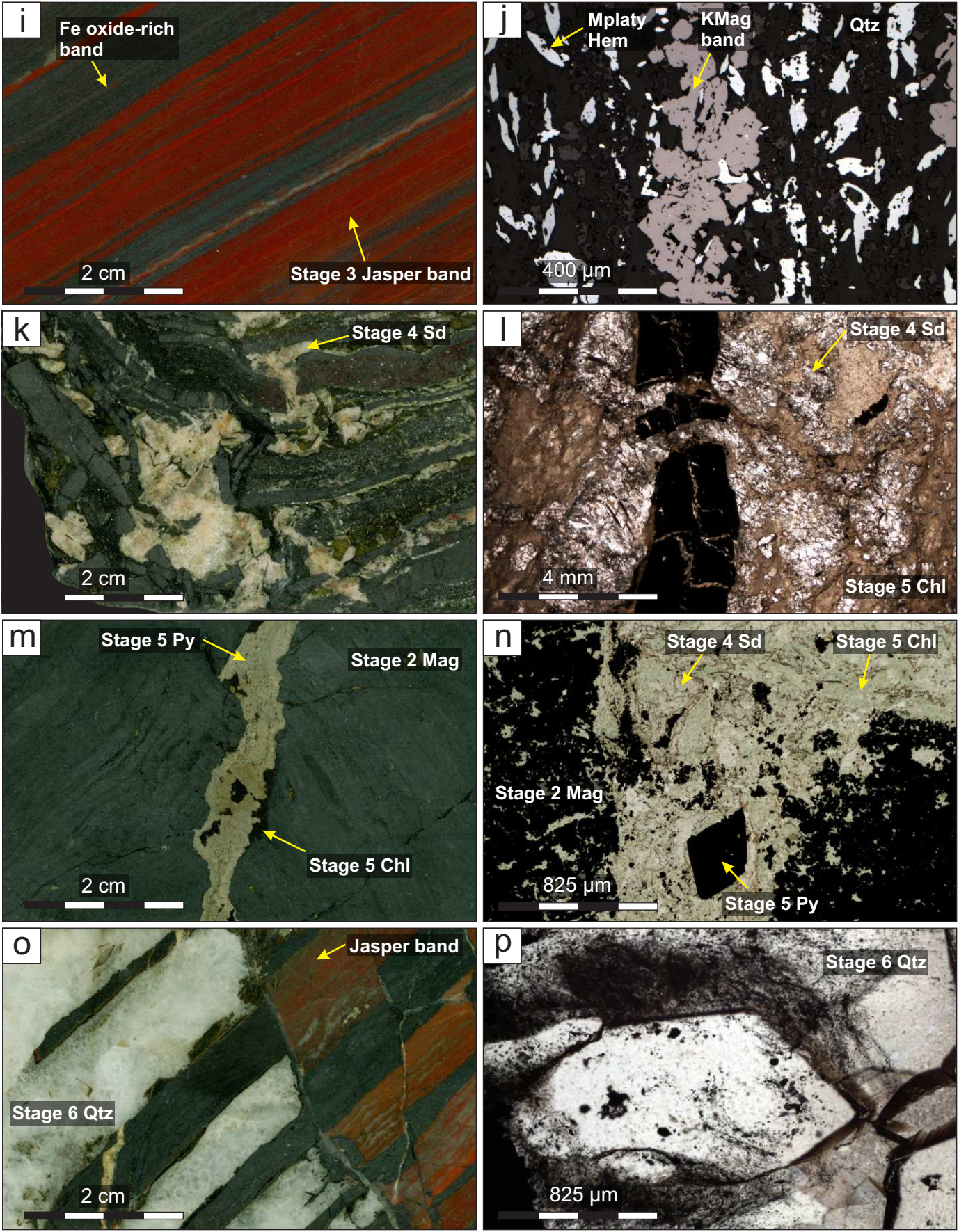
i
Fe oxide-rich band
2 cm
Stage 3 Jasper band
j
Mplaty Hem
KMag band
Qtz
400 µm
k
Stage 4 Sd
2 cm
l
Stage 4 Sd
4 mm
Stage 5 Chl
m
Stage 5 Py
Stage 2 Mag
Stage 5 Chl
2 cm
n
Stage 4 Sd
Stage 5 Chl
Stage 2 Mag
825 µm
Stage 5 Py
o
Jasper band
Stage 6 Qtz
2 cm
p
Stage 6 Qtz
825 µm